Task Specific Humanoid Hand Design using Single Crystal Ultrasonic Motors

Ho Teng Jun

(B.Eng, NUS)

A thesis submitted for

The Degree of Master of Engineering

Department of Mechanical Engineering

National University of Singapore

2007

Acknowledgement

Contents

Summary

This thesis presents the design and synthesis of a humanoid hand based on a set of predefined task requirements. This hand design utilizes cylindrical ultrasonic motor as driving agent, which is also developed and constructed within the university.

An effective humanoid hand design is proposed to meet the functional aspect of a human hand in daily activities. This functional requirement is explicitly represented as the ability to perform the six basic grasps — Cylindrical, Spherical, Lateral, Palmar, Pinch and Hook. To implement this ability into the design, a set of point contact system and functional definitions is developed for the six grasps. As a result, a task specific humanoid hand model is formed and optimized.

A humanoid hand typically demands high-torque and compact actuators to perform various activities. After a thorough research and investigation, the cylindrical ultrasonic motor is finally chosen. The operating principle, by which the vibration motion of the piezoelectric crystal is transformed into rotary motions of the motor, is discussed. Simple beam model is adopted to estimate the rotational speed and torque of the motor. Three cylindrical ultrasonic motors have been constructed and tested. These motors make use of the novel PZN-7%PT (Lead-Zinc-Niobate-Lead-Titanate) piezoelectric single crystal as their driving element. Experimental results on the rotational speed, torque and power output are also obtained.

A driving system for the ultrasonic motors that includes a four-phase full bridge inverter and DC-DC converter is developed. The amplitude of driving voltage signals is chosen as the primary control input, which is controlled by the duty cycle of DC-DC converter. Direction of motor rotation is interchangeable by switching the phase

difference between $90°$ and $-90°$.

Lastly, a single finger prototype is constructed to evaluate the implementation of cylindrical ultrasonic motors. It is found that the proposed actuation system is simple, light-weight and small in size, but further improvements are needed to increase the motor torque. Several observations were made and proposed for future research work.

List of Figures

List of Tables

Chapter 1

Introduction

1.1 Background

1.1.1 Humanoid Hand

Since the industrial revolution, humans have been constantly replaced by machines in many mass production lines. In order to perform the same work that was previously done by human hands, mechanical actuators having similar hand functions have been continuously invented. Mechanical grippers, hooks, clamps and some other classic examples can be treated as the first generation of robotic hands. Nowadays, robotic hand applications can be found in many fields and industries. Different needs from different industries stimulate the evolution of robotic hands in different forms. In particular, applications such as prosthesis, tele-operations and humanoid robots for individual entertainment prefer a multi-functional and human-hand-shape design. This particular breed of robotic manipulators is called the humanoid hand.

In short, humanoid hand is an imitation of the human hand in terms of functionality and appearance. It has been a hot research topic due to its highly complex structure. Ideally a humanoid hand should possess the following properties:

- *multi-functional*: It can reproduce all kinds of hand functions. It is capable of performing various hand grasps and manipulations.

- *dexterous*: Its hand structure is versatile. It can form different type of hand poses and has unlimited ways to form them.

- *human factor*: The outer appearance of the design resembles or partly resembles a human hand. This anthropomorphic feature is important for prosthesis and tele-operation applications.

- *high torque strength*: Actuators used can provide sufficient torque power for normal human hand operations. The torque-to-weight ratio has to be high.

- *compact size*: Compactness is high with carefully designed mechanical structure.

Humanoid hand design itself is a very broad research topic. Development of humanoid hand requires multi-disciplinary knowledge such as design mechanics, artificial intelligent control, electronics circuitry, materials, etc. This complexity of humanoid hand is mainly contributed by the attempt taken to duplicate the functionality of human hand completely. If a humanoid hand is designed to be capable of only limited number of tasks, its complexity could be slashed down significantly. This type of task-oriented humanoid hand will be simple to use, efficient and less costly compared to conventional design approach.

1.1.2   Task Specific Humanoid Hand Design

Sometimes, in a structured working environment or some particular applications, the use of humanoid hand is limited to several simple functions. This renders a humanoid hand with full manipulating and grasping potentials becomes unnecessary. On the other hand, the nature of the workspace may require more than a simple industrial gripper. With these considerations, a task specific humanoid hand design will be appropriate.

In this thesis, a new approach is attempted in humanoid hand design by specifying the task required before hand. As opposed to mainstream designs, it is not merely a duplication of human hand but a specialized humanoid hand design with a set of predefined functions. The necessary hand functionality is then dependent on the range of tasks to be given.

Features

Some important advantages of Task Specific Humanoid Hand Design over conventional approach are listed below:

- Simpler mechanical design results a more compact and rigid structure.

- Less Degree of Freedoms (DOF) are required in the design, indicates that the number of actuators used is reduced. This further implies that hand control issue is simplified.

- Required hand functionality is achieved using the least possible amount of DOFs. The kinematic design becomes more effective.

- Specification of humanoid hand for the given tasks improves its performance in executing them and at the same time, removes redundant DOFs.

- Reduced hand complexity also helps in easier mass production.

- Maintenance of humanoid hand becomes simpler.

However, this hand specialization also has its price to pay:

- A comprehensive set of task definitions is required to serve as a design reference.

- Because of the task specification, the hand design is generally not effective when the task environment changes. Therefore these tasks must be planned carefully in advance.

- The design approach is not efficient when complicated tasks are given.

Classifications

Humanoid hands can be classified according to the actuator types used or their driving methods. Researchers commonly prefer the latter method. Basically the driving methods can be classified into *built-in-actuator type* and *wire-driven type*. Some humanoid hands are reported to be of *hybrid type*. (Table 1.1, page 9)

1. **Built-in-Actuator Type**

    (a) DC Servo Motors

    (b) Ultrasonic Motors

    (c) Shape Memory Alloys

2. **Wire-Driven Type**

    (a) Pneumatic Actuators

    (b) Hydraulic Actuators

    (c) Electromagnetic Motors

    (d) Ultrasonic Motors

3. **Hybrid Type**

    (a) Ultrasonic Motors

The humanoid hand design in this work employs built-in-actuator type driving method. In addition, a special type of cylindrical ultrasonic motor utilizing piezoelectric single crystal is constructed and used.

1.1.3 Ultrasonic Motors

The general definition of ultrasonic motor as given in [1] is:

> *An ultrasonic motor is a kind of motor that uses ultrasonic vibration — a type of elastic vibration — to obtain driving force and drives the motor through frictional force.*

Ultrasonic motors (USMs) are always referred as piezoelectric type USMs since the type of elastic vibration mentioned above is mainly generated by piezoelectric resonators.

In an ultrasonic motor operation, piezoelectric elements are excited by alternating current and generate mechanical vibration of high frequency but small amplitude. This rapid oscillation in turn excites the motor stator in resonance state, causing particles on

the surface of the stator to perform an elliptic motion. The rotor is then pressed against the stator and is driven by friction contact force in between the stator-rotor interface. At the contact points, the horizontal force component of this elliptic motion is transmitted to the rotor through friction. The rectified motion of the rotor can take linear, rotary, or even multi-DOF form depending on different structures of the USMs.

USMs have their advantages over conventional electromagnetic motors in robotic applications. Some important features are:

- USMs can produce high torque at low speed, which is preferable in robotic applications.

- High power to weight ratio. This is critical for space constrained humanoid hand structure.

- Direct drive method is possible since speed-gear reduction is not necessary.

- Precise motor positioning as there is no backlash error due to speed-gear reduction.

- High holding torque at off-state due to the static friction force between stator-rotor interface.

- Silent operation as it works at ultrasonic frequency range.

- No electromagnetic interference.

- The motor structure is simple, which simplifies the mechanical design.

Nevertheless, the application of USMs in robotics has to overcome several difficulties:

- Piezoelectric elements in the motor are fragile and are prone to fatigue failure.

- Piezoelectric properties and the resonant frequency are dependent on temperature. This temperature effect lowers the motor efficiency.

- Multiple phase high frequency sinusoidal voltage signals are required to drive the motor. Thus complex driving circuitry is necessary.

- USM dynamic model is complex and highly non-linear. Advanced control schemes are required.

USM is chosen as the main actuator for this humanoid hand project in view of its outstanding properties. A series of cylindrical USMs has been custom made to meet the specification of the task specific humanoid hand design. Furthermore, novel PZN-7%PT piezoelectric single crystal is used to enhance the motor performance.

1.2 Objective

Robotic hand research has been active since the late 20th century, but the development of humanoid hands is only getting popular recently. This is most probably due to the emergence of humanoid industry for personal entertainment, elder care, tele-operations, etc. Besides that, intelligent, easy-to-use and human-like robot hands have been highly required for prosthesis. However, conventional humanoid hands have been complex, bulky and hard to control. The objective of this thesis is to design a simplified version of humanoid hand based on a set of expected hand functions. A systematic task specific approach is taken to generate a design which is effective and yet highly functional. Another objective of this work is to explore the potential of direct drive ultrasonic motor as humanoid hand actuator. This cylindrical USM is specially designed using piezoelectric single crystal.

1.3 Literature Survey

1.3.1 Development of Humanoid Hand

The development of dexterous multi-fingered robot hand is a challenging endeavor, which has been pursued by many researchers. Great strides have been made since the 80's in the design and development of dexterous robot hands. Many articulated hands have been built, among these are some well-known examples such as the Stanford/JPL Hand by Salisbury *et al* [2], UTAH/MIT Hand by Jacobsen *et al* [3] and DLR II Hand by

Butterfass *et al* [4]. These devices make it possible for the robot to grasp and manipulate objects.

It is natural that most robot hand models have mechanical structure similar to human hand, since these robot hands are designed for taking human operations. Anthropomorphic hand structure is still dominating because the human hand is an existence proof in grasp and manipulation of objects. Furthermore, in some applications (prosthesis, teleoperation, etc), human-hand shape appearance is part of the necessary requirements. Therefore, anthropomorphic multi-fingered robot hand, or humanoid hand, is getting popular in the research field.

Many researches have been performed on the kinematics of hand grasp and manipulation after Salisbury's work [5]. The research results suggest that most of the human hand operations are essentially accomplished by using only the thumb, index finger and middle finger. Therefore, there are always at least three fingers (including thumb) in a humanoid hand. Some examples are Stanford-JPL Hand (3-fingers) [2], UTAH/MIT Hand (4-fingers) [3] and the Robonaut Hand (5-fingers) [6].

The number of DOFs in the humanoid hand also differs from one design to another. Biomechanics study on human hand showed that it has 25 DOFs and each finger has four DOFs when it moves freely without holding an object [7]. However, previous researches have shown that robot hands with high DOFs are very difficult to construct and control. The most critical problem is the limitation of size, especially for built-in-actuator type humanoid hands [4]. Since all of the mechanical elements, such as actuators and sensors, must be installed inside the finger or palm, it imposes a limit to the number of DOFs to be placed. In wire-driven actuator type hands, actuators are remotely installed [2, 3]. It makes the hand structure simple and light by using wire or belt driving mechanism, and hence multiple DOFs system is possible. In fact, a number of humanoid hands take advantage of coupled joint design (several DOFs controlled by 1 actuator) to reduce the number of actuators used.

Older robotic systems use three main types of actuation: *hydraulic, pneumatic* and *electromagnetic* motors [2, 3]. These actuation modes are still commonly found in many

humanoid hands nowadays because of their robustness, linearity and high power rating. However, the type of actuators used for humanoid hand has been diversified as a result of new materials and technology inventions. New breakthrough in materials has created new possibilities, where *piezoelectric* and *magnetostrictive* actuators are reported to be promising [8]. The invention of piezoelectric ultrasonic motor by Sashida [9] has stirred up a lot of interest in its application as humanoid hand actuator, due to its excellent features [10, 11, 12]. On the other hand, some attempted humanoid hand actuator designs using *shape memory alloy* [13] and *electroactive polymers* (also known as artificial muscle) [14]. These new actuators are getting much attention recently as they are having higher power to weight ratio comparing to conventional actuators. However, they are still plagued with low efficiency, non-linear control and some other issues.

Table 1.1 shows a list of anthropomorphic robot hands using different actuator technologies in chronological order. It can be seen that electromagnetic motor is still the main stream actuator in humanoid hand design. Main considerations on the choice of electric motor include commercial availability, linear behavior, high torque, compact size, etc. However, the main disadvantage for this actuator is the overheating problem when the hand is required to maintain a certain torque output (for instance, holding a tool). Some researchers get around this problem by using extra preload springs as passive holding force. Built-in-actuator type humanoid hands are designed mainly for the purpose of prosthesis and general usage where compatibility with different robot arms is important. On the other hand, the Robonaut Hand, which is used for space extra-vehicular activity (EVA), is wire-driven to reduce the hand size. In general, the functionality of low-DOF hands such as Ultralight Hand and Gifu Hand is comparatively lower than high-DOF hands. They are only capable of producing power grasp and precision grasp. High-DOF hands like Shadow Hand and DLR II Hand are able to perform not only grasping motions but also human-like fine manipulations.

Current dexterous humanoid hands have been focused on reproducing, as close as possible, the size, kinematics, and strength of a human hand. The mechanical structure of recent humanoid hands simply follows an anthropomorphic appearance (i.e., four fingers

Table 1.1: Comparison of Specification of Robot Hands

Name	Fingers	DOF	Actuator	Driving Mechanism
Stanford-JPL Hand [2]	3	9	Electric Motor	Wire-Driven
UTAH/MIT Hand [3]	4	16	Pneumatic Tendon	Wire-Driven
Belgrade/USC Hand [15]	5	16	Electric Motor	Built-In Actuator
Anthrobot-2 Hand [16]	5	20	DC Servomotor	Wire-Driven
NTU Hand [17]	5	17	DC Micromotor	Built-In Actuator
WENDY Hand [18]	4	13	AC Servo Motor	Built-In Actuator
Robonaut Hand [6]	5	12	Brushless DC Motor	Wire-Driven
Raparelli Hand [19]	5	15	Pneumatic Valve	Built-In Actuator
Ultralight Hand [20]	5	13	Fluidic Actuator	Built-In Actuator
DLR II Hand [4]	4	13	Brushless DC Motor	Built-In Actuator
Gifu Hand III [21]	5	16	DC Servomotor	Built-In Actuator
Shadow Hand [22]	5	21	Pneumatic Muscle	Wire-Driven
Ultrasonic Hand [12]	5	20	Ultrasonic Motor	Built-In Actuator
UB Hand III [23]	5	16	DC Brushed Motor	Wire-Driven
KH Hand type S [24]	5	15	Brushless DC Motor	Built-In Actuator
SKKU Hand II [25]	4	13	Electric Motor	Built-In Actuator
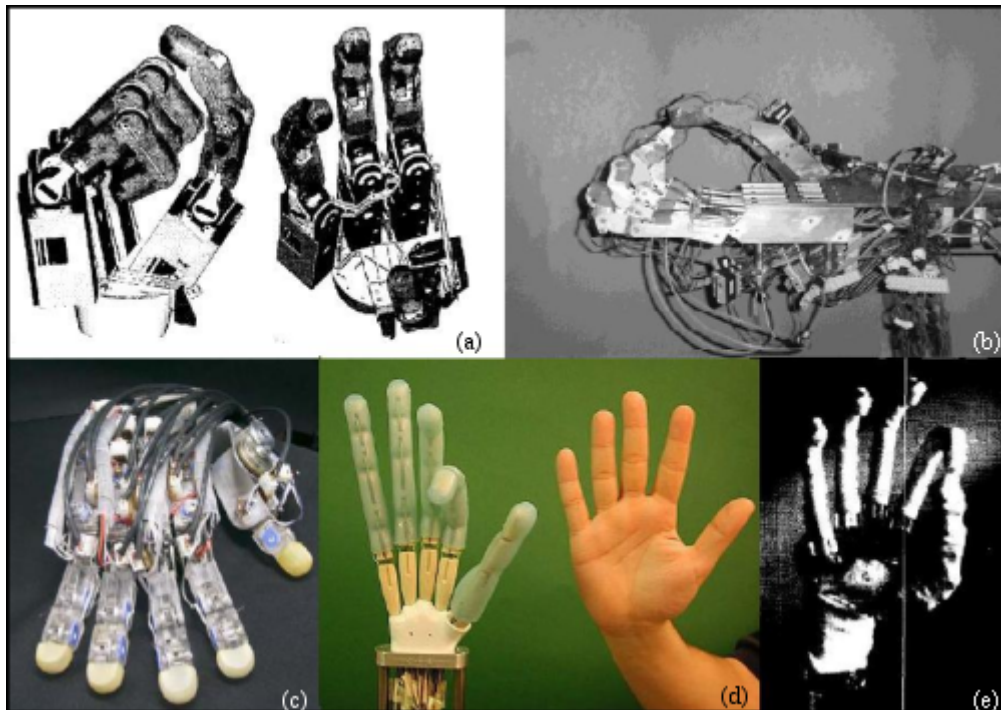
Figure 1.1: Robot Hands from left top corner: (a)DLR-Hand II[4], (b)Raparelli Hand[19], (c)Ultrasonic Hand[12], (d)UB Hand III[23] and (e)Ultralight Hand[20]

and one thumb with corresponding links and joints) without much consideration on the functional effectiveness. In fact, some humanoid hands have limited functionality even if the number of DOFs is high. This is because the kinematic structure is not properly designed to its full potential.

1.3.2 Multi-fingered Grasping Analysis

Many studies have been performed relating to multi-fingered grasping. These involve mechanical design(Cutkosky) [26], stability analysis(Bicchi) [27], kinematics(Li *et al*) [29] and dexterous manipulation(Zhang *et al*) [30].

The formation and classification of different human hand grasps was first observed and introduced by Cutkosky based on grasping motion of factory workers [31]. The Cutkosky taxonomy is then used to describe the hand grasping capability and later becomes an important reference in the design of robot hands. The stability of a grasp is also one of the fundamental issues concerning multi-fingered grasping. Thorough investigations have been carried out by the likes of Bicchi [27] and Rimon [28] on stability analyses, which are characterized by form closure and force closure properties. Loosely speaking, these properties are related to the capability of robot hand to inhibit the motions of object in spite of external applied forces. As opposed to purely geometric nature of form closure, force closure involves consideration of how the contact force can be applied on the object. Hence, the study of force-closure plays a more important role in the positioning of fingers of a robotic hand on the grasped object so as to guarantee robustness against slippage. Many contributions on form closure and force closure grasp synthesis have also been made in an attempt to construct optimal stable grasps for different object shapes [32, 33, 34]. These constructions lead to analytical methods for optimal grasp planning, for which quantitative test was proposed to assess the location and number of contact points [27, 35].

Multi-fingered grasping analysis has explored many aspects in grasping and manipulation of arbitrary objects. Particularly, the stability analysis laid some efficient guidelines for optimal grasp planning in autonomous robot hands. However, in the literature

on grasping and closure analysis, little attention seems to have been paid to the role of the end-effector structure and kinematics. The relationship between the hand grasp structures in Cutkosky taxonomy, and their corresponding force closure properties and contact points are still not clearly defined. In the course of constructing robust force-closure robotic grasps, if the desired location and necessary number of contact points is known, redundant DOF in the mechanical structure can be removed. This exercise can improve the humanoid hand design by reducing its structural complexity, i.e. remove redundant DOF, without sacrificing the hand functionality.

1.3.3 Ultrasonic Motor Actuator

The use of ultrasonic motor (USM) as humanoid robot hand actuator has not been attempted until recent years [12]. The present interest in ultrasonic motors was triggered by Sashida's work in early nineteen eighties [9]. Sashida has invented the ring-type USM and since then USM was reported in literature to have many outstanding properties such as high torque-low speed, high holding torque, high power to weight ratio, etc. The results have attracted many interests for its application in robotics.

The servo control of USM has become a hot topic since the recognition of its potential to replace electromagnetic motor. Much effort has been made to control ring-type USM. However, finding accurate model of USM suitable for control purpose is extremely difficult, because its motion is generated from the piezoelectric effect and frictional force, which are difficult to model mathematically. Modeling of the mechanical vibration of stator and the contact between the stator and rotor using classic elastic theories has been performed by many researchers such as Hagedorn [36], Hagood [37] and recently Dong Sun *et al* [38]. Pons [39] presented a more comprehensive modeling strategy that covers the minor effects in mechanical, piezoelectric and electric field domains. Due to the complexity of the mathematical model, several estimated models were also proposed based on *Finite Element Methods*(FEM) [40], *Equivalent Circuit Model*(ECM) [41] and *Energy Conversion Method.* These models provide considerably good results in predicting the motor characteristics. Currently most of the servo control schemes for USM prefer

the use of estimated models or methods that do not require dynamic models. Some of the methods are *fuzzy logic and neural network control schemes* [42, 43], *adaptive control* [44], *sliding mode control* [45, 46], etc.

Cylindrical USM is a relatively new development. It shares some common operating characteristics with the ring-type USM. For instance, its operation requires two sinusoidal voltage inputs with a specific phase difference. However, cylindrical USM is unique in that the motion of its rotor is generated from *the bending of the stator tube.* This makes cylindrical USM has some operating characteristics that are different from the ring-type USM. For example, the motor stator is in tube form and rotors are positioned on the two sides of tube. This configuration makes the cylindrical USM particularly suitable for direct drive actuation. Because of this mechanical structure advantage, cylindrical USM is chosen as the motor actuator prototype in this project.

Dynamics modeling of cylindrical USM faces the same difficulty as the ring-type USM. The dynamics of piezoelectric cylindrical shell and the vibration mode analysis has been a rather complicated area due to the non-linearity and various minor effects. Modeling analysis has been focused on 3-D FEM models, with some notable exceptions by Berg *et al* [47], Morita [48] and also Lu *et al* [49]. Berg derived a set of equations of motion for the vibration of piezoelectric shell, generalizing from the Flügge's shell theory while Mortia described the bending mode of stator using simple beam bending model. On the other hand, Lu introduced a kinetic analysis on cylindrical USM and gave some structural optimizations. However, the input-output relationships of cylindrical USM and the development of an effective servo control scheme still remain a challenge. Thus, in this thesis the motor characteristics of cylindrical USM are carefully explored, with the focus on establishing the torque-speed curve under different operating conditions.

1.4   Thesis Outline

Chapter 1 provides the necessary background information about the general expectation on a humanoid hand, and the need of task specific design. Ultrasonic motor actuator is also briefly discussed regarding its superiority over conventional electromagnetic motors.

The literature survey gives the current research status of humanoid hand development, multi-fingered grasping analysis and the design and control of USM.

Chapter 2 defines the design philosophy of a task specific hand design and shows that hand functionality of a prosthesis hand can be represented by six basic grasps. A set of grasp definitions is then developed from these six basic grasps, which serves as the main design criteria. Based on these specifications, a kinematic structure is then proposed. It is followed by results of structural analysis and grasp simulations that confirm the kinematic design.

Chapter 3 discusses the development of an actuation system using cylindrical USM. It starts with a review on power requirement of humanoid hand, and points out the need of a high torque actuator. Cylindrical USM is finally chosen based on its superior properties. The basic working principle, vibration mode dynamics and theoretical speed and torque of cylindrical USM are introduced in detail. For humanoid hand design, motors of different sizes are designed and constructed using single piezoelectric crystal as driving element. The later part of the chapter deals with the design and implementation of a driving circuit that generates four sinusoidal signals to drive the motor.

Chapter 4 evaluates the kinematic and actuation system designs through experiments. The input-output relationship of the driving system is carefully analyzed and observed, while the motor performance is measured using weight lifting experiment. The results are compared with theoretical ones and other actuation systems. A finger prototype is finally constructed to investigate the implementation of cylindrical USM.

Chapter 5 concludes this thesis by summarizing the humanoid hand design and its actuation system and proposing future research work.

Chapter 2

Kinematic Design

2.1 Design Philosophy

Most humanoid hands are currently characterized by their dexterity and maneuverability, provided by their high levels of DOF, and anthropomorphic appearance. Particularly, the kinematic structure and finger configuration have been constructed simply referring to human hand model without a second thought. Such design methodology is widely used because it is believed that the closer the kinematic design and number of DOF are to the human hand, the better its ability to reproduce human hand functionality and dexterity. In other words, most kinematic designs of humanoid hand are just a duplicate of the human hand model without a critical analysis on the reasons of doing so.

It is undeniable that after thousand years of revolution, human hand has evolved to be the most sophisticated, dexterous and multi-functional end-effector human kind can ever have. It is therefore justifiable that a humanoid hand design similar to it is able to perform a wide range of tasks. However, a prototype following the kinematic structure of human hand (together with all the DOFs) is usually accompanied with high degree of complexity. Naturally, this kind of complexity is not favorable due to construction, control and maintenance issues. In term of applications, such a sophisticated design could also be an overkill and creates a lot of redundancies. Consider the case where a humanoid hand is needed as the end-effector of elder-care humanoid robot. The daily

elder-care services require probably only a certain range of grasping and manipulation actions. For such structured and pre-defined working environment, it would render an advanced dexterous hand unnecessary. In return, the tasks are reviewed and appropriate structural design is installed for that purpose. This is *task specific design*, which is the core design component in our hand kinematic design.

As opposed to other humanoid hands, the main objective of current humanoid hand research is to design a specific humanoid hand based on predefined working environment. The predefined workspace usually contains a set of grasping and manipulation actions that is needed in an application. The ability to perform this set of grasps or hand motions can be associated with a term called the hand functionality, which by definition, is *the ability to use the hand in everyday activities*. In general, hand functionality can be kinematically described into different groups of hand postures, grasps, and dexterous manipulation that are used to perform various functions such as holding, picking, turning, etc. Therefore, for an application where a certain range of grasping and manipulations is considered, the corresponding level of hand functionality is determined. Based on this, the kinematic design of a specific humanoid hand (with limited hand functionality but sufficient to complete the tasks) can be effectively derived with no excess complexity.

Our philosophy is to achieve that level of hand functionality with the least degree of freedoms (DOF), and hence the lowest complexity. Reducing the number of DOFs without sacrificing the requested hand functionality brings along many benefits. For instance,

- inverse kinematics of the hand is drastically simplified as the number of joints is reduced. Simpler control schemes and controllers can be implemented with more robust performance.

- less actuators implies less space needed for driving electronics, actuation mechanism and associated actuator sensors. A more compact and lightweight kinematic design can be constructed.

- reproducibility of the kinematic structure is easier and cost involved is also reduced.

- better design efficiency since multi-functional robot hands are made possible with low complexity.

To reduce the number of DOFs in humanoid hand, a good understanding on the relation between the hand functionality and the required kinematic structure is necessary. However, this relationship is not clearly defined quantitatively in the literature.

There has been much research published on constructing force closure robotic grasps such as those by A. Bicchi [27], V.D. Nguyen [32] etc. However, researches on multi-fingered grasping analysis have been focused on the geometric aspect of object grasping and manipulation with little attention to the end-effector configuration. Specifically, the functional aspect of the hand grasps, as described in Cutkosky taxonomy [26], is not incorporated with details in object grasping analysis. For example, the motion of objects in some hand grasps are not fully restricted (not a force closure) as described in the grasp functions. These definitions of hand grasp involving its function and closure properties are not critically reviewed. Hence, the following sections will focus on establishing these relations comprehensively. The results are used to develop an effective kinematics design.

Another aspect in the course of kinematic design is the overall anthropomorphic appearance. It is arguable whether a human-hand like kinematic structure is necessary, since the humanoid hand is designed for only a specific range of tasks. It is possible that an odd shape robot hand is more effective in these given tasks, compared to a human-like configuration. However, the design approach here takes into consideration of the end-users' perspective. In general, humanoid hands mainly find their applications in human-robot interaction activities and work on tasks previously done by human hand. Hence, an anthropomorphic appearance is a great advantage because it improves the user experience by its intuitive appearance and user-friendliness. For instance, in teleoperation, operators will need only minimal or no training even for difficult operations. It is therefore part of our design philosophy to integrate anthropomorphic element in the kinematic design.

2.2 The Task Specific Approach

2.2.1 Task Definition

For the purpose of this thesis, the task specific design methodology is demonstrated by the following application scenario:

> *An effective humanoid hand design is proposed to be a multi-functional, ro-*
> *bust and yet simple prosthesis for amputees. User-friendliness, light weight*
> *and cost-effectiveness are among the top priorities. For general use in daily*
> *activities, the humanoid hand prosthesis must be able to perform various basic*
> *grasping actions.*

This is a typical example where a task specific design is appropriate. The top priorities described above suggest that the kinematic complexity should be kept as low as possible. As we know, the degree of complexity is dependent on the level of hand functionality to be designed. In this example, the required hand functionality is defined as *the ability to perform various basic grasping actions in daily activities.* This prescribed requirement can be interpreted as the ability to perform six basic grasps which are widely used in our daily living. When these grasps are properly defined, the development of a humanoid hand capable of doing these is straight forward. Task specification is then completed by simplifying the design with the least complexity.

2.2.2 Hand Functionality and Dexterity

Hand Functionality

The functionality of hand, or any other end effectors, is usually associated with the dexterity of it. In fact, hand functionality and hand dexterity serve as two different bases in humanoid hand design.

The hand functionality, by definition, is *the ability to use the hand in everyday activities.* In everyday activities, the human hand accomplishes different tasks by using different kind of grasping and manipulation actions. However, it is not hard to deduce

that some simple activities are repeated at a daily basis. Therefore, the corresponding grasping actions used for such activities are far more frequent than other rarely used hand actions. Through observation on these frequently encountered hand activities(holding a cup, inserting key, carrying a briefcase, etc), it is found that some fundamental hand grasps are dominant and can be categorized into these six basic hand grasps [31], namely:

1. **Cylindrical Grasp**,

2. **Spherical Grasp**,

3. **Lateral Grasp**,

4. **Palmar Grasp**,

5. **Pinch Grasp**, and

6. **Hook Grasp**.

More details on these grasps will be demonstrated in later sections. These six grasps have been identified as the six most important classes in human hand grasping family and become an indicator for the functionality of humanoid hand. When a humanoid hand is able to perform these commonly used grasps, the hand is considered to be '*functional*'.

Hand Dexterity

On the other hand, the dexterity of hand is *the skillful performance, or ability to use hand in general sense.* The level of hand dexterity is simply an indication of the range of grasping actions and object manipulations that is possible in a humanoid hand. Therefore, the more actions a humanoid hand can perform, the higher is its dexterity. Because of that, highly dexterous humanoid hands are usually constructed with high DOFs in order to perform various human-like fine manipulations.

Design Approach

Both functionality and dexterity defines the ability of using hand, but differentiates each other in terms of everyday usage. It can be seen that a highly functional hand in daily activities is not necessarily having high degree of dexterity and hence does not focus

on having high number of DOFs. In other words, the humanoid hand design approach should adopt an effective methodology that maximizes its performance in most commonly used grasps. At the same time, redundant DOFs that are not necessary for daily tasks should be kept at minimum. In this thesis, the hand design concept is based on a hand functionality approach and thus the kinematic model is geared toward a set of basic hand grasps. The six basic hand grasps, as described above, are expanded from the Cutkosky taxonomy and will be revised with more details on their closure properties in the following sections.

2.3 Basic Grasps and Their Properties

2.3.1 Power and Precision Grasps

Hand grasps are formed and observed in different occasions of human activities. The study of hand grasps is called *prehension*, which can be defined as *the application of functionally effective forces by the hand to an object for a task, given numerous constraints.* There are infinite number of ways to grasp an object by changing the kinematics and kinetics of hand. However, in the study of prehension, hand grasps can be classified according to their functions and tasks. During the analysis of grasping motions, many researchers including Schlesinger (1919) have proposed and reported methods to classify grasping patterns [50]. These classifications of grasping modes depend for many parts on the researchers' personal definitions, and no unified view has been reached at present. From the point of view of grasping tasks, Napier (1956) broadly divided grasping patterns into *Power Grasp* and *Precision Grasp* [51].

Napier has provided an extensive description on the differences between power and precision grasps. Napier defined the power grasp as a grasp involving the contact of palm and fingers with the object, in order to exert the full potential of forearm muscles. In general, the thumb is positioned in plane with palm where fingers are flexed in opposition to the palm. In a precision grasp, the thumb is abducted and rotated opposing the palm. The object is pinched between fingers and opposing thumb, especially between thumb

and index finger when the grasp is used to hold a small object. This type of grasp mainly makes use of finger contacts for fine manipulation.
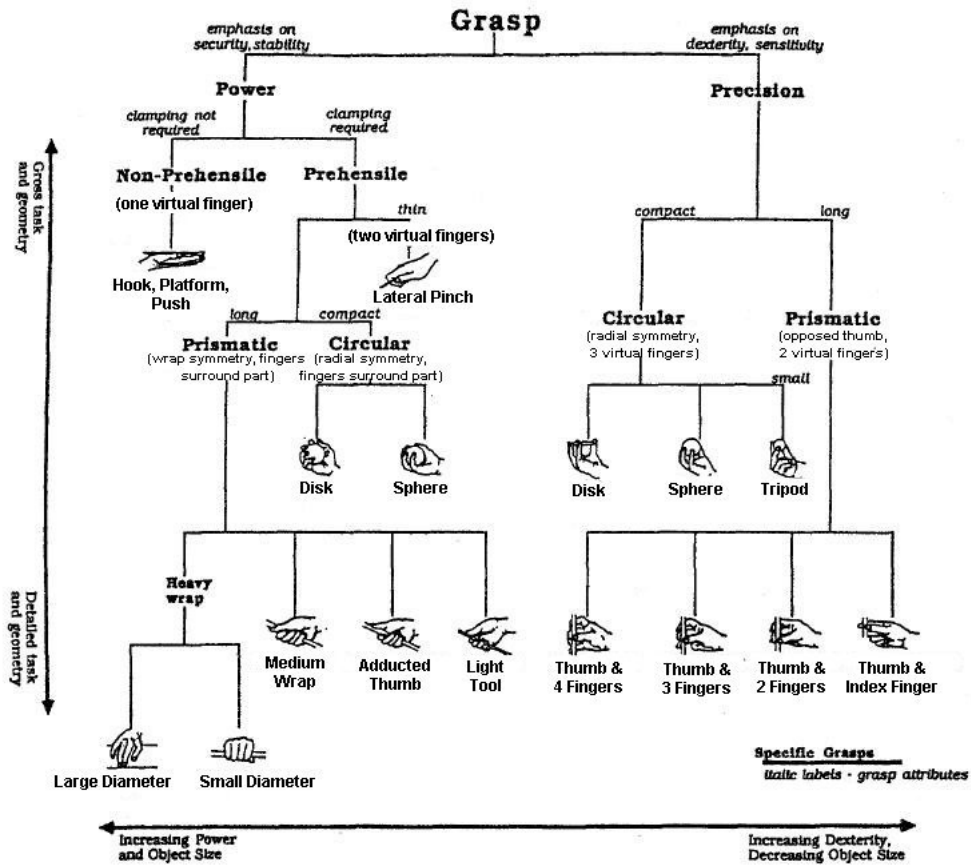
Figure 2.1: Cutkosky Taxonomy of Manufacturing Grasps [31]

Cutkosky classified more grasping patterns by incorporating the detail of objects and the precision of tasks in Napier's concept [26]. As shown in Figure 2.1, the six basic hand grasps can be categorized into these two groups according to their respective functions. The cylindrical, spherical and hook grasps are considered as power grasps. These grasp configurations lack the manipulation ability but are good at providing large contact force and torque to the objects. Pinch and palmar grasps are considered as precision grasp. They are able to provide very fine and precise control on the orientation and position of objects. Lateral grasp can switch in between power and precision grasps, depends on the position of thumb.

Definitions of the six basic grasps are in many ways derived from the concept of

Table 2.1: Categorization of Basic Grasps

Power	Precision	Power/Precision
Cylindrical	Pinch	Lateral
Spherical	Palmar	
Hook		

power and precision grasps. In this thesis, the traditional classification of grasps is further combined with the study of form and force closure to present a more complete definition.

2.3.2 Grasp Definitions

The concept of six basic grasps were originally reported by Schlesinger and later enhanced by Cutkosky through observations on the grasping motions of factory workers [31]. They constitute a significant part in our hand functionality due to their frequent usages in hand activities. Each of them is distinctively identified with respect to the class of objects, as well as the associated functions. On the closure properties of these grasps, it can be best explained using the concept of *form closure* and *force closure*.

Form closure is the ability to prevent motions of object, relying on unilateral, frictionless contacts. When a hand grasp is said to have formed a form closure, the object is not movable in the grasp, assuming no external forces applied to the object.

Force closure can be explained as the restriction of object motions despite whatever external force disturbance. This means any force or torque applied onto the object can be opposed by a combination of contact forces.

Form closure and force closure have been investigated thoroughly by many researchers during the analysis of grasping mechanisms [27, 28]. They have been used in robotics for optimal grasp planning [35]. Many research work were published on the grasp synthesis problem, i.e. given the object geometry, to place contacts so that object motions are restricted [32, 33, 34]. Somov [52] was the first to show that at least seven contact points are needed to form form-closure on any three dimensional polyhedral objects. To solve the grasp analysis problem, i.e. to determine whether an object has any freedoms left, qualitative and quantitative tests were proposed [27, 35]. The idea of partially restrained

grasps were also introduced by Lakshminarayana (1978) [53], to account for some grasps intended to allow only some degree of freedoms to the object. This partial form/force closure property is useful when we need to restrict the object motions within certain directions.

As shown, the grasp closure theories were well established. These analyses are helpful in our development of grasp definitions, particularly the partial form/force closure concept. It has been discovered that the six basic grasps are not necessary to be complete form or force closure. Based on the function of each grasp and combining it with the grasp closure property, a set of redefined definitions for the six basic grasps is established.

For each grasp, a given range of objects with a general shape is defined. With the given objects, necessary contact points and their locations for force closure are derived using grasping synthesis methods. After that, the grasp stability is analyzed to search for optimal contact point locations. Depending on the grasp functionality, a partial force closure may be sufficient. This is because some hand grasps allow the object motions in certain directions, either intentional, or this motion is opposed by the weight of objects, or prevented by contact friction. Therefore, besides the contact point requirement, the grasp definition is accompanied with another set of object constraints, describing its specific functions in object handling.

The six basic grasps can be quantitatively defined, using the analysis of contact points and object constraints. The set of grasp definitions will be derived specifically from the fundamental principles and used for the derivation of hand structure design.

2.3.3   Cylindrical Grasp

Task Definition

Cylindrical grasp is commonly used for cylindrical shape objects such as pipe, bottle, etc. The cross-section of the objects is uniform along the height in general. However it is not necessary to be a circle. This grasp is categorized as one of the power grasps, where palm contact is used. This type of grasp is mainly used for holding objects firmly and transmitting high force/torque to the objects. That is why it is commonly found in

many heavy duty activities such as turning bottle caps, weight-lifting, etc.

One important characteristic of cylindrical grasp is that sliding of object along the height direction is not restricted by any frictionless contact point. In other words, the cylindrical grasp is not a complete form closure grasp. However, it can form complete force closure when contact points with friction cone are applied i.e. any force/torque in that direction is countered solely by friction. This suggests that the cylindrical grasp focuses on providing force/torque restrictions in the other two dimensions (the plane of cross-section area). Based on this grasp property, the contact point system is derived.
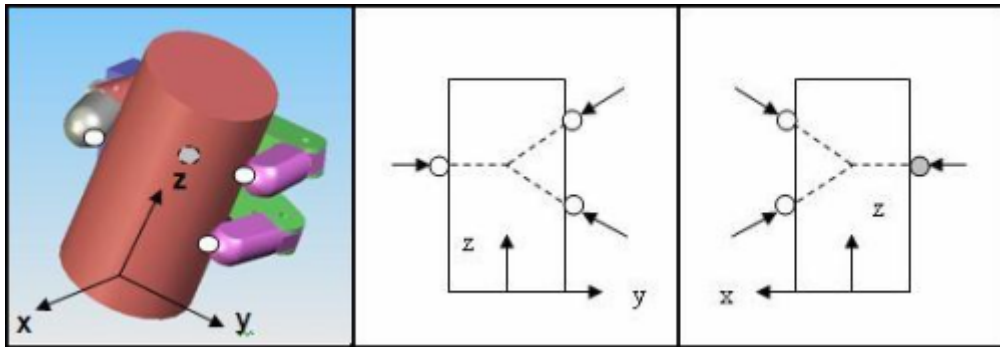
Figure 2.2: Contact Point System of Cylindrical Grasp *(Small white circles represent the contact point. Dashed circle implies the contact point is behind the object.)*

Contact Point System

Let's define the x, y, z-direction of cylinder as shown in Figure 2.2. For a firm grasp the object should be stationary in the XY cross-section plane. In order to attain force closure in x and y direction, a minimum of four contact points is needed as shown. Referring to the middle diagram, the contact points of thumb and finger tips are shown. In the YZ plane, the forces applied should be concurrent and ideally meet at the centre of gravity (CG) of object. The same applies to the remaining contact force exerted by the palm in XZ plane. This configuration prevents motion caused by force/torque exerted in x and y direction.

The sliding of object in z-direction is not prevented by the contact points by definition. If the object is having uniform and circular cross section area, rotation about the z-axis is also allowed. These two object motions are solely opposed by contact friction.

Object Degree of Freedom

Form closure analysis shows that object motions are restricted in the direction of[1]

$$T_x, T_y, R_x, R_y$$

while the DOFs of object are

$$T_z, R_z$$

We have seen that external moments in these two DOFs can be countered by contact point friction. Hence force closure is assured when contact friction is considered.

2.3.4 Spherical Grasp

Task Definition

This grasp is mainly applied for objects having spherical shape. This object classification can be extended to irregular shape objects that are considerably small and graspable within fingers, thumb and palm. In this discussion we limit ourselves in spherical objects for simplicity. In general, the spherical grasp encloses the objects and forms a complete form closure grasp. Again, this is a strong power grasp used for catching, throwing and other daily activities.

Spherical grasp is the only form closure grasp among the six basic grasps. It provides full motion restrictions in all three primary axes, i.e. x, y and z-directions, except the rotation of spherical objects. Unlike cylindrical grasp, it is not very effective at transmitting torques. In other words, the grasp is functional at giving pure active or passive forces. Therefore, the contact point system for spherical grasp concentrates on force restrictions. All rotation restrictions will depend on the contact friction.

---

[1]T and R stand for Translation and Rotation in x, y, z-directions; as defined in Figures 2.2 to 2.7.
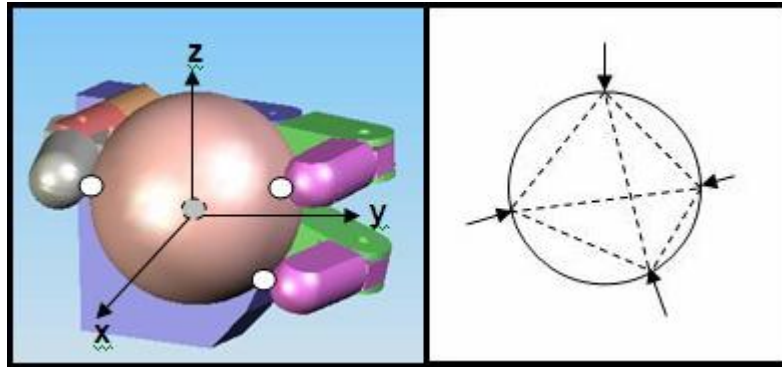
Figure 2.3: Contact Point System of Spherical Grasp

Contact Point System

Studies have shown that any 3D polyhedral object requires seven contact points for form closure. For spherical objects, four triangular tetrahedron contact points structure is the simplest contact point system. This is illustrated in the Figure 2.3. Ideally the four points should be equal distance apart and finger forces are perpendicular to the spherical surface. This combination of four finger forces is able to oppose forces from any direction, which is also the least contact points to maintain form closure for spherical grasp. However, there is a range of possible point locations where form closure can still be maintained. Optimal locations will be deduced when the requirements of other basic grasps are considered.

Object Degree of Freedom

From form closure analysis, object motions are restricted in the direction of

$$T_x, T_y, T_z$$

while the DOFs of object are

$$R_x, R_y, R_z$$

Force closure is possible when all the rotations are opposed by contact friction.

2.3.5 Lateral Grasp

Task Definition

The lateral grasp applies strong opposition force onto lateral objects, namely those with two flat sides parallel to each other and short distance apart. These include plates, sheets, key and so on. In human hand structure, this grasp is formed by the opposition of thumb pulp with the side of index finger. Besides a stable grasp for holding flat objects, the main function for a lateral grasp is to perform twisting actions on lateral objects.

The opposition of thumb with the side of index finger gives prominent clamping force onto the objects. The object experiences forces perpendicular to its lateral surfaces. A lateral grasp clamp is very stable because it doesn't allow object rotations in all directions except the one perpendicular to the surface. This enables lateral grasp to transfer powerful torques to the objects about the two axes along the flat surface (x and y-axes). Lateral grasp is involved in many twisting actions such as bending, key turning, etc.
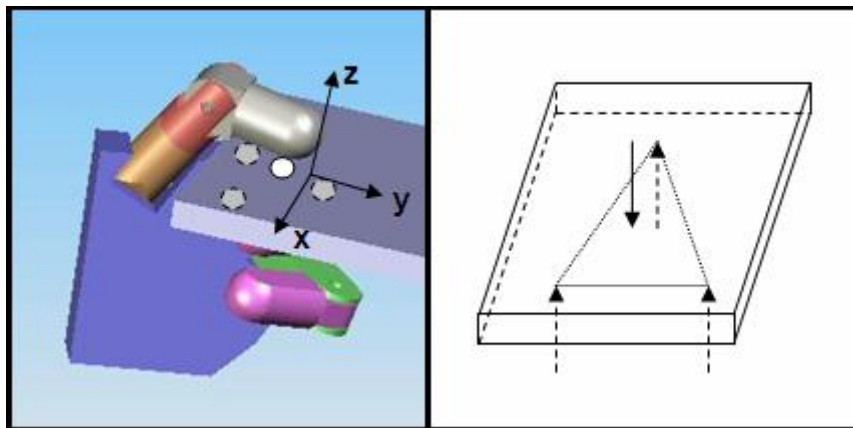

Figure 2.4: Contact Point System of Lateral Grasp *(Upper force must be inside the triangle)*

Contact Point System

To form the contact point system we need to interpret the functions of lateral grasp into closure requirement. The opposition force requires at least two contact points on the flat

surfaces. Let's denote this direction as z-axis. It is clear that to prevent object rotations in x and y directions, at least four points are required (Figure 2.4). That is, one point on one side of the object and three points on the other side. The three points on one side should spread and form a triangle where the fourth point is pointing inside the triangle, in order to oppose any torques in x and y directions.

From the four contact points and the flat nature of lateral objects, we can easily deduce that translational motions in x and y-directions together with rotation in z-direction are not obstructed.

Object Degree of Freedom

From form closure analysis, object motions are restricted in the direction of

$$T_z, R_x, R_y$$

while DOFs of the object are

$$T_x, T_y, R_z$$

Force closure is possible when all the DOFs are restricted by contact friction.

2.3.6   Palmar Grasp

Task Definition

The use of palmar grasp can be found in many tool handling activities. Sometimes it is also called a tripod grasp. In a palmar grasp, fingers and thumb are flexed and wrapped around the side of objects like a "tripod". End of the object can rest on the palm surface for support if fine manipulation is required. The objects can range from flat circular slabs like discs to objects with long cylindrical handle such as sculpture knife. However, the objects must be having rounded cylindrical surface for tripod grasp to be possible.

This tripod grasp formation gives great and fine controllability to one end of the objects. At the same time, other parts are kept steady. This type of object motions is important in writing, crafting, cutting, etc where manipulations of tools are critical.
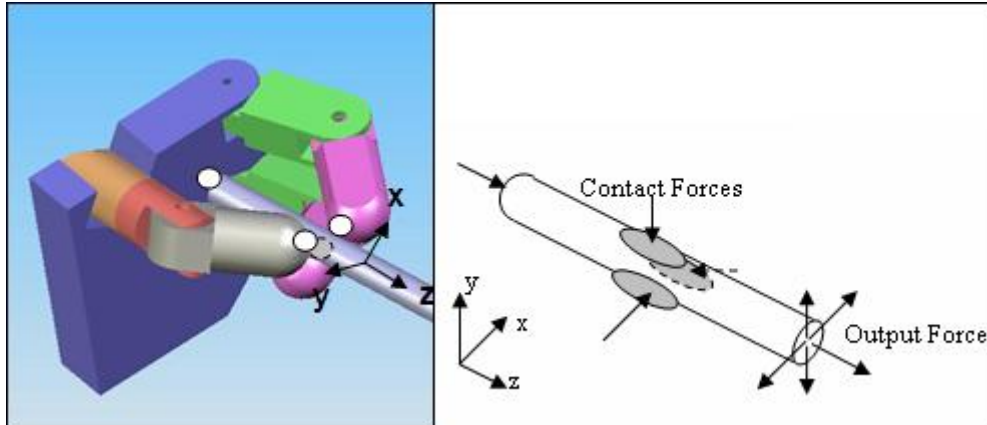
Figure 2.5: Contact Point System of Palmar Grasp

Contact Point System

To perform a tripod grasp onto an object, at least three soft contacts are required (Figure 2.5). The three soft contacts are located on the cylindrical surface, and ideally evenly spaced. End of the object rests on palm surface representing the fourth contact point.

Referring to form closure analysis, grasped objects are restricted in four DOFs; which are translations and rotations in x and y-direction respectively. The translational motion in negative z-direction may also be restricted. z-rotation and positive z-translation are subjected to the contact friction. Grey pads in Figure 2.5 represent the required soft contacts to maintain a tripod grasp. This configuration is designed for fine control of motions and forces at the free tip of objects.

Object Degree of Freedom

Motions of the object are restricted in the direction of

$$T_x, T_y, (T_{z-}), R_x, R_y$$

while the DOFs of object are

$$T_{z+}, R_z$$

Force closure is possible when contact friction is considered.

2.3.7 Pinch Grasp

Task Definition

Pinch grasp makes use of the opposition force between thumb and finger to grasp small objects. Pinch grasp is suitable for objects with any shape; however the object size should be small so that opposition force can be applied on two sides of the objects. The grasping action is similar to an industrial gripper, using simple open and close positions to pick up and drop objects from one place to another.

In a pinch grasp, precision is more decisive than grasping force in maintaining grasp stability. Take the picking task as an example, if the pinch points do not fall into a stable region, the objects will slip away easily. The grasping force is relatively low since forces are applied from finger tips. This fits the pinch grasp into the category of precision grasp. Pinch grasp is important in many delicate actions, such as picking, stacking small objects or arranging items.

Figure 2.6: Contact Point System of Pinch Grasp
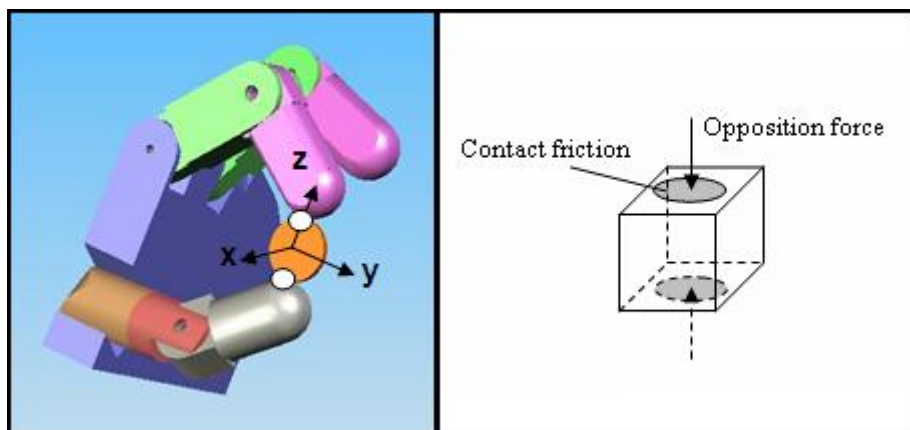
Contact Point System

Formation of pinch grasp is the simplest of all basic grasps. A fundamental pinch grasp requires 2 contact points on each side of the object, where two opposite and equal forces act upon (Figure 2.6). This pair of forces must point towards each other, so that an opposition force is created without introducing any extra torque. In most cases, point of

action for the two forces coincides with centre of gravity of the object.

Pinch grasp has the weakest closure property compared with other basic grasps. Apart from the one dimensional motion restriction along the opposition force direction, other DOFs of the object are susceptible to external disturbance. Under normal circumstance, the pinch points are assisted with contact friction to increase the grasp stability. Note that the contact friction also enables pinch grasp to perform additional force transmitting functions, such as pulling, turning, pushing and so on.

Object Degree of Freedom

From form closure analysis, object motions are restricted in the direction of

$$T_z$$

while DOFs of the object are

$$T_x, T_y, R_x, R_y, R_z$$

The presence of contact friction is necessary in pinch grasp due to large number of DOFs.

2.3.8 Hook Grasp

Task Definition

Hook grasp is the formation of fingers into hook shape, typically used for carrying, hanging and pulling objects. In a hook grasp, fingers are curled into U-shape and aligned together, with the thumb either rests on the object or leaves open. This half-open structure is suitable for grasping objects with handle. The handles can range from flexible strings to solid bars. For some applications hook grasp is used to pull long tubular objects.

Analyzing the class of objects in hook grasp, they are mostly long and cylindrical. The curled and aligned finger structure is also similar to cylindrical grasp. Unlike cylindrical grasp, it doesn't form a complete closure to the objects. This enables fast grasp and release of handles. Besides, hook grasp is primarily used to apply one directional pulling

force, which is used to counter the weight and momentum of objects or human body. There is no opposition force in a hook grasp.
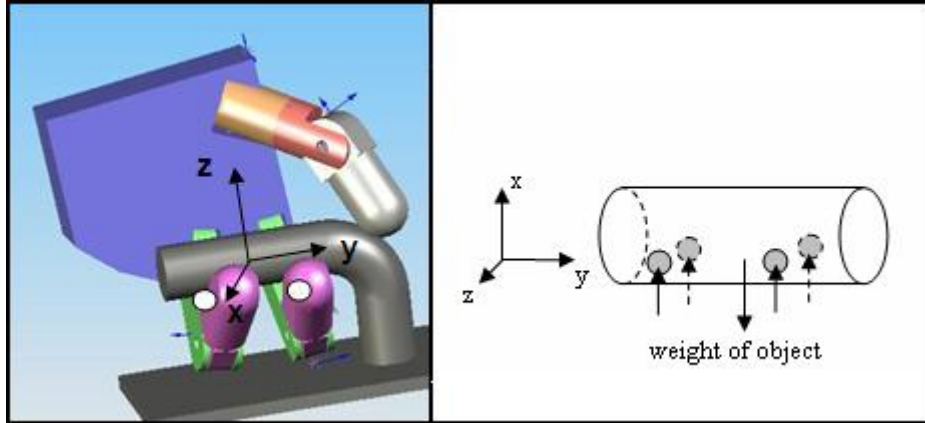
Figure 2.7: Contact Point System of Hook Grasp

Contact Point System

As mentioned, the hook grasp does not form a closure onto the object. This implies that the grasped object has many DOFs. From functional aspect, hook grasp is required to counter motion in only one direction. For that purpose one contact point will be enough. However, for stability reasons more points would be necessary. Since handles are usually long slender objects, three extra contact points will be required to prevent swinging and to ensure the force is transmitted without slippage. The distribution of points is demonstrated in Figure 2.7. Centre of gravity of the object should locate in between the points.

In this configuration the object is restricted except in the y-translation, y-rotation, z-rotation and positive x-translation. Note that the contact points of hook grasp are concentrated at one side of the object. Force closure cannot be attained even with contact friction, as forces in x-translation and z-rotation direction are unable to be opposed.

Object Degree of Freedom

From form closure analysis, object motions are restricted in the direction of

$$T_{x-}, T_z, R_x$$

while DOFs of the object are

$$T_{x+}, T_y, R_y, R_z$$

Force closure is not possible as some degree of freedom are not able to be opposed. A summary of object constraints and free DOFs in all hand grasps is shown in Table 2.2.

Table 2.2: Summary Table of Object Constraints in All Hand Grasps

Hand Grasps	Restricted Motions	Free DOFs
Cylindrical Grasp	T_x, T_y, R_x, R_y	T_z, R_z
Spherical Grasp	T_x, T_y, T_z	R_x, R_y, R_z
Lateral Grasp	T_z, R_x, R_y	T_x, T_y, R_z
Palmar Grasp	$T_x, T_y, (T_{z-}), R_x, R_y$	T_{z+}, R_z
Pinch Grasp	T_z	T_x, T_y, R_x, R_y, R_z
Hook Grasp	T_{x-}, T_z, R_x	T_{x+}, T_y, R_y, R_z

2.4 Prototype Design

2.4.1 Task Specific Implementation

In the previous section, we have defined the given tasks, i.e. the six basic hand grasps. To design a humanoid hand capable of doing all these grasps, requirements from each grasp are combined and compared. The focus here is to meet all the functional aspects with the least complexity, i.e. the lowest number of hand joints.

The contact point analyses have shown the minimum contact points and their locations for all grasps. To further specify the kinematic model of humanoid hand, a specified object size range for the grasps is also derived based on the size of common objects in everyday lives (Table 2.3). With the help of these task definitions, the fundamental design criteria are set.

Table 2.3: Common Object Size Range for the Six Basic Hand Grasps

Hand Grasp	Common Object	Dimension	Minimum Dimension	Maximum Dimension
Cylindrical Grasp	Water Bottle	Diameter	⌀25mm	⌀75mm
Spherical Grasp	Baseball	Radius	12.5mm	37.5mm
Lateral Grasp	Plate	Thickness	∼0	15mm
Pinch Grasp	Coin	Diameter	∼0	⌀20mm
Palmar Grasp	Pen	Diameter	⌀5mm	⌀20mm
Hook Grasp	Handle	Diameter	∼0	⌀25mm

Geometric model of human hand is also studied to improve the allocation of contact points. Human hand has the ability to perform a grasp with the least effort, or the least amount of energy. These finger placements are tracked and recorded in the study. Contact point locations for each grasp are reviewed by combining the contact point systems with human hand grasping behavior. In the process, the point allocations are checked against object restriction requirements to make sure they are consistent.

After formulating the initial hand design, physical constraint of finger links is investigated. The finger links must be rigid and are not interfering with grasped object. The sequential actions of fingers from fully open position to grasp position are simulated. Another aspect is the anthropomorphic appearance of hand structure. This element has been integrated not only in grasping positions, but also in how the humanoid hand approaches and performs the grasps. These are tested in our virtual models, developed using SOLIDWORKS software.

2.4.2 Mechanical Structure

The kinematic design has to fulfill all of the following requirements:

- meet the functional aspects of all six basic grasps,

- form the grasps with more than or equal to the minimum contact points,

- follow the form and force closure properties,

- cover the common object size range for all grasps and

- in the simplest form.
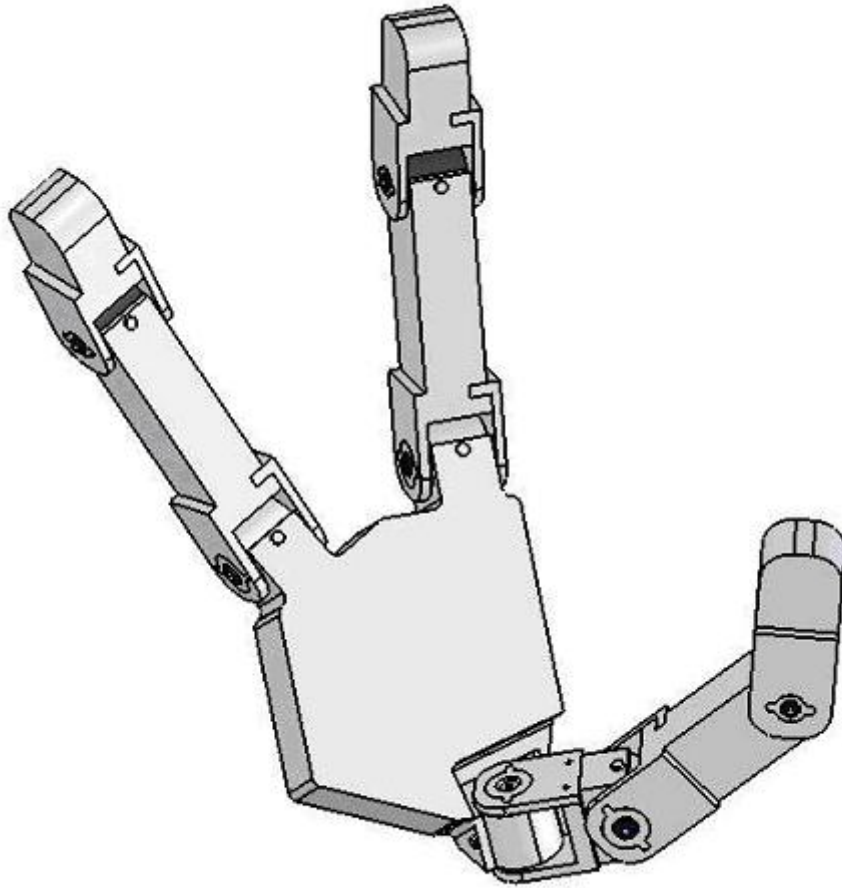
Figure 2.8: Task Specific Humanoid Hand

A basic kinematic model with seven DOFs and three fingers is concluded (Figure 2.8). The low number of DOFs is consistent with our design philosophy. There are two fingers and one thumb. The two fingers contain two DOFs each, with an acute angle of 30 degrees in between. The thumb has three DOFs, where the extra degree of freedom is specially designed to enable the thumb to oppose other fingers and at the same time be perpendicular to the finger plane to form a lateral grasp. Ideally the bottom joint of thumb is a two-DOF joint, but for construction easiness it is replaced by two one-DOF joints. It was designed to have the size of an ordinary human hand, but due to the size constraint of motor, the hand size is scaled up 1.5 times. The dimension from index finger tip to the end of palm is 280mm and thickness is 31mm. Detailed information on

the hand dimensions and assembly are presented in Appendix C.

It is verified that this hand setup is capable of performing all six basic grasps through software simulations (SOLIDWORKS). It is able to satisfy the minimum contact point requirement as stated. The dimension ratio of hand links can be further investigated to increase the hand effectiveness. This improvement is performed under a series of considerations described in the next section.

2.5 Design Analysis

An initial prototype has been designed for the humanoid hand to achieve sufficient hand functionality. At this stage, the design is critically reviewed to deduce the proper linkage dimension ratio and angle for maximum performance. One aspect of optimization is to differentiate the importance of each grasp relative to each other and thus design the hand to perform better in that particular grasp. However, the usage frequencies of these six grasps vary from person to person. In this study, we assume an equal preference in all these six grasps during the design analysis.

In a cylindrical or spherical grasp, the dimension ratio of finger links can be optimized to improve the grasping range. Let's consider a typical scenario where humanoid hand is performing a cylindrical grasp. To be effective, the hand design should be able to grasp the largest possible cylinder/sphere for a given hand size. Using cylindrical grasp definition, the grasp configuration for largest possible cylinder will have the contact points as shown in Figure 2.9. At this maximum grasp limit, fingers are wrapped around the cylinder/sphere and contact points are at the tip of finger, thumb and palm.

For optimization of grasping range, the total hand length, which is represented by the sum of palm length from thumb to finger (n_1), finger middle phalange length (n_2) and finger distant phalange length (n_3), must be at minimum. This suggests that finger middle phalange should be tangential and touch the cross-section circle. The link lengths are related to the cylinder radius r by
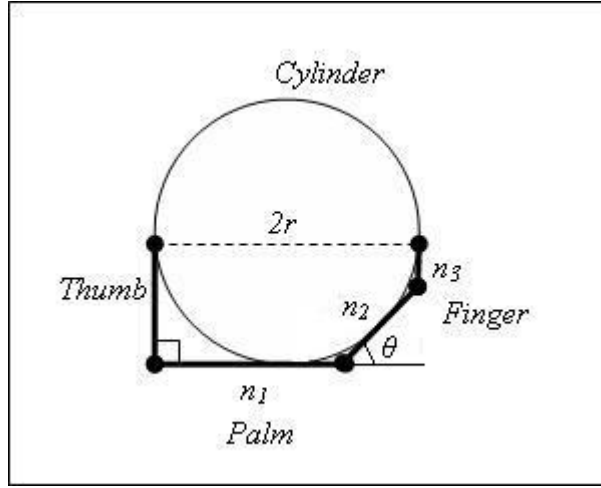
$$2r^2 - rn_1 - n_1n_3 = 0 \qquad (2.1)$$

Figure 2.9: Schematic Diagram of a Cylindrical Grasp at Maximum Grasp Limit

Further specify the angle formed by palm and finger middle phalange as θ. We can derive that

$$n_1 = r + r \left(\frac{\sin \theta}{1 + \cos \theta} \right) \tag{2.2}$$

$$n_2 = \frac{r \left(1 - \frac{\sin \theta}{1 + \cos \theta} \right)}{\cos \theta} \tag{2.3}$$

$$n_3 = r \left(\frac{\cos \theta}{1 + \sin \theta} \right) \tag{2.4}$$

The optimal angle θ can be found by differentiating the sum of links with respect to the angle,

$$\frac{d(n_1 + n_2 + n_3)}{d\theta} = 0 \tag{2.5}$$

and it is deduced that $\theta = \frac{\pi}{4}$. Substituting this value into Equation 2.2, 2.3, 2.4 and it is found that the optimal link ratio is

$$n_1 : n_2 : n_3 = \frac{2}{2 - \sqrt{2}} : 2 : 1 = 53.2\% : 31.2\% : 15.6\% \tag{2.6}$$

and the thumb length must be equal or larger than the maximum radius r.

To guarantee a firm lateral grasp, the dimensions of the thumb and index finger should also be fine-tuned. Theoretically, the thumb phalanges have to be as long as possible to

increase the maximum object thickness in lateral grasp. Location of thumb joint on the palm is strategically measured and placed so that thumb tip contact is always within the contact point triangle (Figure 2.4).

When the hand design is geared towards palmar grasp, one should look at the dimension ratio of fingers and palm. It is found that a hand with small palm and long fingers performs better in palmar grasp. It is also found from stability analysis that the ideal angle configuration is one where the three points of contact are equidistant and 120° apart. This suggests that the fingers and thumb should be of similar length and their tips are able to coincide at the same cross-sectional plane on the object.

For a steady hook grasp, angle between the two fingers should be kept as small as possible. Note that this requirement is conflicting with spherical and palmar grasp requirements where the fingers are required to spread wide. On the other hand, pinch grasp would emphasize the ability of the thumb to oppose other fingers.

Various dimension combinations have been tested for their advantages and disadvantages in all the basic grasps. Through the analysis it is clear that each grasp has its best hand configuration and it is not possible to get the optimum. Therefore, compromises are required when conflicting dimension requirements are encountered. This exercise is performed based on the importance of the different grasps. Since the priorities of the grasps are not set, tradeoff is performed such that the resulting dimension ratio provides maximum grasping range to all grasps. For instance, palmar grasp would require a long finger/small palm combination but cylindrical grasp prefers them in the ratio described in Equation 2.6. In this case the optimal point between the two is chosen based on the grasping range of simulation results.

2.6 Grasp Simulation

The simulation results of humanoid hand in 3D grasping are presented in Figure 2.10 and 2.11. Grasping functionality of the kinematic design is verified. Take note that humanoid hand size is larger than normal human hand due to the motor dimensions. The range of grasped objects to be tested is therefore 50% larger than common object size range

stated in Table 2.3.

In cylindrical, spherical, palmar and pinch grasps, it is observed that the opposition of thumb towards fingers is the most critical. However, lateral grasp would require the thumb to face the side of index finger. These two configurations become possible by using a special 35 degree inclined thumb base joint. The base joint is controlled by one motor to move in between the two configurations. The opposition of thumb is designed at the most desired angle; 180 degree from middle plane of the two fingers. This configuration would provide the firmest grasp and the best force transmission.

2.7   Summary

The design philosophy of humanoid hand kinematics is first introduced. It is proposed that in a structured environment, the kinematic design can be improved and simplified based on task specification. In this study, the task specific methodology is demonstrated by a prosthesis application scenario. Hand functionality needed for this application has been explicitly represented as the ability to perform six basic grasps—Cylindrical, Spherical, Lateral, Palmar, Pinch and Hook Grasps. To investigate the relations between grasping ability and kinematic structure, a set of grasp definitions describing the form and force closure, contact point system and stability is developed. The object constraint requirements are summarized in Table 2.2.

As a result, a humanoid hand prototype with three fingers and seven DOFs is designed with task specific implementation. Anthropomorphic element is integrated into the design for better user experience. A design analysis is also performed to refine the dimension ratio and angle in between the fingers. It is found that the optimal ratio of palm and finger link length in a cylindrical grasp should be 53.2% : 31.2% : 15.6%. Based on equal preference on each grasp, compromises are made during the design process when opposing grasp requirements are encountered. A 35 degree inclined thumb base joint is installed to enable the opposition and orthogonal configuration of thumb with fingers. Grasping performance of the proposed kinematic design is verified through grasp simulation.
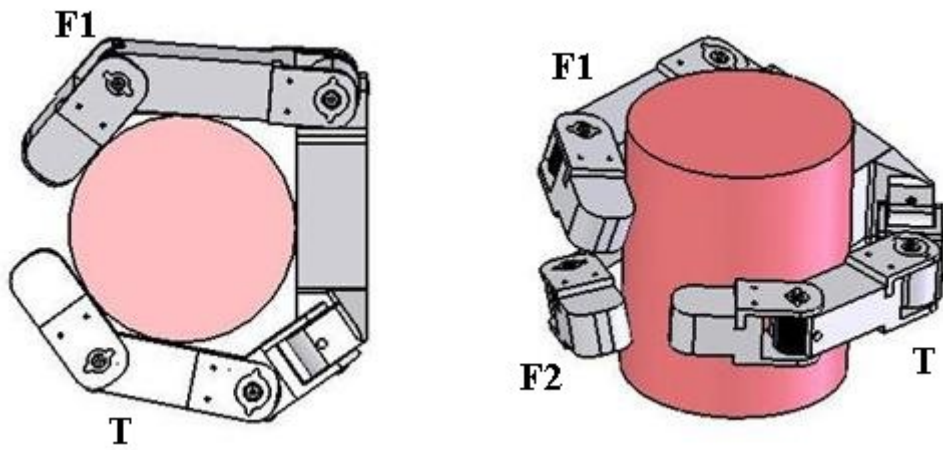
(a) Cylindrical Grasp
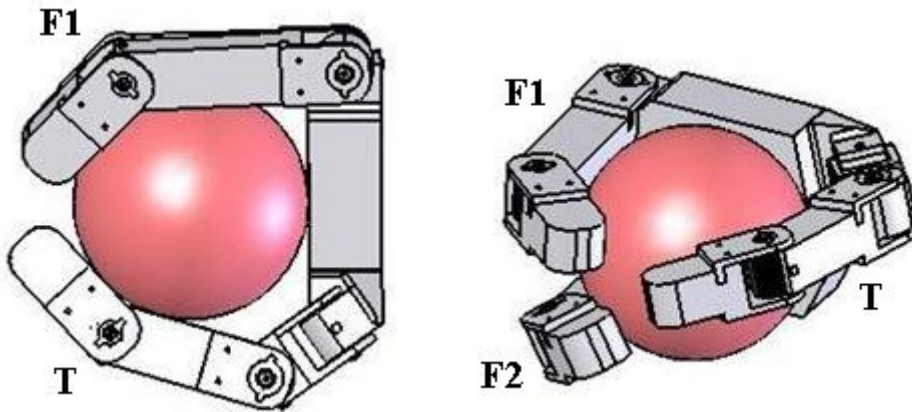
(b) Spherical Grasp
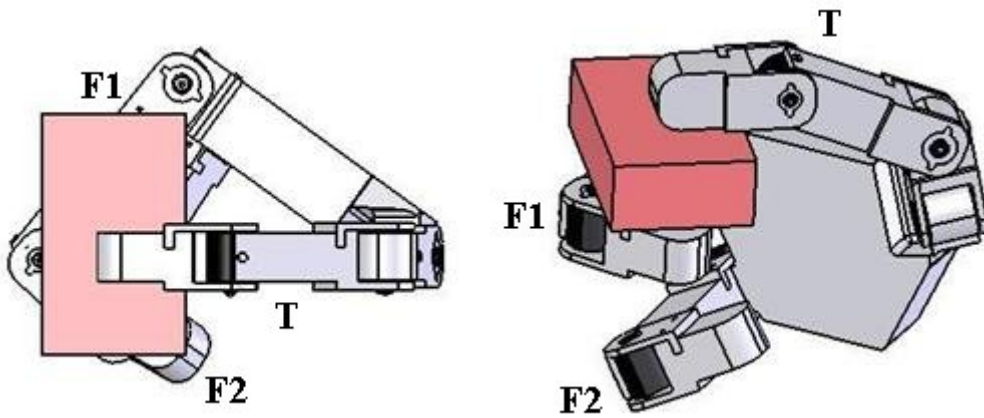
(c) Lateral Grasp

(T—Thumb   F1—Finger 1   F2—Finger 2)

Figure 2.10: Simulation of Cylindrical, Spherical and Lateral Grasps

(a) Palmar Grasp

(b) Pinch Grasp
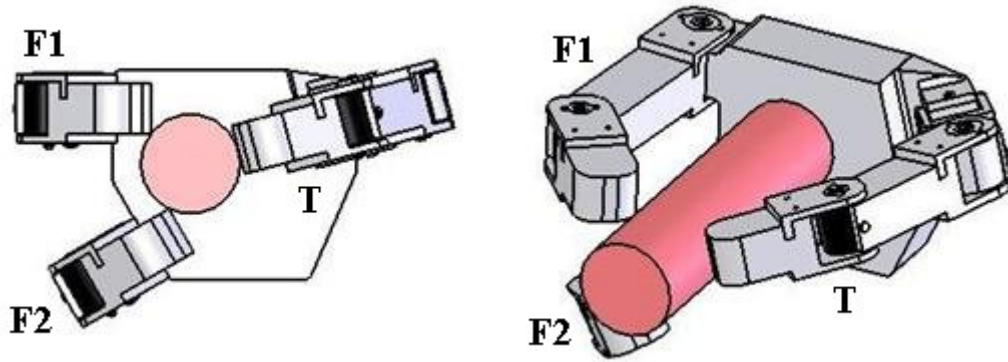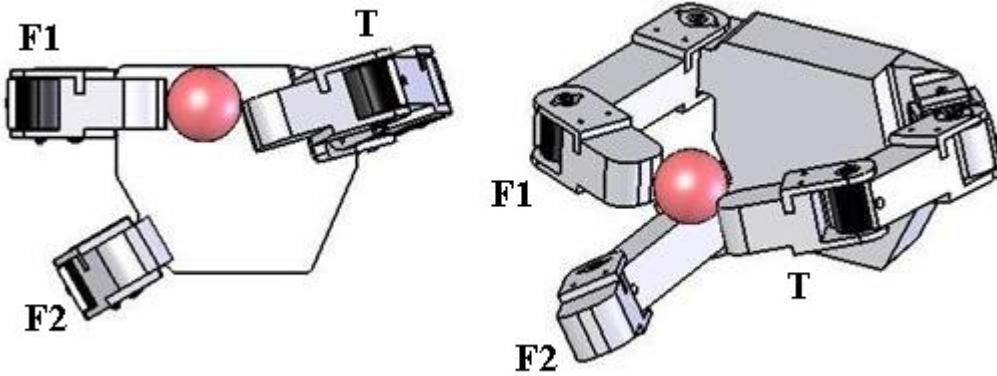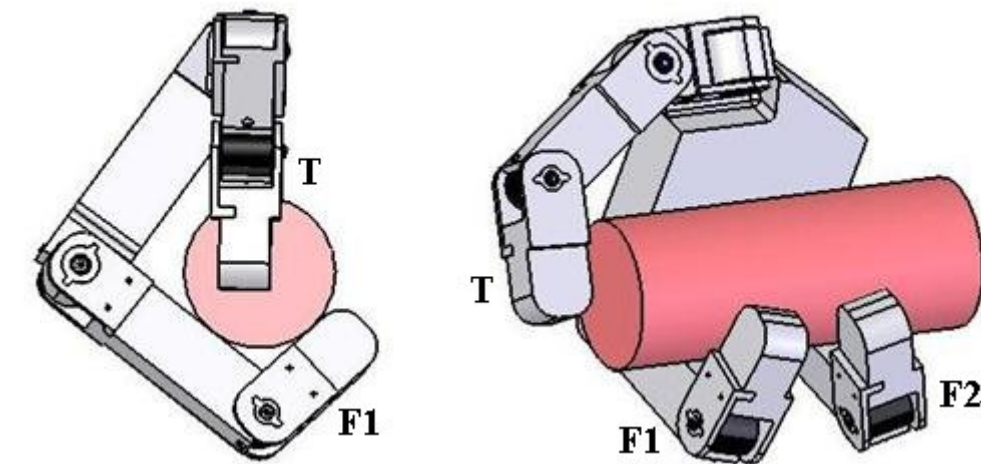

(c) Hook Grasp

(T—Thumb   F1—Finger 1   F2—Finger 2)

Figure 2.11: Simulation of Palmar, Pinch and Hook Grasps

Chapter 3

Actuation System Design

3.1 The Use of Ultrasonic Motor

3.1.1 Power Requirement of Humanoid Hand

The actuation system of humanoid hand is responsible for the realization of different hand functions. These hand functions involve object grasping and manipulations which require a considerable amount of actuation power. Therefore, the torque and force provided by this actuation system has to be strong enough to meet this stringent power requirement. The required strength differs from one design to another for different working environment. However, the power performance of a humanoid hand is generally compared with the average strength of a human hand.

Human Hand Strength

The human hand is regarded as the best multi-functional end-effector, not only because of its dexterous kinematic structure, but also for its superior power and strength. The extraordinary power is provided by human forearm muscle, which can be described as a very effective biological hand actuation system. It combines lightweight, high strength and compactness properties into one robust system. The strength of human hand has been demonstrated in many medical researches and fitness tests. One of these tests is Key-Pinch Test which is a strength test on the maximum pinch force between thumb

and index finger. Young adult population has reported an average reading of 53.6N [54]. In another study by Burdea [55], the maximum controllable force that a human finger can exert is between 40N to 50N. In normal daily activities, comfortable value of exerted force is 15% to 25% of the controllable force. According to a clinical study by Ketchum and Thompson [56], maximum torque of the metacarpophalangeal joint (MCP joint, the base joint) of index finger can go up to 2.7Nm. The torque limits of other joints were deduced respectively by observing the muscle moment arms and phalange lengths. A more extensive human hand strength analysis can be found in [57].

Torque Requirement

The output power of the humanoid hand actuation system should be comparable with the strength of the human hand. Hence, the power requirement of the humanoid hand is standardized based on human hand data described above. Referring to the Key-Pinch Test [54], the amount of torque required in the thumb base joint to generate such force would be 53.6N×6cm = 3.22Nm (Moment arm from the joint to the grasp point is 6cm). Likewise, the maximum torque of finger MCP joint calculated from Burdea's experiment [55] is 50N×7cm = 3.5Nm. It is observed that different measurement results are obtained from these tests. Such discrepancies are probably due to the use of different muscles in different hand configurations. To generalize the power requirement, a standard is set by assuming the maximum controllable fingertip force as 40N. Using the task specific kinematic model and standard hand dimensions (Figure 3.1), torque requirements of each joint are derived in Table 3.1.

Table 3.1: Torque Specification of Hand Joints

Hand Joint	Torque Requirement
Thumb	
Base(MCP) Joint	$40N \times 66mm = 2.64Nm$
Middle(IP) Joint	$40N \times 20mm = 0.80Nm$
Fingers	
Base(MCP) Joint	$40N \times 69mm = 2.76Nm$
Middle(IP) Joint	$40N \times 8mm = 0.32Nm$
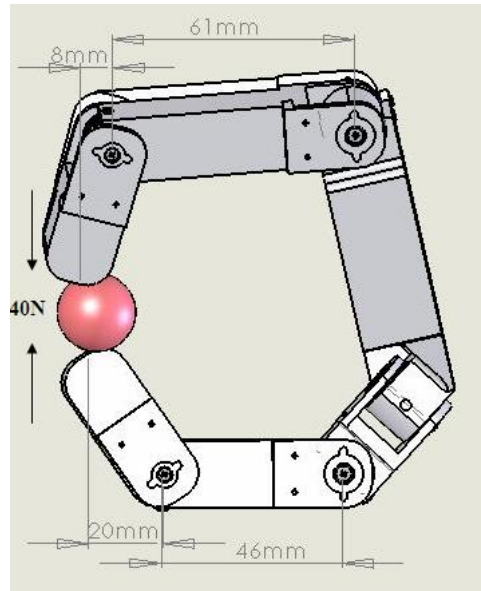
Figure 3.1: Generation of 40N Fingertip Force using Humanoid Hand *(Human Hand Size)*

3.1.2 Current Humanoid Hand Actuation Systems

The most straightforward choice of actuator location for humanoid hands is at or near the finger joint it drives. Hands using this type of actuator placement are called *built-in-actuator type* or *direct-drive* hands. In a direct-drive hand, joint axes are directly coupled to rotors of high-torque actuators and no transmission mechanism is required between the motors and their loads. Because of this, the system has excellent features, such as no backlash, small friction and high stiffness. *Built-in-actuator* system has the following advantages:

- actuators are directly mounted on the joints and therefore the whole actuation system can be integrated into the hand. This design greatly reduces the space required for actuation system, makes the hand more compact and hence enhances the portability of the humanoid hand.

- backlash and tendons stretch non-linearities are avoided, and hence reduces the dynamics complexity.

- distant joints are controlled independent of intermediate joint motions.

- mathematical computations used in force and position control are reduced.

However, difficulties are encountered in mounting the joint actuators in each finger. The most critical one is the space constraint issue. High torque actuators are sometimes impossible to mount on the joints because of their size and shape. Another issue is the weight of actuators could compromise the output torque generated. Therefore, a number of presented designs have utilized a remote drive approach. Mechanical motions are transmitted to finger joints using tendons routed over frictionless pulleys. Humanoid hands of this design are called *wire-driven* type hands and have these merits:

- a considerable reduction in hand weight and joint size, which in turn reduces passive load applied to the actuators and minimizes size of the hand.

- high-power actuators can be used to drive the joints with no space constraint because they are placed outside the hand structure.

- locating actuators away from the hand avoids routing of actuation wires to each joint.

- force, torque and other sensor installations are made easier since space in the fingers is not occupied by the actuation system.

Both actuation system approaches have been broadly used in humanoid hand designs in recent years (refer to Table 1.1). To decide an appropriate actuation system for the task specific humanoid hand, considerations on the power requirement, the general application of humanoid hand and the actuation technology would be necessary.

3.1.3 An Ultrasonic Motor Actuation System

The use of ultrasonic motor actuator is relatively new in humanoid hand designs. As seen in many humanoid hands that have been constructed (Table 1.1), researchers continue to use electric motors or pneumatic actuators in their actuation systems due to their excellent and robust properties. A notable exception is a five-fingered humanoid hand built by Yamano *et al* [12], which has an actuation system using USM and elastic element.

In fact, USM has shown many superior properties and presents itself as a promising humanoid hand actuator. However, the development of a USM driven humanoid hand is not popular because of many practical issues that need to be resolved. In recent years, USM actuator has shown its great potential in other engineering fields. Results can be seen from the success of USM micromotor which is now widely used in many micro-level engineering applications such as advance medical equipment. With these positive technology advancements, the feasibility of USM in a humanoid hand actuation system should be reconsidered.

An actuation system making use of USM is designed in this humanoid hand project. Such implementation is based on the following motivations:

1. *Built-in-Actuation System*: As stated in the task definition, this humanoid hand is designed to be a prosthesis with specified functions. For this type of application where strength, compactness, light weight and portability are equally important, a built-in type actuation system is more favorable. USM has many outstanding properties that make it particularly suitable for compact actuation system. For example, its high-torque low-speed property eliminates the need of speed reduction gear, hence occupies less space compared to other electric motors. Furthermore, the stator-rotor configuration of cylindrical type USM also matches very well with the hand joint in a direct-drive actuation system.

2. *Power Requirement*: According to the fingertip force requirement in Section 3.1.1, a humanoid hand should have a maximum controllable fingertip force of 40N. However, most of the built-in type humanoid hand designs do not have sufficient actuator torque to produce that amount of force. For instance, DLR-II Hand which was driven by custom made brushless DC motor and bevel gears is only capable of applying a fingertip force of 30N. On the other hand, currently commercialized USM still cannot offer significant advantages over conventional electric motor due to its low force transmission efficiency. However, USM possesses a power to weight ratio thousand times larger than electromagnetic motor, and therefore it has the potential to generate greater torque with an efficient motor design. This encourages

the development of a generic USM that is able to outperform electric motors and meets the power requirement.

3. *Breakthrough in Piezoelectric Crystal Research*: PZN-7%PT piezoelectric single crystal with better quality and strength has been successfully developed [58]. This single crystal piezoelectric element, which reported to have properties several times higher than conventional PZT materials, can be used to design stronger USM for high-power applications such as this humanoid hand project. With the presence of new piezoelectric material, development of USM driven hands is now not limited by sub-standard performance of commercialized USMs. Collaboration was made with MICROFINE PTE. LTD., whom is able to provide crystal materials and technical support in the development and evaluation of USM actuation system for this project. Development of custom made single crystal cylindrical USM is thus carried out to investigate the feasibility of such motor.

In the following sections, an actuation system design utilizing cylindrical USM is reported. This system involves a custom made actuator which is developed with novel PZN-7%PT piezoelectric single crystal.

3.2 Operating Principle of Cylindrical USM

3.2.1 Basic Working Principle

A cylindrical USM essentially consists of a cylindrical stator transducer, two rotors and a preload mechanism. The stator transducer is a cylindrical metallic tube with four pieces of piezoelectric element bonded on four sides of the tube. The poling direction of piezoelectric crystals is in the thickness direction. Rotors are made of brass or other metals with high coefficient of friction. The preload mechanism provides and controls the magnitude of the frictional force between the stator and rotor.

The working principle of a cylindrical USM is schematically presented in Figure 3.2. The principle of operation is to vibrate the piezoelectric material using high frequency electrical signal, and this piezoelectric vibration is converted into rotor rotation by mean

(a) Principle of the Cylindrical USM using 2 Bending Modes
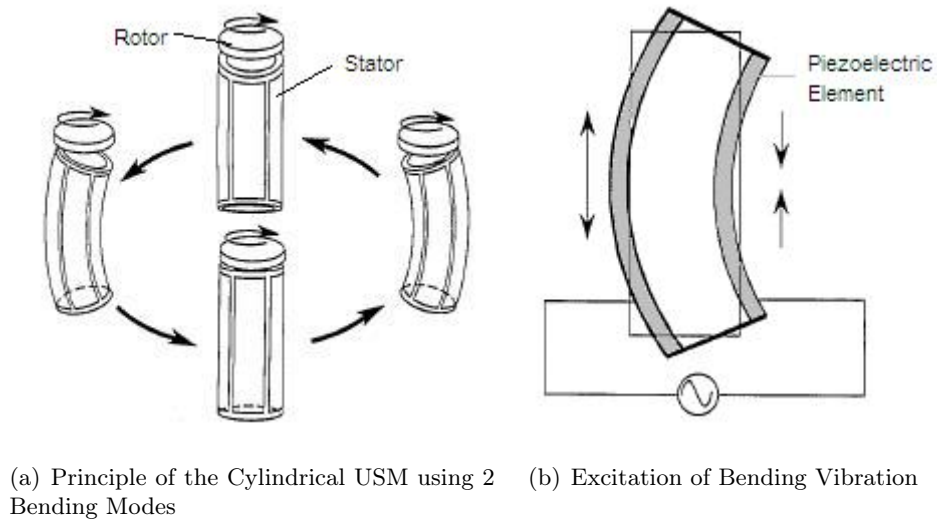
(b) Excitation of Bending Vibration

Figure 3.2: Operating Principle of Cylindrical USM [48]

of contact friction. With one AC electric source connected to one pair of piezoelectric crystals, a fundamental bending vibration of the stator transducer is generated by the transverse piezoelectric effect (i.e. via the d_{31} mode), as shown in Figure 3.2(b). When two fundamental bending modes are excited by two electrical sources with 90 degree phase difference, the rotation vibration of cylindrical stator transducer is excited (Figure 3.2(a)). A one-wavelength traveling wave can then be realized on the end surfaces of stator, causing rotors loaded on the transducer to turn around in the indicated direction through frictional force in the stator-rotor interface. The direction of rotation can be reversed by shifting the phase difference to -90 degree.

3.2.2 Vibration Mode of Cylindrical Stator Tube

In order to maximize the bending vibration amplitude, it is important to configure the operating variables such that the stator transducer vibrates at resonance frequency. To calculate the resonance frequency and understand the patterns and properties of USM stator vibration, several analytical analyses have been proposed, including the simple beam bending model by Morita *et al* [48] and also a more complicated thin circular shell model by Berg [47].

Simple Beam Bending Model

For simplicity, the stator transducer can be model as a simple long beam undergoing free vibration [48]. The motion equation can be described using *Timoshenko's Equation*. Detail derivation of *Timoshenko's Equation* is summarized in Appendix A. This differential equation describes the transverse vibration of prismatic beam, counting the effects of rotary inertia and shearing deformation. It is written as:

$$EI\frac{\partial^4 w}{\partial z^4} + \rho A\frac{\partial^2 w}{\partial t^2} - \rho I\left(1 + \frac{E}{\kappa G}\right)\frac{\partial^4 w}{\partial z^2 \partial t^2} + \frac{\rho^2 I}{\kappa G}\frac{\partial^4 w}{\partial t^4} = 0 \qquad (3.1)$$

w — displacement in the radial direction
z — axial direction of the stator tube
E — Young's Modulus
G — Transverse Modulus
ρ — density of the stator material
I — polar moment of inertia of A
A — cross-sectional area
κ — adjustment coefficient
t — time

The geometric boundary conditions, for a free-free stator vibration are

$$\frac{\partial^2 w(\pm L/2, t)}{\partial z^2} = 0 \qquad \text{and} \qquad \frac{\partial^2 w(\pm L/2, t)}{\partial z^3} = 0. \qquad (3.2)$$

L — length of the stator

From the eigenvalue solutions of boundary conditions, the natural vibration frequencies ω_i and the corresponding mode shape $W_i(z)$ of stator transducer can be obtained as:

$$\omega_i = 2\pi f_i = \left(\frac{\alpha_i}{L}\right)^2 \sqrt{\frac{EI}{\rho A}\left[1 - \frac{I}{2A}\left(\frac{\alpha_i}{L}\right)^2\left(1 + \frac{E}{\kappa G}\right)\right]} \qquad (3.3)$$

$$W_i(z) = C_i\left[\sin\left(\frac{\alpha_i}{2}\right)\cosh\left(\frac{\alpha_i}{L}z\right) - \sinh\left(\frac{\alpha_i}{2}\right)\cos\left(\frac{\alpha_i}{L}z\right)\right] \qquad (3.4)$$

where C_i are constants to be determined and $\alpha_i = (i + \frac{1}{2})\pi$ are frequency parameters. Fundamental resonance frequency ω_1 and bending mode shape $W_1(z)$ are utilized in the

cylindrical USM model. Therefore, fundamental frequency parameter α_1 is used in the calculation, which has a value of 4.7 ($i = 1$).

Equation 3.3 and 3.4 can be used to determine the trajectories of elliptic motion of particles on the stator surface, and then estimate the rotational speed of motor. However, this model is valid under the assumption that length of the stator is five times or more than the stator diameter. For short cylindrical USM designed in this project, Timoshenko's model alone is not enough to provide an accurate estimation.

Thin Cylindrical Shell Model

The cylindrical stator can also be modeled as a circular cylindrical shell using Flügge's shell vibration theory [47]. In the derivation of *Flügge's equations*, the following assumptions for the stator shell are made:

- All points that lie on a normal line to middle surface before deformation stay on the same line after deformation.

- Displacements are small compared to the shell thickness.

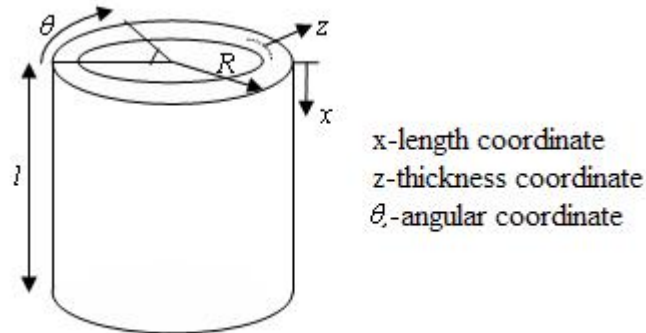- The normal stresses in the thickness direction are negligible.

Figure 3.3: Coordinate System of A Circular Cylindrical Shell

Consider an elastic circular cylindrical shell with the coordinate system defined as shown in Figure 3.3. The cylindrical coordinates are denoted correspondingly by x, θ and z and the displacements in these three directions by u, v and w respectively. Starting from

Newton's Law of Motion, and relating the resulting forces and moments with stress, strain and displacement equations, the equations of motion for thin circular cylindrical shell are derived. The *Flügge's equation* describing the dynamics of stator can be written in matrix form:

$$\Im \{u_i\} = 0 \tag{3.5}$$

where $\{u_i\} = \begin{bmatrix} u \\ v \\ w \end{bmatrix}$ is the displacement vector and $\Im$ is a matrix differential operator,

$$\Im = \Im_{D-M} + k\Im_{Flügge} \tag{3.6}$$

k — thickness parameter, $k = \frac{h^2}{12R^2}$
h — thickness of the shell
R — radius of the shell

where $\Im_{D-M}$ is an operator according to Donnell-Mushtari theory, assuming bending rigidity negligible. $\Im_{D-M}$ is derived as

$$\begin{bmatrix} \frac{\partial^2}{\partial s^2} + \left(\frac{1-\nu}{2}\right)\frac{\partial^2}{\partial\theta^2} - \Omega^2\frac{\partial^2}{\partial t^2} & \left(\frac{1+\nu}{2}\right)\frac{\partial^2}{\partial s\partial\theta} & \nu\frac{\partial}{\partial s} \\ \left(\frac{1+\nu}{2}\right)\frac{\partial^2}{\partial s\partial\theta} & \left(\frac{1-\nu}{2}\right)\frac{\partial^2}{\partial s^2} + \frac{\partial^2}{\partial\theta^2} - \Omega^2\frac{\partial^2}{\partial t^2} & \frac{\partial}{\partial\theta} \\ \nu\frac{\partial}{\partial s} & \frac{\partial}{\partial\theta} & 1 + k\nabla^2\nabla^2 + \Omega^2\frac{\partial^2}{\partial t^2} \end{bmatrix} \tag{3.7}$$

and $\Im_{Flügge}$ is a modifier for Flügge's Theory,

$$\Im_{Flügge} = \begin{bmatrix} \left(\frac{1-\nu}{2}\right)\frac{\partial^2}{\partial\theta^2} & 0 & -\frac{\partial^3}{\partial s^3} + \left(\frac{1-\nu}{2}\right)\frac{\partial^3}{\partial s\partial\theta^2} \\ 0 & 3\left(\frac{1-\nu}{2}\right)\frac{\partial^2}{\partial s^2} & -\left(\frac{3-\nu}{2}\right)\frac{\partial^3}{\partial s^2\partial\theta} \\ -\frac{\partial^3}{\partial s^3} + \left(\frac{1-\nu}{2}\right)\frac{\partial^3}{\partial s\partial\theta^2} & -\left(\frac{3-\nu}{2}\right)\frac{\partial^3}{\partial s^2\partial\theta} & 1 + 2\frac{\partial^2}{\partial\theta^2} \end{bmatrix} \tag{3.8}$$

where $\Omega^2 = \frac{\rho(1-\nu^2)R^2}{E}$, $\nabla^2 = \frac{\partial}{\partial s^2} + \frac{\partial}{\partial\theta^2}$ and $s = \frac{x}{R}$.

ρ — density of shell
ν — Poisson's Ratio, and
E — Young's Modulus

As seen above, the three differential equations are of eighth order. We are interested in the closed form solutions for u, v and w when the stator vibrates at its resonance frequency. Boundary conditions are assumed for a free-free vibration. At these boundaries, the summation of shear force and moment resultants is equal to zero. We could predict that the stator shows periodic behavior with respect to time and the circumferential angle θ is preserved in the solution functions for u, v and w. The periodic variation with respect to s is generalized to an exponential function. Hence, the displacement functions at resonance frequency can be found in the form of

$$u = A e^{\lambda s} \cos n\theta \cos \omega t \tag{3.9}$$

$$v = B e^{\lambda s} \sin n\theta \cos \omega t \tag{3.10}$$

$$w = C e^{\lambda s} \cos n\theta \cos \omega t \tag{3.11}$$

where n is the number of circumferential waves, A, B, C and λ are undetermined constants and ω is the resonance frequency.

The above functions describe the mode shapes and resonance frequencies of stator. The constants can be determined by substituting these functions into the equations of motion, which leads to a set of homogeneous equations. For a non-trivial solution, an eighth order characteristic equation in terms of ω and λ is obtained. A more detailed derivation of the circular cylindrical shell dynamics can be found in Appendix B. The cylindrical shell model presents a more complete dynamic analysis and is not limited to long beam shell structures. However, this modeling method involves many assumptions and estimations that can affect the accuracy of rotational speed and torque approximations.

3.2.3 Estimation of Rotational Speed and Torque

Predictions of rotational speed and torque of the cylindrical type USM have been presented based on various dynamic models. To estimate the output torque, Morita *et al* [48] simplified the stator wall as a bimorph and then estimated the bending displacement

and introduced a force factor for torque calculation. Deriving from the bending displacement of simple beam model, the bending curvature and induced displacement in length direction are related to the strain and piezoelectric effects. The *maximum attainable rotational speed*, ω_R, in rpm under the condition of no slippage between stator and rotor is given by [58]:

$$\omega_R(\text{in rpm}) = \frac{15 Q f_r g_1 L^2 V_{p-p}}{A_o r_o^2} \tag{3.12}$$

Q — quality factor
f_r — driving frequency
V_{p-p}— applied peak to peak voltage
L — length of the stator
r_o — outer radius of the stator
g_1 — properties of active piezoelectric materials
A_o — a function of frequency constant and is given below

$$A_o = \frac{-\alpha_1 \sin(\alpha_1/2) \sinh(\alpha_1/2)}{\sin(\alpha_1/2)\cosh(\alpha_1/2) - \sinh(\alpha_1/2)\cos(\alpha_1/2)}$$

where α_1 is the fundamental frequency parameter. The cylindrical USM drives the rotor through frictional force F_f, which increases proportionally with the preload force F_p. It is noted that no slippage condition for maximum rotation speed is maintained when $F_f < \mu F_p$, where μ is the coefficient of friction between stator and rotor. However, a large preload force is not favorable as this will reduce the efficiency of force transmission. In general, motor torque τ generated is directly proportional to the frictional force F_f in the stator-rotor interface. To estimate the motor torque, the dynamics of friction force interface needed to be understood but it has been difficult to be modeled. However, the maximum output torque, τ_{max}, can be approximated by assuming that it occurs when preload force applied to clamp the stator is sufficiently high to prevent free vibration. Under this absolute clamping condition, no strain is expected in the piezoelectric plate as it is being offset by the preload force. Therefore, *maximum motor torque τ_{max}* is approximated as [58]:

$$\tau_{max} = -\frac{1}{2}\mu r_o g_2 V_{p-p} \tag{3.13}$$

where g_2 is a function of the dimensions and properties of the piezoelectric active elements.

From Equation 3.12 and 3.13, the approximate maximum rotational speed and motor torque are directly proportional to the peak to peak voltage V_{p-p} applied across the piezoelectric elements. To improve the motor performance, cylindrical USMs are usually driven by high-amplitude voltage sources. However, it should be noted that the voltage amplitude is limited by properties of the piezoelectric elements and electrical impedance of the motor. Extremely high voltage may cause overheating and damage the piezoelectric materials. Besides that, the preload force F_p should also be controlled to prevent slippage between rotor and stator, as well as low efficiency due to frictional loss.

The actual rotational speed and motor torque are expected to be smaller as mechanical and heat losses are neglected in the dynamic models. In addition, the two equations were derived based on a simple beam model, which assumes that the stator length dimension is five times larger or more than the stator diameter. Inaccuracy could be significant as the dimension of motor design is not within the theory assumption.

3.3 Fabrication of Cylindrical USM

3.3.1 Structural Design of USM

As a requirement for the actuation system design, a series of cylindrical USMs with different sizes would be required to accommodate for different torque specifications at each joint. In this project, three similar USMs but with different sizes (and hence different power performance) are built, which are planned to be mounted on the *finger middle joint* (lowest torque), *finger base joint* and *thumb base joint* (highest torque). As an easy reference, the three motors are denoted as **Motor S**, **Motor M** and **Motor L**, according to their sizes from the smallest to the largest.

Stator Design

An actuation system using the built-in-actuator approach is constructed to eliminate the need of an external driving box. In order to mount the actuators into the joints directly, the motor size has to be close to or smaller than the size of the humanoid hand joints. Based on the measurements of a normal human hand, appropriate dimensions for the motor stators are concluded (Table 3.2).

Note that, the stator length is restricted to 20mm, an upper limit for finger width. Another important observation is that these stator dimensions do not follow the dimension assumption stated in the simple beam model. This would affect the estimations of rotational speed and motor torque.

Table 3.2: Stator Dimensions

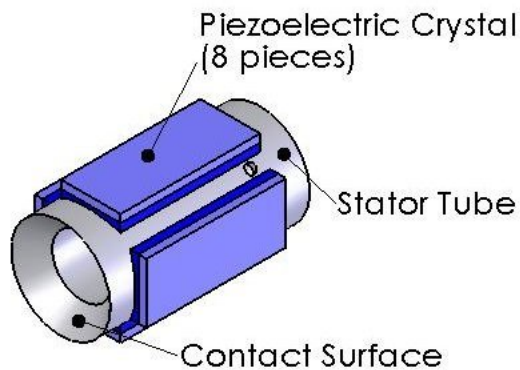|	**Stator Dimension**
Motor S	20mm length × 10mm diameter
Motor M	20mm length × 15mm diameter
Motor L	20mm length × 20mm diameter

Figure 3.4: Stator Design

Figure 3.4 shows the mechanical structure of a motor stator (Motor S). The aluminum circular cylindrical stator transducer has four sides trimmed off to accommodate four pairs of piezoelectric crystals. The two end surfaces, which act as the contact surfaces of stator and rotor, are also trimmed at an angle perpendicular to the stator bending

motion for maximum force transmission. This contact angle β can be estimated from the arc tangent of the ratio between the lengthwise displacement u and bending displacement W at the end surfaces:

$$
\begin{aligned}
\beta \ &= \arctan\left(\frac{u\langle L/2\rangle}{W\langle L/2\rangle}\right) \\
&= \arctan\left(\frac{2rA_o}{L}\right)
\end{aligned}
\tag{3.14}
$$

Rotor Design

The motor rotor design integrates a few new features that could improve the motor performance (Figure 3.5):

1. Extra material is added to the original rotor plate, extended toward the inner stator space. This extra mass increases its moment of inertia and thus provides higher and more stable motor torque.

2. One of the rotors has its core removed to house the preload spring. This design can shorten the shaft and make the design more compact.

3. An engagement mechanism is introduced in between the two rotors to prevent the rotors from rotating at different speeds.
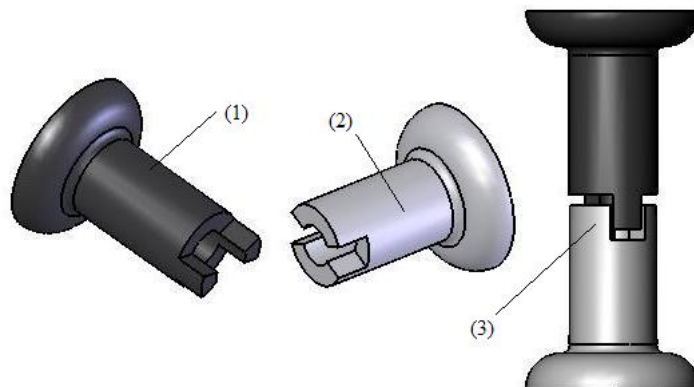

Figure 3.5: Rotor Design with New Features

Motor Shell and Support

The stator is required to be supported at its nodal points, which are the points where no or minimum deflection is observed, for a free-free stator vibration. Location of the nodal points can be estimated using the mode shape equation $W(z)$ (Equation 3.4 in Section 3.2.2). Substituting stator dimensions into the equation, the fundamental mode shape is then plotted (Figure 3.6(a)), where the nodal points are located $\pm$**5.525mm** from the stator centre. A motor shell incorporates the nodal support feature is designed (Figure 3.6(b)).
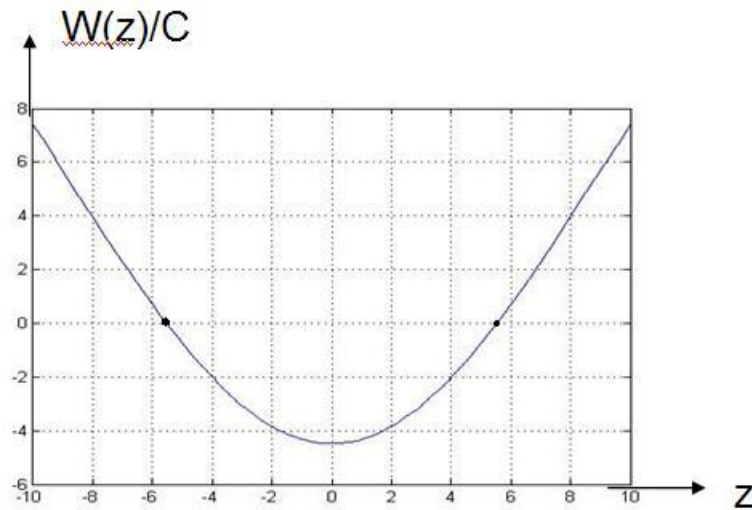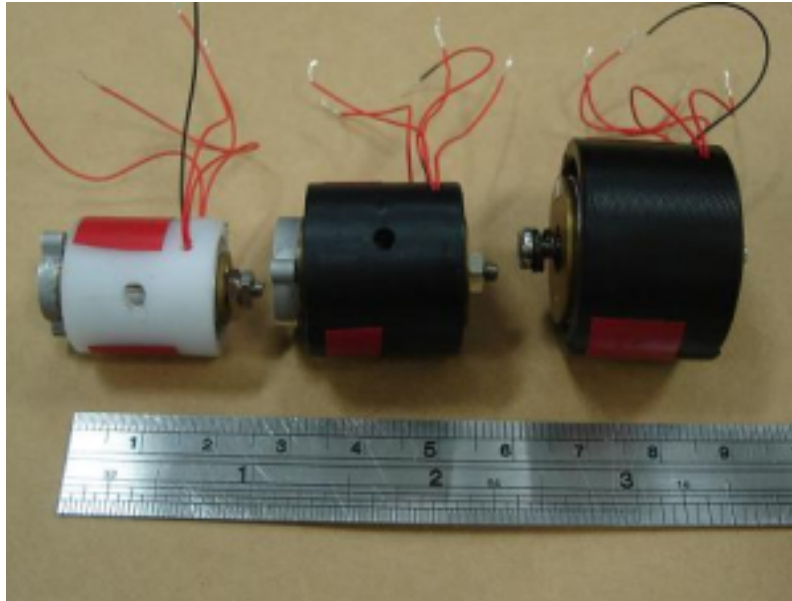

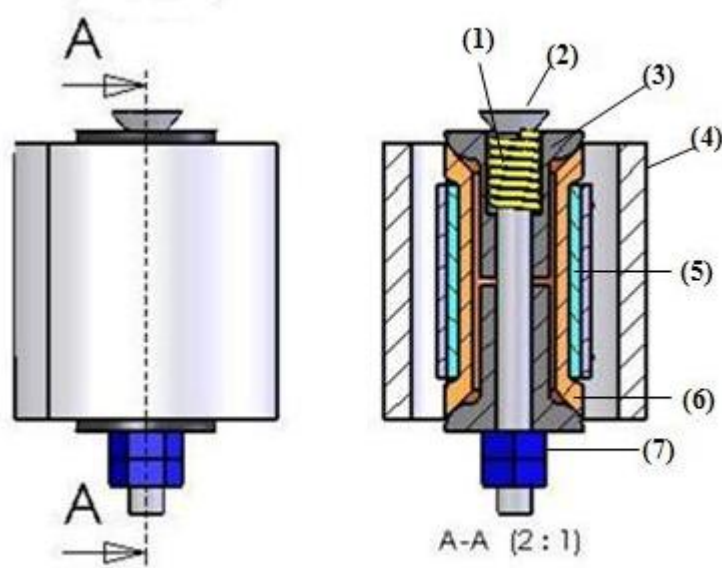(a) Fundamental mode shape $W(z)$ and Nodal Points
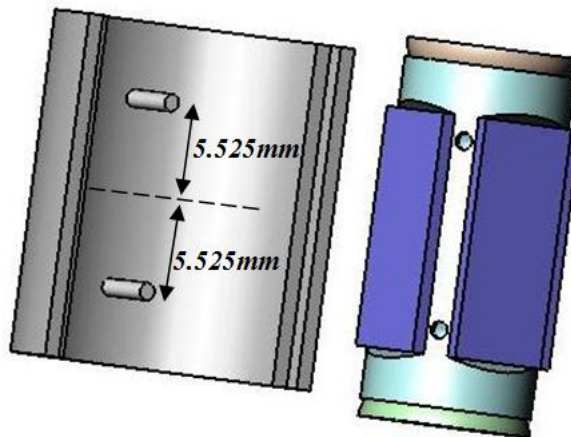
(b) Motor Shell Design

Figure 3.6: Motor Shell with Nodal Supports

(a) Cylindrical USMs of Different Sizes

(b) Cross-section View of Motor S

1)Spring   2)Shaft   3)Rotor   4)Shell   5)Piezocrystals   6)Stator   7)Nut

Figure 3.7: Cylindrical USMs

Motor Assembly

Figure 3.7(a) shows the three cylindrical USMs (Motor S, Motor M and Motor L) fabricated and assembled for this project. The cross-section of cylindrical USM is shown in Figure 3.7(b). The stator is clamped by two rotors using elastic spring. The springs provide the preload, which is necessary to generate frictional force in the stator-rotor interface (Table 3.3). For stronger motor output torque, two thin piezoelectric crystals bonded in pair are used instead of one single crystal. This can increase the electric field across the crystal which is a variable proportional to the motor output. Four electrodes are evenly pasted on the middle layer of piezoelectric crystal pairs. Stator and outer surfaces of the crystal pairs are connected together to form a common ground (Figure 3.8). During motor operation, the four electrodes are excited by four sinusoidal voltage signals with 90 phase difference.

Table 3.3: Properties of Springs Used for the Motor Assembly

Spring Properties*	Motor S	Motor M	Motor L
Part Number	SSC-021AB-2M	SSC-026B-2M	SSC-032C-1M
Outer Diameter (mm)	3.76	4.57	6.10
Free Length (mm)	7.94	7.94	7.94
Max Spring Force (N)	17.77	29.99	44.43
Spring Constant k (N/mm)	4.38	8.22	10.84

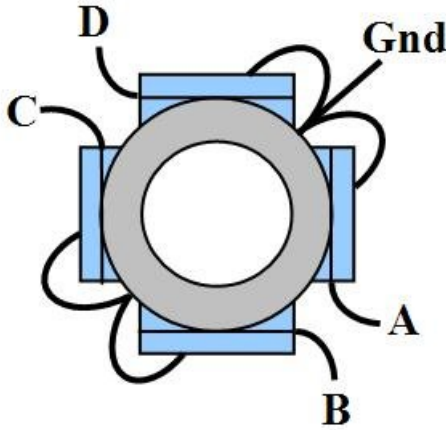*Reference from SHINCOIL Spring Catalogue

Figure 3.8: Schematic Diagram of the Electrode Connections

Detailed information on design and dimensions of the motor parts and assembly is attached in Appendix C.

3.3.2 PZN-7%PT Single Crystals and Their Properties

The construction of cylindrical USMs makes use of novel PZN-7%PT single crystal, a new generation of piezoelectric element. This single crystal, which is developed by Mi-crofine Materials Technologies Pte. Ltd., is prepared by a proprietary flux growth technique that promotes growth of large size crystals (wafers up to 25mm edge length). Compared to conventional PZT piezoelectric materials, the single crystal not only pos-sess good compositional uniformity and superior dielectric and piezoelectric properties, but also insensitive to compositional variations in the material. Table 3.4 shows general properties of a PZN-7%PT single crystal resonator.

Table 3.4: Specifications of PZN-7%PT Single Crystal

	PZN-7%PT Single Crystal
Poling field(kV/mm@R.T.)	0.7~0.8
Depolarization Temperature($^\circ C$)	~100
Loss K^T(@1kHz)	6700-8000
k_{31}	0.80-0.85
d_{31}(pC/N)	$1400 - 1700^*$
s_{11}^E(pm^2/N)	~40

*obtained with a Berlincourt-type meter

Based on the motor configuration and direction of the applied voltage, poling direc-tion $(110)^L \times (01T)^W \times (001)^T$ and a cutting angle of 45° is used during the crystal preparation. Dimensions of piezoelectric single crystals are summarized in Table 3.5, together with their resonance, anti-resonance frequencies f_r, f_a and capacitance C_p at room temperature. Note that these properties are dependent on temperature changes during motor operation. Samples of piezoelectric crystal are shown in Figure 3.9.

Table 3.5: Dimensions and Properties of Crystals used in the Motors

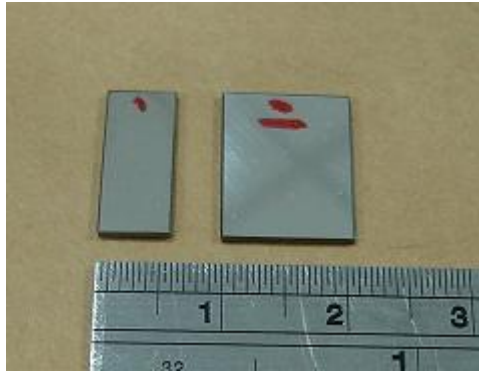|	Motor S	Motor M	Motor L
Piezoelectric Crystal Dimensions			
Length (mm)	14	14	14
Width (mm)	6	9	11
Thickness (mm)	0.8	0.8	0.8
Resonance Frequency f_r (kHz)	59.8~63.1	56.07~59.3	52.37~56.4
Anti-resonance Frequency f_a (kHz)	85.41~91.8	76.6~79.5	69.3~73.1
Capacitance C_p (nF)	4.45~5.80	8.37~9.45	9.50~11.94

Figure 3.9: Piezoelectric Single Crystals Used in Motors

3.3.3 Determination of Driving Frequencies

Crystals are bonded onto the stator according to the configuration described in Figure 3.8. Since mechanical resonances of the stator model and resonance frequencies of the piezoelectric crystals are not the same, the combined stator-crystal assembly exhibits different resonance properties. Using an Impedance Analyzer, resonance properties of the three motor stators are obtained (Figure 3.10~3.12). From the graphs, frequencies correspond to the lowest impedances would drive the stators at resonance state. However, the actual resonance frequencies of assembled motor are slightly lower than the measured values. This is because the preload force imposed by the spring affects the free vibration and lowers the resonance frequency of the stator.

A resonance frequency test is performed by operating the motors using a four-channel Frequency Generator. Sinusoidal signals of fixed amplitude and variable frequencies are used to drive the motor and the corresponding motor speeds are recorded. The motor

achieves maximum rotational speed at its resonance frequency f_{mr} (Figure 3.13). This frequency represents the optimal driving frequency. In a similar fashion the optimal driving frequencies for the other two motors are obtained. The optimal driving frequencies and average motor capacitance C_m measured on each electrode are tabulated in Table 3.6. Note that resonance frequencies of the assembled motors will vary with respect to preload force and temperature, but the changes are not significant.
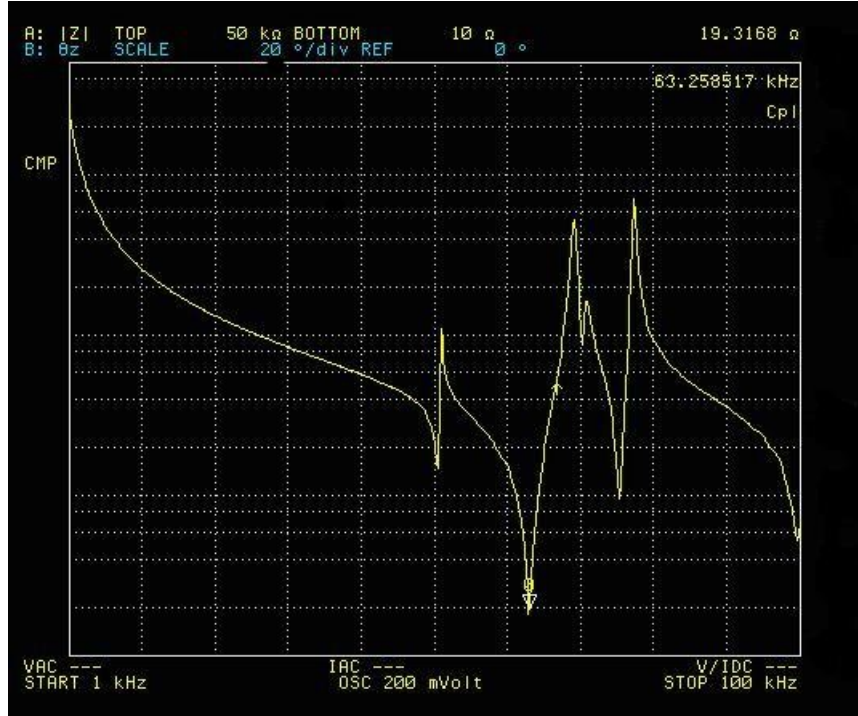

Figure 3.10: Motor Impedance versus Exciting Frequency (Motor S)

Table 3.6: Driving Frequencies and Capacitance of the Motors

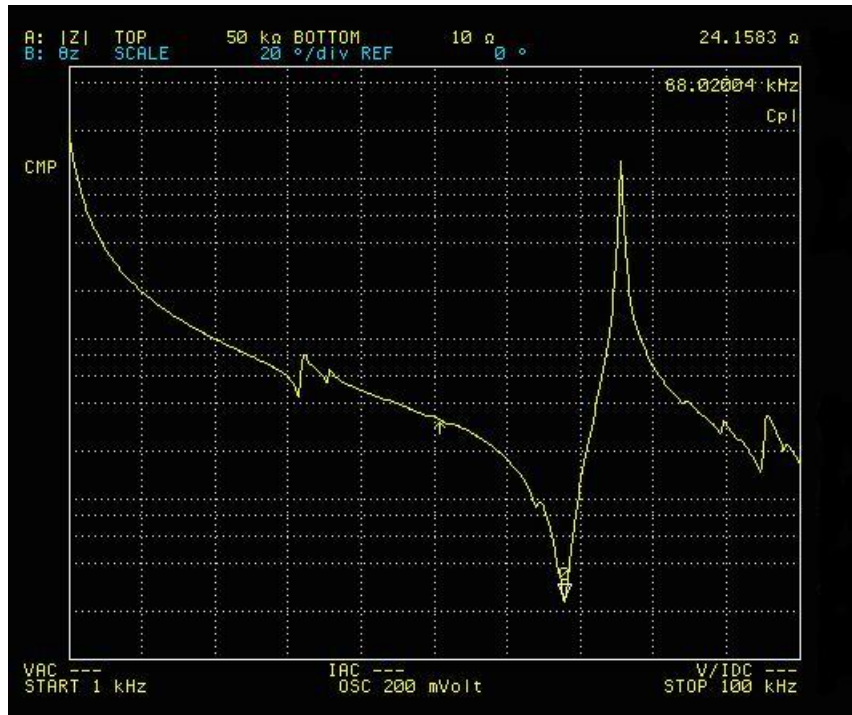|	Motor S	Motor M	Motor L
Stator Resonance Frequency f_{sr} (kHz)	63.5	69.5	69.5
Stator Anti-resonance f_{sa} (kHz)	69.1	77.6	75.6
Motor Resonance Frequency f_{mr} (kHz)	$\sim$61	$\sim$67	$\sim$60
Motor Capacitance C_m (nF)	5.390	7.612	9.107

Figure 3.11: Motor Impedance versus Exciting Frequency (Motor M)
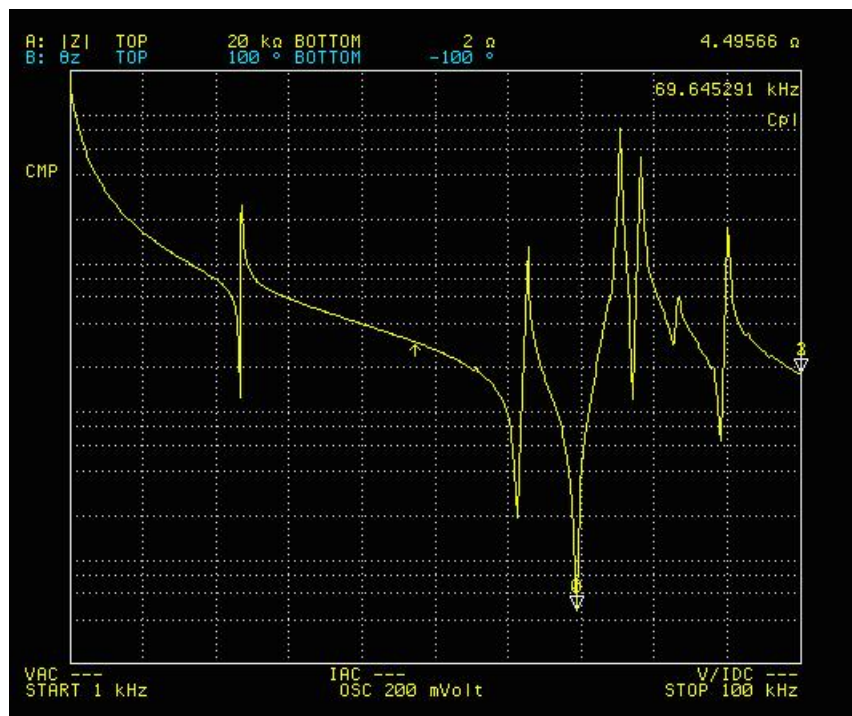

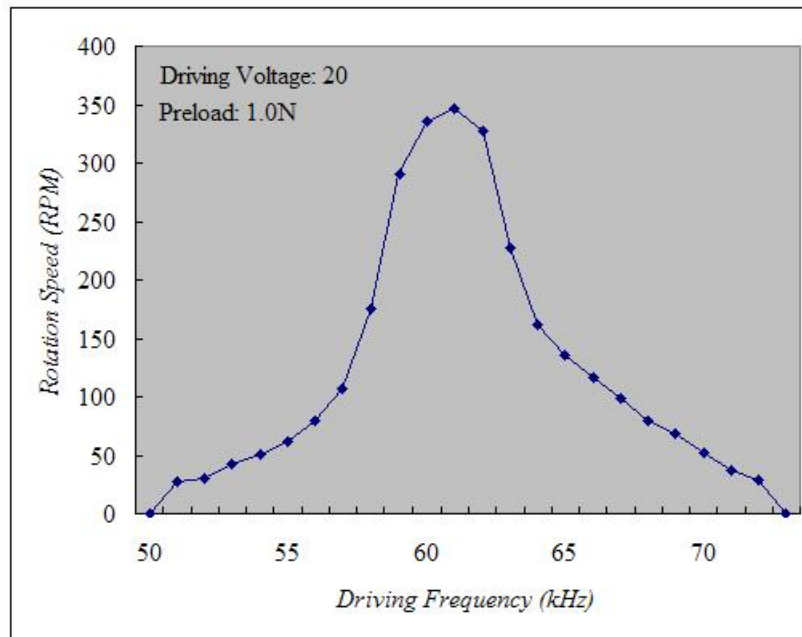Figure 3.12: Motor Impedance versus Exciting Frequency (Motor L)

Figure 3.13: Rotation Speed as a Function of Driving Frequency (Motor S)

3.4 Control System Implementation

3.4.1 Operation of Cylindrical USM

The motor operation requires four sinusoidal voltage signals with 90° phase difference being applied to electrodes A~D (Figure 3.8) respectively. These four voltage signals are generated by full-bridge inverters, which are combined and integrated into a driving circuit. In general, there are three possible control inputs for controlling the speed of the cylindrical motor—amplitude, frequency and phase difference of the four sinusoidal driving voltage signals. Frequency control system is not efficient because stator vibration is not at its maximum and unstable if it is not operated at resonance state. On the other hand, phase difference which is not 90° creates slippage in the stator-rotor interface and causes large speed ripples. Hence, voltage amplitude control provides the most effective means for speed control. A driving circuit based on amplitude control scheme has these three controllable parameters:

- *voltage control*: controls the amplitude of sinusoidal signals for variable speeds

- *phase control*: can switch between 90° and −90° phase difference to generate clock-

wise or anticlockwise rotations.

- *frequency control*: a means to adjust the frequency of signals, so that it matches the motor resonance frequency for optimal performance.
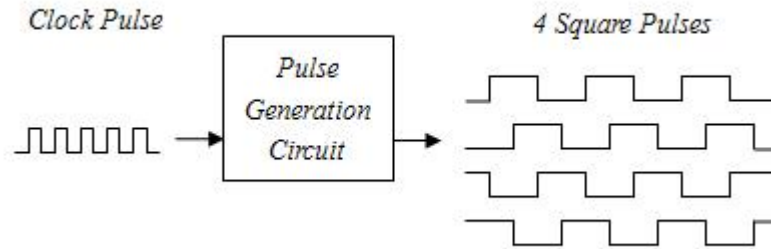
3.4.2 Driving Circuit Design

Similar driving system using two sinusoidal signals has been developed to operate cylindrical type ultrasonic motors [60]. To provide four sinusoidal signals that are 90° out of phase with adjustable amplitude, a driving circuit is proposed comprised of the following components (Figure 3.14):

1. **Pulse Generation Unit**: Firstly, four identical square pulses of same frequency but with 90° phase difference are generated through the pulse generation circuit. These pulse signals are responsible for switching the power MOSFETs in the inverter. This circuit essentially consists of Timer `NE555` and J-K Flip Flop `74LS73` ICs. A variable resistor is included to tune the frequency of Timer `NE555` clock pulse. The parent clock pulse is then passed through 2 J-K Flip Flops and creates four signals of different phases—making use of the toggle property of J-K Flip Flop when pulse changes from 0 to 1. Generated square pulses have frequency four times smaller than the original frequency (Figure 3.14(a)).

2. **Boost DC-DC Converter Circuit**: The amplitude of the output sinusoidal signals in an inverter is controlled by the input DC link voltage. A boost DC-DC converter is implemented to boost and control the amplitude of this DC voltage. This is necessary for remote motor operation when batteries are used. The circuit consists of inductor L, capacitor C, resistor R, diode and power MOSFET switch (Figure 3.14(b)). In a DC-DC converter, the output voltage amplitude can be varied by adjusting the duty cycle D of the switching signal, which is governed by the relation

$$\frac{V_{out}}{V_{in}} = \frac{D}{1 - D}.$$
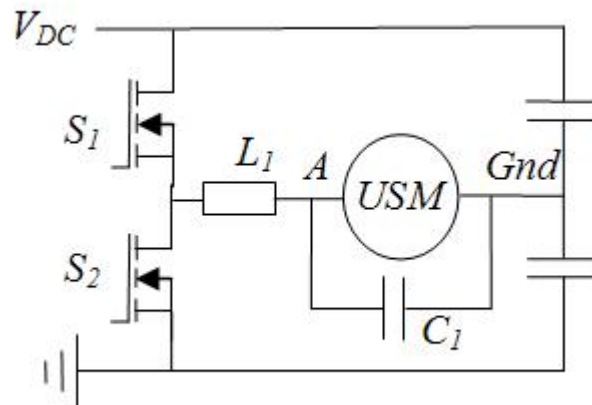
Control of the duty cycle D is achieved through Pulse-Width Modulation (PWM)

(a) Pulse Generation Circuit
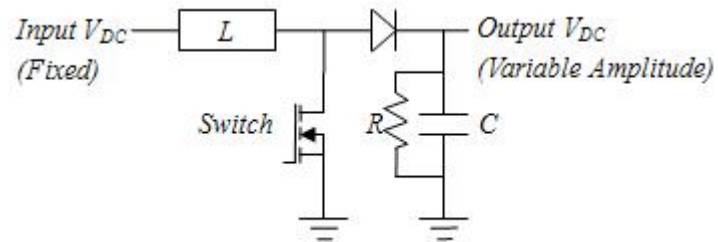
(b) Boost DC-DC Converter

(c) Series Resonance Inverter

Figure 3.14: Main Components in the Driving Circuit

of the switch gating signals, which can be manipulated real-time by control signals from the computer or microprocessor. A more detailed explanation of the working principle can be found in power electronics handbook [59]. One property of the boost DC-DC converter is that its output voltage cannot be reduced to zero. The minimum value of the output voltage is the same as input voltage amplitude. In cases where full-range output voltage control is required, a buck-boost converter can be considered [59].

3. **Series Resonance Inverters**: The variable DC link voltage generated by the DC-DC converter is fed into the series resonance inverter to generate adjustable sinusoidal signals for motor operation. The DC input V_{DC} is inverted by full-bridge inverters and later filtered by resonance LC circuit (Figure 3.14(c)). The frequency of the generated signals is dependent on switching frequency of the power MOSFETs (S_1 & S_2), controlled by square pulses from the pulse generation circuit. In order to obtain sinusoidal signals, inductors L_1 and capacitors C_1 are connected to the motor to form a resonant tank. Resonance frequency of this LC resonant tank, f_{ir} (including the motor capacitance C_m) is designed to be close to the switching frequency of power MOSFETs, which should be the same as the motor resonance frequency f_{mr}. Such setting can boost the amplitude of the output signals through resonance gain. The frequency f_{ir} can be estimated by

$$f_{ir} = \frac{1}{2\pi\sqrt{LC}} \tag{3.15}$$

where L is the inductance in the inverter (L_1 for electrode A) and C is the total capacitance, $C = C_1 + C_m$.

A schematic diagram of the driving circuit and control system can be described in Figure 3.15. Digital or analog signals ($u_1 \sim u_3$) are generated by the control unit (a computer or microprocessor) to control the driving circuit. PWM signal u_1 controls the duty cycle D of switching signal in the DC-DC converter, which is directly related to the amplitude of output sinusoidal signals. Control variable u_2 adjusts the frequency of the

clock pulse to match the output sinusoidal frequency with the motor resonance frequency. The direction of rotation is switched by u_3, which changes the phase difference of pulse signals from $90°$ to $-90°$ or vice versa. The main variable of the driving system is the amplitude of the output sinusoidal signal, which decides rotational speed and torque of the motor operation. Closed loop control can be achieved by feeding back the angular position θ of the cylindrical USM using an optical encoder.
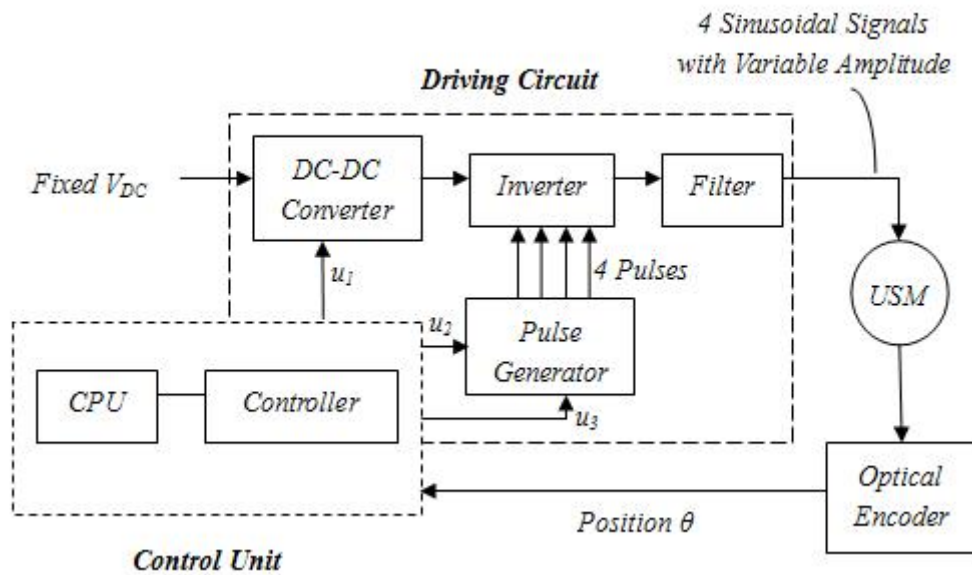

Figure 3.15: Schematic Diagram of Driving Circuit and Control System

3.4.3 Hardware Implementation

The complete driving system is shown in Figure 3.16. Power MOSFETs `IRF630` are used as switches in the inverter and DC-DC converter circuit. These MOSFETs are driven by `IR2110` IC chips, which are *high and low side MOSFET drivers*. Input voltage of the whole driving system is provided by a DC Power supply and is fixed at 10V. Duty cycle control of the DC-DC converter is provided by a PWM scheme control input, which can vary from 20% to 80%. Gating signals for the MOSFET switches are provided by the pulse generation unit. In the pulse generator, four pulses with $90°$ phase difference are generated by a timer `NE555` followed by two J-K Flip Flops `74LS73`.
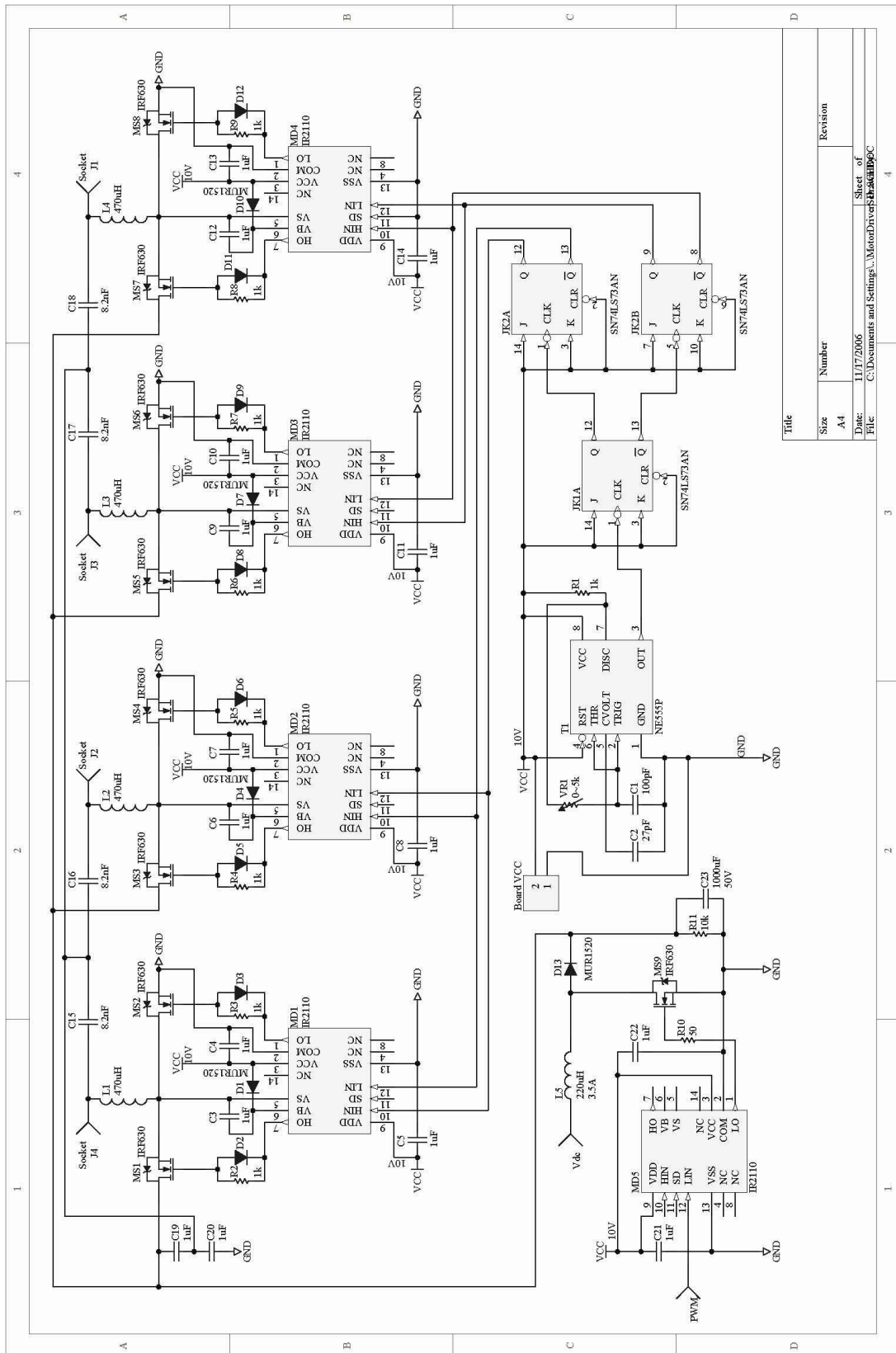
Figure 3.16: Schematics of Complete Driving System

Limitation of the Driving Circuit

The proposed driving circuit has succeeded in driving and controlling the motors at different speeds and directions. However, it has the following limitations:

- In current design, the amplitude of the sinusoidal signals cannot be reduced to zero since a boost DC-DC converter is used. If a full-range control is required, a buck-boost DC-DC converter can be considered.

- The amplitude of the sinusoidal signals is also constrained by the current limit of the driving circuit. The operating range is limited (lower than $100V_{pp}$) to avoid overheating of the electronic components and piezoelectric crystals. In cases where higher signal amplitude is recommended, components with better tolerance should be used in the driving system. The circuitry design could also be improved to reduce the current consumption during high amplitude operation.

- Since the motor is connected in series with the series resonance inverter, internal capacitance and inductance of the motor has a direct effect on the value of resonant tank. Because the inductors and capacitors used are of fixed values, any changes in the motor electrical properties during motor operation will not be compensated, and thus may distort the sinusoidal signals and affect the performance. Variable inductors and capacitors can be considered if more accurate adjustment is required.

3.5 Summary

The first section shows necessary power requirement in a humanoid hand to exert a finger force of 40N (Table 3.1). *Built-in-actuator* and *wire-driven* type actuation systems are also discussed and compared. As a result, an actuation system using direct-drive cylindrical ultrasonic motor is proposed due to its superior properties, especially its high power to weight ratio.

Custom made cylindrical type USMs are developed and fabricated in this research. Three USMs with different stator diameters (Motor S 10mm, Motor M 15mm and Motor

L 20mm) but same stator length (20mm) are fabricated for different joint requirements in the humanoid hand. Firstly, the operating principle and basic structure of a cylindrical USM are investigated. The dynamics of motor stator vibration is later analyzed using simple beam bending model and thin cylindrical shell model. Theoretical equations derived from the simple beam model are used to estimate motor rotational speed and torque. It is noted that the estimation accuracy is limited since stator dimensions are not within the derivation assumption. Features are added into the USM structural design (Figure 3.4~3.7) to improve its performance. For better output power, novel PZN-7%PT single crystal piezoelectric crystal is used as driving element. Driving frequencies of the three USMs, which are the same as motor resonance frequencies f_{mr}, are determined as 61, 67 and 60kHz respectively.

A driving system is proposed to operate the motor using four-channel sinusoidal signals with 90 degree phase difference. Operating frequency is the same as motor resonance frequency, and signal amplitude is adjustable to control the magnitude of motor speed. The circuit essentially consists of pulse generation unit, boost DC-DC converter and series resonance inverter. Motor control is achieved by monitoring the duty cycle D of switching signal in the DC-DC converter, which is proportional to the output signal amplitude.

Chapter 4

Design Evaluation

4.1 Actuation System Evaluation

4.1.1 Driving System Characteristic

The performance of a cylindrical USM driven by proposed driving circuit is investigated. Since a complete control unit is yet to be developed, an external Frequency Generator is used to generate control signals with PWM scheme to adjust the duty cycle D. The driving frequency is set according to Table 3.6 for each motor. Input voltage for the circuit is fixed at 10V, which is provided by a DC Power Supply.

The driving system is able to generate sinusoidal signals between $50V_{pp}$ to $100V_{pp}$ from a 10V DC supply, which corresponds to the duty cycle D of the switching signal from 20% to 80%. Duty cycle values at extreme ends would cause high power loss in the DC-DC converter and therefore are not used. High gain in amplitude of the output signals is also partly contributed by resonance gain in the series LC inverter.

During the motor operation, a few observations are made and discussed as follow:

- A small fluctuation is observed in the output voltage signals during the motor operation. This is mainly due to variations of load impedance (in this case, the connected motor) which is a function of friction contacts and preload force in the stator-rotor interface.

- The amplitude of the exciting signals is not only dependent on the duty cycle D, but also a function of preload force applied to the stator. It has been stated that resonance frequency of the motor is lowered when high preload force is applied. When the resonance frequency is shifted, resonance gain in the series LC inverter is affected and thus the output signal amplitude drops.

- The driving system does not have current monitoring capability to control the current passing through the motor load. This indicates that the motor operation runs the risk of overheating the piezoelectric crystals when high V_{pp} is applied for a long time.
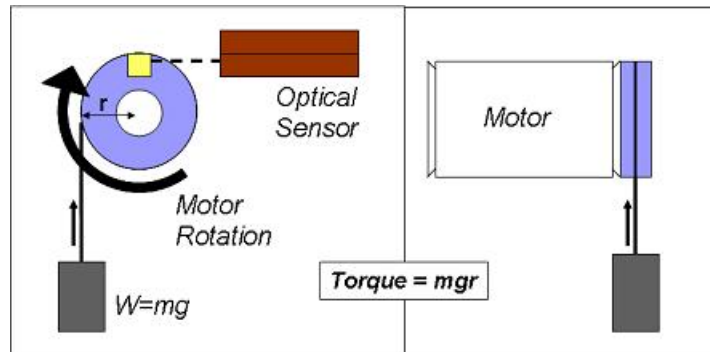
4.1.2 Experimental Motor Performance

Experimental Setup

The torque-speed curve of the cylindrical USM is determined by *weight lifting technique.* A simple experiment is set up as shown in Figure 4.1(a). Spindles (Figure 4.1(b)) are attached to the rotor by means of connection pins. Weights of different mass act as the load and the output torque τ can be calculated by $\tau = mgr$, where m is the weight mass and r is the radius of spindle. Rotational speed ω is measured using an optical sensor. Actual implementation is illustrated in Figure 4.1(c).
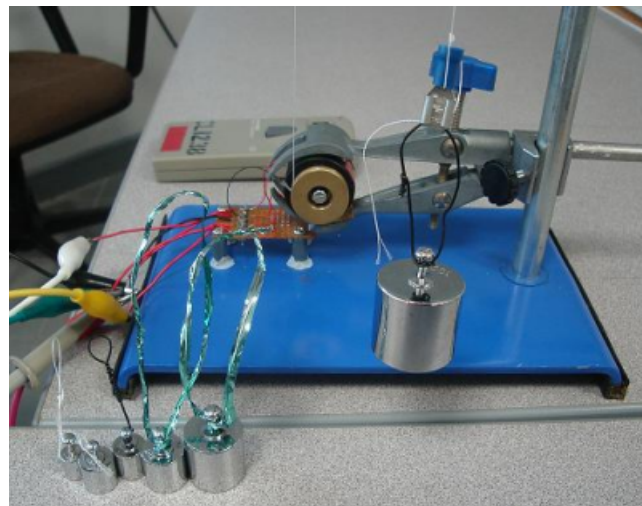
Torque-Speed Relation

Torque-speed relations of Motor S are summarized in Figure 4.2(a) and 4.2(b). Figure 4.2(a) demonstrates the relationship between motor speed and output torque when a preload force of 2N is applied while Figure 4.2(b) illustrates the relationship when a preload force of 5N is exerted. In both cases, the operating frequency is adjusted to be the same as the resonance frequency after the preload effect is considered. Duty cycle values are also selected such that amplitudes of the driving signal remain close. The no-load speeds for the two cases are 351 RPM and 316 RPM respectively. On the other hand, maximum output torques are 4.5mNm and 10mNm.

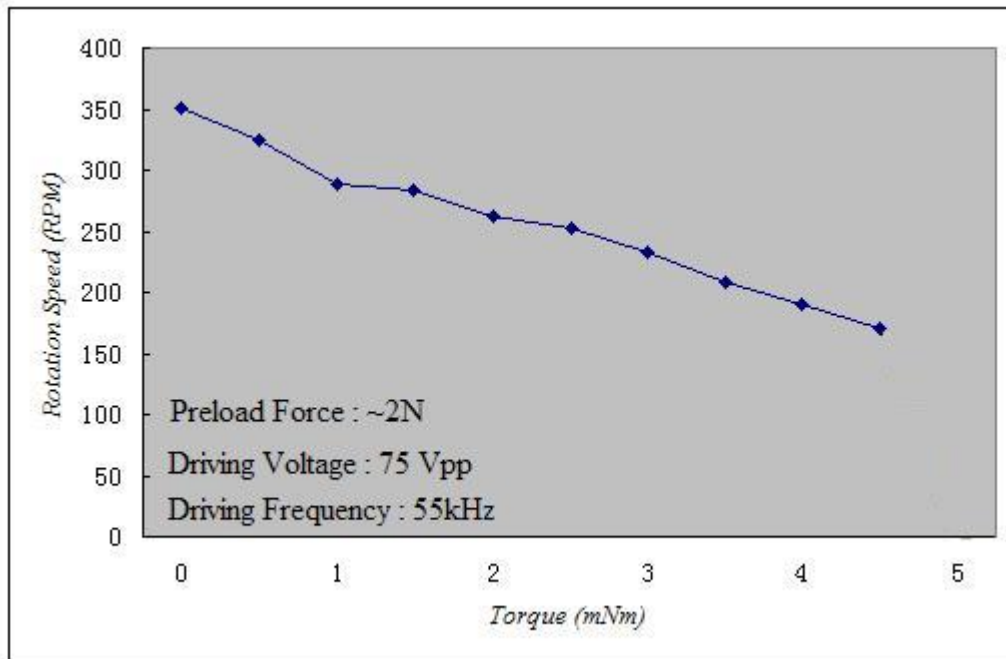(a) Schematics of Experiment Setup

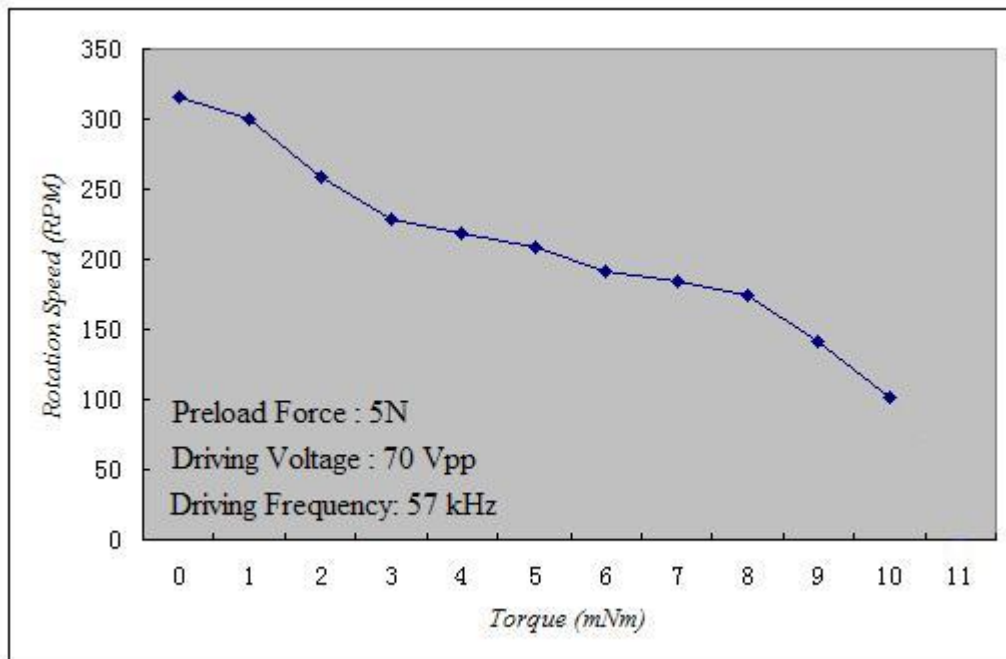

(b) Spindles for Motor Analysis

(c) Weight Lifting Experiment

Figure 4.1: A Motor Performance Test

(a) Torque-Speed Curve at Preload Force of 2N

(b) Torque-Speed Curve at Preload Force of 5N

Figure 4.2: Torque-Speed Relations of Motor S

The two graphs show that preload force determines the maximum torque that can be produced. A higher preload force increases the frictional force in between stator and rotor, and converts more vibration energy into motor output power. It is observed that the rotational speed drops sharply when applied load torque reaches the maximum value. The abrupt change in speed is caused by the design of weight lifting technique. Since the weight is not placed along the stator-rotor interface, extra moment is introduced and makes preload pressure on the surface uneven (Figure 4.3). When the weight mass increases, this effect becomes significant and causes motor failure. Other measurement techniques should be considered to investigate its high torque characteristics.
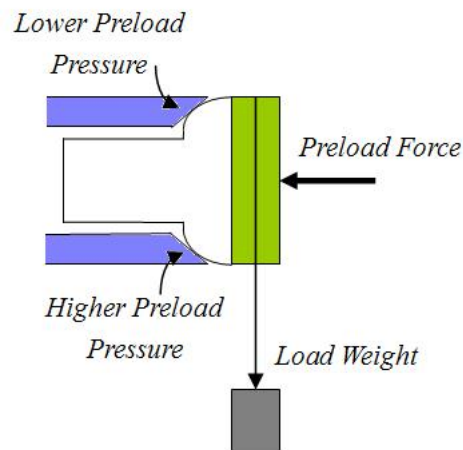

Figure 4.3: Effect of Weight Lifting on the Contact Interface

The motor performance can be theoretically improved by increasing the amplitude of applied voltage signals or the preload forces exerted on the rotors. As discussed above and shown in Figure 4.2, preload force applied has to be increased to increase the maximum motor torque. The relation between preload and maximum torque can be assumed to be linear. However, a motor under high preload force consumes more power, draws more current and creates more significant friction loss during motor operation. Such operating condition can easily overheat and depolarize the piezoelectric crystals. To overcome this problem, the motor design can be improved to reduce friction loss in the contact surface and minimize current consumption.

Comparison with Theoretical Values

The principle and estimation of theoretical speed and torque have been discussed in Section 3.2.3. In this section, these theoretical values are calculated and later compared with the experimental results. The maximum rotational speed and torque of a cylindrical USM can be estimated using equations (3.12) and (3.13).

For comparison purposes, the dimensions of Motor S, crystal properties and operating frequency are substituted into the equations (Actual values can be found in the previous sections). The quality factor is assumed to be **55** (PZN-PT) and the coefficient of friction is taken as **1.4** (for aluminum). As a result, the *Estimated Nominal Rotational Speed* is

$$\omega_R = 0.3748 V_{p-p} \text{RPM} \tag{4.1}$$

and *Estimated Maximum Torque* is

$$\tau_{max} = 7.583 \times 10^{-4} V_{p-p} \text{Nm} \tag{4.2}$$

which are directly proportional to the voltage amplitude V_{p-p}.

Substituting the operating voltage amplitude as $75V_{pp}$ (Same amplitude as the experimental values), the theoretical no-load speed and maximum torque are **28 RPM** and **56.9 mNm** respectively. It is obvious that the equation for no-load speed requires revision for more accurate estimation. On the other hand, theoretical maximum torque is assumed when the preload force is sufficiently high to prevent stator vibration. Therefore, this torque can be taken as the upper limit when preload force applied is further increased.

Output Power and Efficiency

Graphs of output power versus output torque are plotted and illustrated in Figure 4.4(a) and (b). The output power P_o is calculated using the equation $P_o = \tau \times \omega_R$. It can be seen that the maximum powers are 80mW and 145mW, occur at 4.5mNm and 8mNm respectively. Torque region around the maximum power defines the optimal operating

range of Motor S at these preload forces. Input power of the motor can also be estimated by $P_i = V_{rms}I_{rms}cos\psi$, where ψ is the input phase difference. In general, since the motor is a capacitive load, the phase lead ψ is close to $90°$ and can be assumed to be $70 \sim 80°$ (In this example, a phase lead of $75°$ is assumed). Through measurement, average input currents I_{rms} for each of the four electrodes connected to the motor are 18mA for 2N preload and 23mA for 5N preload. Maximum power efficiency η_{max} of Motor S is thus estimated as

$$\eta_{max} = \frac{P_{o,max}}{P_i} = \frac{80mW}{4(70V/\sqrt{2})(18mA)\cos 75°} = 8.65\%, \quad \text{(2N Preload)}$$

$$\eta_{max} = \frac{P_{o,max}}{P_i} = \frac{145mW}{4(75V/\sqrt{2})(23mA)\cos 75°} = 11.45\%, \quad \text{(5N Preload)}$$

The low power efficiencies indicate that the optimal performance of USM is not achieved. Further investigations are required on the motor parameters, driving system and operating conditions to improve the efficiency.

Analysis on Motor M and Motor L

Motor M experiences frequency mismatch problem when it is connected to the driving system. It is observed that the resonance frequency of Motor M (which has been determined as 67 kHz) is too high to be matched by resonance frequency f_{ir} of the series resonance inverter. As a consequence, the motor is not operating at its resonance frequency and thus shows undesired performance. In order to drive the motor at the designated frequency, a more effective inverter circuit will be required.

It is also found that the performance of Motor L is not satisfactory when it is excited at resonance frequency. The induced rotational speed and torque are comparatively weak and not suitable for the actuation system. The driving force of the motor, which is related to the magnitude of stator vibration, is not as large as expected, which is probably due to the short stator dimension. Further investigation on the motor dimensions will be required to improve the performance.
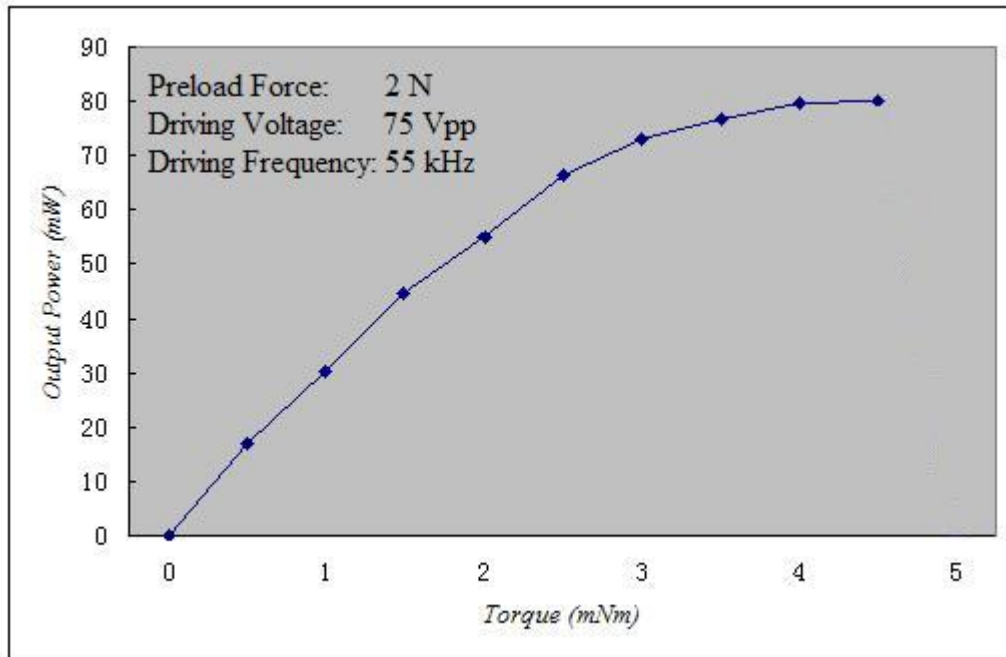
(a) Output Power vs Output Torque at Preload Force of 2N
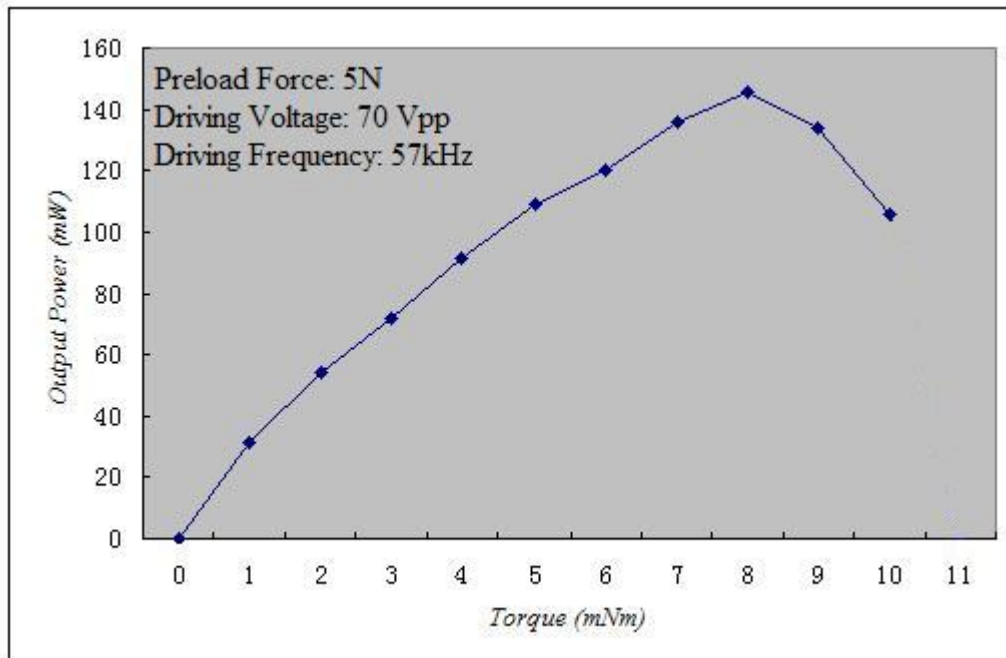
(b) Output Power vs Output Torque at Preload Force of 5N

Figure 4.4: Output Power of Motor S at Different Preload Forces

4.1.3 Comparison with Other Actuation Systems

The developed actuation system using cylindrical USM makes use of direct-drive approach and has a rather simple structure compared to other actuation systems. At a preload force of 5N, the cylindrical USM Motor S is capable of generating a maximum torque of 10mNm, which can be increased to 76mNm at $100V_{pp}$ when sufficient preload force is applied (estimated using Equation 3.13). Compared to conventional flat USM motor used in humanoid hand (diameter 30mm and $\tau_{max} = 0.1Nm$) [12], cylindrical USM will be a better choice due to its structural advantage and higher torque to size ratio.

In comparison with direct-drive electric motor, the cylindrical USM which is without a gear box saves more space and in addition, is able to provide holding torque passively using static friction. In terms of power output, it is shown that USM has the potential to be further improved to match with its electric counterpart (Table 4.1), although currently the motor operation is limited by the driving circuit design and heat loss problem. As a conclusion, the cylindrical USM actuation system is a novel and feasible driving force for humanoid hand design.

Table 4.1: Comparison between Cylindrical USM and Electric Motor

Parameters	Motor S		Electric Motor*
	Reported Value	Attainable Limit	
Dimension	$\varnothing 10 \times 22$		$\varnothing 13 \times 24.5$
Voltage	$70V_{pp}$	Up to $500V_{pp}$	4.8V
No Load Speed	315RPM	-	6980RPM
Stall Torque	10mNm	$0.7583 \times V_{pp}$	1.77mNm
Power Rating	145mW	-	750mW
Efficiency η_{max}	11.45%	-	66%

*Specification of High Torque MAXON RE-Max 10 DC Servomotor

4.2 Kinematic Design Analysis

A finger prototype is physically constructed to verify the implementation of cylindrical USM actuation system. The prototype, includes the palm and two segments of index finger, is fabricated from aluminum according to the dimensions in Appendix C. Complete

assembly of the finger prototype (including motors) is illustrated in Figure 4.5. Simple and clean installation of a cylindrical USM is observed at the two joints, where no extra pulleys, tendons or any other mechanisms are required for the driving system. Only four driving electrode wires (red wire) and common wire (black wire) of the motor are extended and connected to the driving circuit, which will be placed in the palm. It is clear that the use of direct-drive cylindrical USMs has effectively reduced the weight of whole humanoid hand system and frees much space for other uses. For instance, motor encoders and touch sensors can be installed with more flexibility.

Minor modifications and corrections have been performed to the kinematic design, to account for glitches found during the finger prototype assembly. For instance, location of bolts and nuts is verified so that finger motions are not obstructed. Resulting finger joint output torque is rather low, mainly due to the heavy mass of prototype material. For example, the distant finger link alone weighs 73 grams, and reduces active torque of the distant joint by $73g \times 3cm = 22$mNm. The weight of the finger prototype can be reduced by fabricating it using lighter material, such as hard plastics.

4.3 Summary

This chapter concludes the experimental results of USM actuation system. The driving system is able to generate sinusoidal signals between $50V_{pp}$ to $100V_{pp}$ from a 10V DC supply, corresponding to the duty cycle D of switching signal from 20% to 80%. Output signal amplitude has a short operating range to prevent high heat loss at high amplitude operation, which could damage the piezoelectric crystals.

Torque-speed relations of Motor S at different preload forces are summarized in Figure 4.2(a) and 4.2(b). No-load speeds for the two cases are 351 RPM and 316 RPM respectively. Maximum torques achieved are 4.5mNm and 10mNm. It is found that higher preload force can increase the motor performance. Theoretical maximum torque can be reached when the preload force is sufficiently high to prevent stator vibration. Maximum output power and efficiencies are also calculated by assuming the input phase lead at $75°$. From the two experiments, maximum power of 80mW and 145mW, occur

(a) Fully Open Position
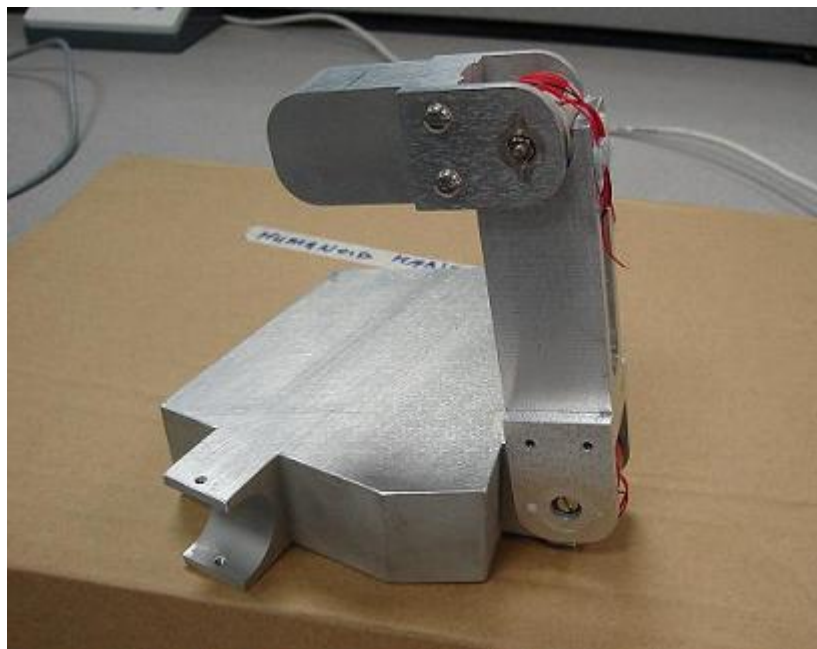
(b) Fully Close Position

Figure 4.5: Finger Prototype with Motors Attached

at 4.5mNm and 8mNm respectively. The maximum power efficiencies are estimated as 8.65% (2N Preload) and 11.45% (5N Preload).

Operations of Motor M and Motor L are found not effective due to frequency mismatch problem and short stator length. The design of inverter circuit and motor dimension should be reviewed to improve the motor performance. Compared with other humanoid hand actuation systems, the feasibility of single crystal USM is verified due to its structural advantage, high power to weight ratio, passive holding force, etc. Actual cylindrical USM actuation system is implemented in a finger prototype. It is shown that the system implementation is light and compact, which frees a lot space for other uses, such as sensor installations.

Chapter 5

Conclusion

5.1 Summary

In this thesis, the kinematic design of a task specific humanoid hand and an actuation system using single crystal cylindrical USM are presented. The humanoid hand is specifically designed for prosthesis use and simplified based on a limited functionality requirement. At the same time, a novel cylindrical USM driven actuation system is proposed and developed.

A task specific design methodology is adopted to develop a humanoid hand. Based on the necessary requirements of prosthesis, the specified hand functionality is represented as six basic grasps — Cylindrical, Spherical, Lateral, Palmar, Pinch and Hook Grasps. A comprehensive set of grasp functions and contact point systems is then defined and used as design tool. As a result, a seven DOFs, three fingers humanoid hand prototype is designed and refined. The kinematic design is verified through grasp simulations.

Then, an actuation system for humanoid hand using cylindrical USM is developed and constructed. Cylindrical USM is chosen to be the actuator and its operating principle is discussed. Estimated motor properties are obtained through modeling techniques. Following that, three different sizes of cylindrical USMs are specially designed and assembled to drive the joints of humanoid hand. Fabrications of these cylindrical USMs make use of the novel PZN-7%PT piezoelectric single crystal as their driving element. A

driving circuit for cylindrical USM that includes full-bridge inverters and DC-DC converter is also developed. A duty cycle control scheme is used to vary the amplitude of voltage signals and hence control the motor speed and output torque, while the direction of rotation is switched by changing the phase difference of the driving signals.

Finally, a finger prototype is fabricated and the implementation using cylindrical USM is investigated. It is observed that direct-drive cylindrical USMs occupy less space, effectively reducing the load and simplifying the actuation system. The motor performance is measured through weight-lifting experiment and is compared with other actuation systems. Experimental results verify the potential of cylindrical USM in humanoid hand application. Observations during motor operation are also made and discussed.

5.2   Proposals for Future Work

The work presented in this thesis initiates a new perspective in humanoid hand design and at the same time has laid down much room for improvements. The author would like to make the following proposals:

- Task specific technique requires a comprehensive set of grasp and manipulation definitions. The six basic grasp definitions have been demonstrated in this thesis but the list is not limited to these. More grasp definitions can be obtained to design humanoid hand with more sophisticated functions.

- Current hand design is based on an equal preference to all grasps. For the development of hands with special purposes, a kinematic design optimization procedure that is able to set preference to a particular grasp can be investigated.

- Two modeling methods have been investigated to estimate the driving frequency and motor performance but the results are not accurate. The effects of preload force and friction model at stator-rotor interface, which can affect the resonance frequency, are not included in the modeling. A more complete modeling technique can be used to obtain better estimation.

- Efforts can be made to miniaturize both the cylindrical USM and the driving circuit in order to reduce the overall size of the humanoid hand actuation system.

- It is found that the series resonance inverter is not suitable to drive the motor with high resonance frequency (such as Motor M) due to frequency mismatch problem. Other ways of generating exciting signals can also be investigated, such as using AC power supply.

- Experimental motor performance has been measured using weight-lifting technique. It is observed that the resolution and precision of this technique are low. It also causes extra moment in the rotor and creates uneven preload pressures. Therefore, it is necessary to use a better mean for torque and speed measurements in the future work.

Appendix A

Timoshenko's Equation

A.1 Derivation of Timoshenko's Equation

A.1.1 Transverse Vibration of Prismatic Beam

Let us now consider the transverse vibration of a prismatic beam in $x - y$ plane (Figure A.1). When the beam is vibrating transversely, the dynamic force equilibrium in y-direction is

$$V - V - \frac{\partial V}{\partial x} dx - \rho A dx \frac{\partial^2 v}{\partial t^2} = 0 \tag{A.1}$$

and the moment equilibrium equation

$$-V dx + \frac{\partial M}{\partial x} dx \approx 0 \tag{A.2}$$

From elementary flexural theory, we have

$$M = EI \frac{\partial^2 v}{\partial x^2} \tag{A.3}$$

EI — flexural rigidity, where
E — Young's Modulus
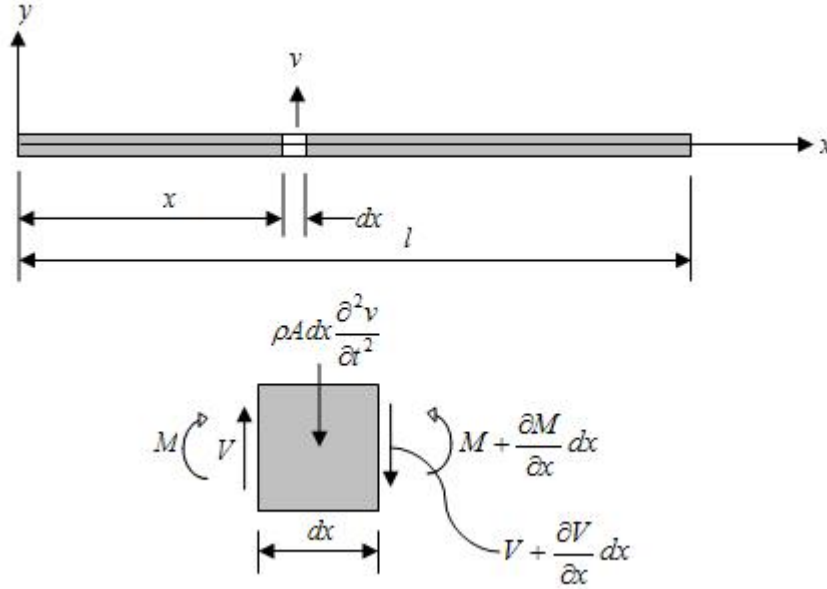I — second moment of inertia

Figure A.1: Schematic Diagram of A Prismatic Beam

ν — transverse displacement of a typical beam segment
V — shearing force
M — bending moment
ρ — density
A — cross section area
l — total length of the beam

Using the expressions in A.1 $\sim$ A.3, we obtain

$$EI\frac{\partial^4 v}{\partial x^4}dx = -\rho A dx \frac{\partial^2 v}{\partial t^2} \qquad (A.4)$$

which is the general equation for transverse free vibration of a beam, assuming EI does not vary with x. When a beam vibrates transversely in one of its natural modes, the deflection at any location varies harmonically with time, as follow:

$$v = X(A\cos\omega t + B\sin\omega t) \qquad (A.5)$$

where X is the beam mode shape and ω is the vibration frequency.

Let $a = \sqrt{\frac{EI}{\rho A}}$, equation A.4 becomes

$$\frac{\partial^4 v}{\partial x^4} = -\frac{1}{a^2}\frac{\partial^2 v}{\partial t^2} \tag{A.6}$$

Substituting eq.A.5 into eq.A.6 results in

$$\frac{d^4 X}{dx^4} - \frac{\omega^2}{a^2}X = 0 \tag{A.7}$$

To solve this 4th order ordinary differential equation, we introduce k, and $k^4 = \frac{\omega^2}{a^2}$,

$$\frac{d^4 X}{dx^4} - k^4 X = 0 \tag{A.8}$$

General solution for X is

$$X = C_1 \sin kx + C_2 \cos kx + C_3 \sinh kx + C_4 \cosh kx \tag{A.9}$$

This expression represents a typical normal function for transverse vibration of a prismatic beam. The constants C1~C4 in eq.A.9 can be determined by boundary conditions at the ends of beam.

A.1.2   Beam with Free Ends

At free ends, both the bending moment M and shearing force V vanish to zero. We have the following boundary conditions:

$$\left(\frac{d^2 X}{dx^2}\right)_{x=0} = 0, \left(\frac{d^3 X}{dx^3}\right)_{x=0} = 0, \left(\frac{d^2 X}{dx^2}\right)_{x=l} = 0, \left(\frac{d^3 X}{dx^3}\right)_{x=l} = 0.$$

Substituting eq.A.9 into the boundary conditions, we would obtain

$$
\begin{aligned}
&C_2 = C_4 = 0 \\
&C_1(-\cos kl + \cosh kl) + C_3(-\sin kl + \sinh kl) = 0 \\
&C_1(\sin kl + \sinh kl) + C_3(-\cos kl + \cosh kl) = 0 \\
&\cos kl \cosh kl = 1
\end{aligned}
\tag{A.10}
$$

The solutions of kl for the last equation in eq.A.10 can be approximated as

$$
k_i l \approx (i + \frac{1}{2})\pi, i = 0, 1, 2, \ldots
\qquad
\begin{aligned}
&k_0 l = 0 \\
&k_1 l = 4.730 \\
&k_2 l = 7.853 \ldots \ldots
\end{aligned}
\tag{A.11}
$$

and C_1 and C_3 can be found by substituting the value of kl back into eq.A.9. The first 3 modes of vibration of the beam are
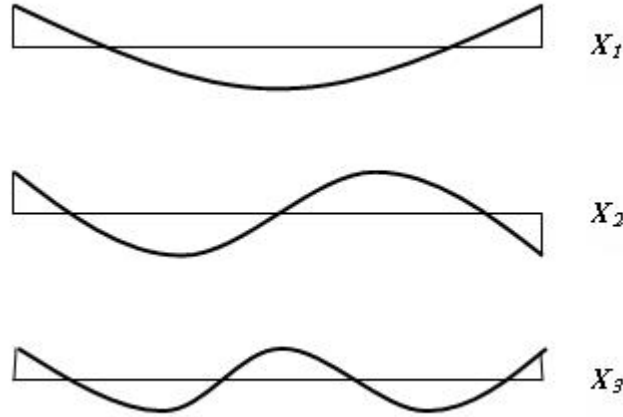

Figure A.2: First 3 Modes of Vibration of a Prismatic Beam

A.1.3 Effects of Rotary Inertia and Shearing Deformation

In previous discussions, we have assumed that the cross-sectional dimensions of the beam were small with respect to its length. Corrections to the theory will now be given for the purpose of taking into account the effects of cross-sectional dimensions on the frequencies.

Vibration of a typical beam element involves translational and rotational motions. The angle of rotation θ is equal to the slope of deflection curve $\frac{\partial v}{\partial x}$. Hence, *angular velocity* ω and *angular acceleration* α will be given by

$$\omega = \frac{\partial^2 v}{\partial x \partial t} \quad \text{and} \quad \alpha = \frac{\partial^3 v}{\partial x \partial t^2} \quad \text{respectively.}$$

Angular momentum M_ω of the element about an axis through its centre of mass and perpendicular to xy plane will be

$$M_\omega = I_m \alpha = -\rho I \frac{\partial^3 v}{\partial x \partial t^2} dx \tag{A.12}$$

where I_m is the mass moment of inertia. Including this angular momentum into the moment equilibrium eq.A.2,

$$-V dx + \frac{\partial M}{\partial x} dx - \rho I \frac{\partial^3 v}{\partial x \partial t^2} dx = 0 \tag{A.13}$$

and combines with eq.A.1 and A.3, we have

$$EI \frac{\partial^4 v}{\partial x^4} dx = -\rho A dx \frac{\partial^2 v}{\partial t^2} + \rho I \frac{\partial^4 v}{\partial x^2 \partial t^2} dx \tag{A.14}$$

This is the vibration differential equation, in which the second term on the right side represents the *effect of rotary inertia*. A more accurate differential equation is obtained where deflection due to shear is taken into account.

Let ψ denote slope of deflection curve when shearing force is neglected, and

$\quad$ β denote angle of shear at the neutral axis in same cross-section.

$$\frac{dv}{dx} = \psi + \beta \tag{A.15}$$

From elementary flexure theory, *bending moment M* and *shearing force V* are:

$$M = EI \frac{\partial^2 \psi}{\partial x^2}, \tag{A.16}$$

$$V = -\kappa \beta AG = -\kappa \left(\frac{dv}{dx} - \psi \right) AG \qquad (A.17)$$

κ — numerical factor depending on the shape of cross-section
A — cross-sectional area
G — shear modulus of elasticity

and the equation A.13 can also be written as

$$-V dx + \frac{\partial M}{\partial x} dx - \rho I \frac{\partial^2 \psi}{\partial t^2} dx = 0 \qquad (A.18)$$

Substituting eq.A.16 and A.17 into A.18, we obtain

$$EI \frac{\partial^2 \psi}{\partial x^2} + \kappa \left(\frac{dv}{dx} - \psi \right) AG - \rho I \frac{\partial^2 \psi}{\partial t^2} = 0 \qquad (A.19)$$

On the other hand, combining eq.A.1 and A.17,

$$\kappa \left(\frac{\partial^2 v}{\partial x^2} - \frac{\partial \psi}{\partial x} \right) G - \rho \frac{\partial^2 v}{\partial t^2} = 0 \qquad (A.20)$$

Eliminating ψ from eq.A.19 and A.20, we obtain the complete differential equation for transverse vibrations of prismatic beam, the **Timoshenko's Equation**,

$$EI \frac{\partial^4 v}{\partial x^4} + \rho A \frac{\partial^2 v}{\partial t^2} - \rho I \left(1 + \frac{E}{\kappa G} \right) \frac{\partial^4 v}{\partial x^2 \partial t^2} + \frac{\rho^2 I}{\kappa G} \frac{\partial^4 v}{\partial t^4} = 0 \qquad (A.21)$$

A.2 Resonance Frequencies of Free Ends Beam

The general equation of deflection v_i for a beam with 2 free ends can be written as

$$v_i = \left(\sin \frac{(i + 1/2)\pi x}{l} \right) (A_i \cos \omega_i t + B_i \sin \omega_i t), i = 0, 1, 2, \ldots \qquad (A.22)$$

where i denotes fundamental or higher natural modes. Neglecting last term in Timoshenko's Equation (which is small compares to other terms) and uses binomial expansion,

the resonance frequencies of natural modes are derived as

$$\omega_i = a\frac{(i+1/2)^2\pi^2}{l^2}\left[1 - \frac{I}{2A}\frac{(i+1/2)^2\pi^2}{l^2}\left(1 + \frac{E}{\kappa G}\right)\right].\qquad\text{(A.23)}$$

Appendix B

Cylindrical Shell Dynamics

Discussion on the dynamics here is limited to *thin circular cylindrical shell*, which is the general shape of USM stator. This fundamental model does not include the effects of initial stress, anisotropy, variable thickness, shear deformation, rotary inertia and other minor effects. In general, the standard or classical theories of thin shells are governed by 8th order systems of differential equations, which take many forms depending upon the assumptions made.
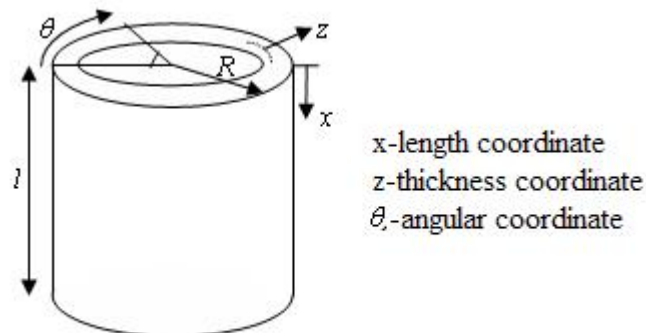

Figure B.1: Coordinate System of A Circular Cylindrical Shell

B.1 Fundamental Coordinate System

Shell coordinates x, θ and z are defined as the axial, circumferential and radial axes as shown in Figure B.1. The origin of z coordinate rests on the *middle surface*, which is

93

a layer lies in the middle of outer and inner shell surfaces. For derivation purpose, a dimensionless variable s is introduced to replace x coordinate where $s = \frac{x}{R}$, and R is the cylindrical radius.
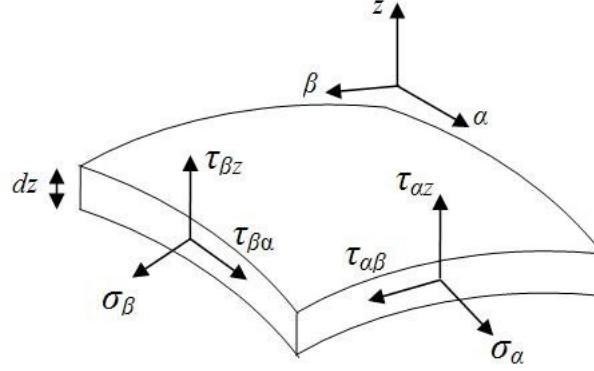

Figure B.2: A Fundamental Shell Element and Its Principal Stresses

B.2 Strain-Displacement Equations

Consider a fundamental shell element which is a differential element bounded by 2 surfaces dz apart at a distance z from the *middle surface*, with 4 side surfaces normal to the middle surface along the line constant α_o and constant β_o (Figure B.2). Coordinates α and β are generalized curvilinear axes of the shell surface. σ and τ denotes the normal and shear stresses in their corresponding directions.

In classic theory of small displacements of thin shells, the following assumptions were made, which is also called *Love's First Approximation*:

1. Thickness of the shell h is small compared with the other dimensions ($R/h \geq 10$).

2. Strains and displacements are sufficiently small so that higher order terms in strain-displacement equations can be neglected.

3. Transverse normal stress σ_z is small compared with other normal stresses and can be neglected ($\sigma_z \approx 0$).

4. Normals to the undeformed middle surface remain straight and normal to the deformed middle surface and suffer no extension ($\gamma_{\alpha z} = \gamma_{\beta z} = e_z = 0$). This is also known as *Kirchhoff's Hypothesis*.

Generalized strain-displacement equations for a thin shell were derived based on 3-dimensional Theory of Elasticity and expressed as

$$
\begin{aligned}
e_i &= \frac{\partial}{\partial \alpha_i}\left(\frac{U_i}{\sqrt{g_i}}\right) + \frac{1}{2g_i}\sum_{k=1}^{3}\frac{\partial g_i}{\partial \alpha_k}\frac{U_k}{\sqrt{g_k}}, \qquad i = 1,2,3 \\
\gamma_{ij} &= \frac{1}{\sqrt{g_i g_j}}\left[g_i\frac{\partial}{\partial \alpha_j}\left(\frac{U_i}{\sqrt{g_i}}\right) + g_j\frac{\partial}{\partial \alpha_i}\left(\frac{U_j}{\sqrt{g_j}}\right)\right], \qquad i \neq j
\end{aligned}
\tag{B.1}
$$

where e_i and γ_{ij} are normal and shear strains of the shell element. α_i in these equations represents the 3 shell coordinates (α, β and z) and U_i are displacement components of the 3 shell coordinates (U, V and W). The term g_i is defined as

$$
g_1 = A\left(1 + \frac{z}{R_\alpha}\right)^2, \qquad g_2 = B\left(1 + \frac{z}{R_\beta}\right)^2, \qquad g_3 = 1
$$

where A, B are coordinate constants and R_α, R_β are radii of curvature of the coordinates. According to *Kirchhoff's Hypothesis*, the 3 displacements can be rewritten as:

$$
\begin{aligned}
U(\alpha, \beta, z) &= u(\alpha, \beta) + z\theta_\alpha \\
V(\alpha, \beta, z) &= v(\alpha, \beta) + z\theta_\beta \\
W(\alpha, \beta, z) &= w(\alpha, \beta)
\end{aligned}
\tag{B.2}
$$

and u, v, w are the displacements of *middle surface* and $\theta_\alpha, \theta_\beta$ are rotations of the normal to the *middle surface* during deformation, i.e.

$$
\theta_\alpha = \frac{\partial U}{\partial z}, \qquad \theta_\beta = \frac{\partial V}{\partial z}.
$$

From the assumption $\gamma_{\alpha z} = \gamma_{\beta z} = 0$, it is derived that

$$
\begin{aligned}
\theta_\alpha &= \frac{u}{R_\alpha} - \frac{1}{A}\frac{\partial w}{\partial \alpha} \\
\theta_\beta &= \frac{v}{R_\beta} - \frac{1}{B}\frac{\partial w}{\partial \beta}
\end{aligned}
\tag{B.3}
$$

Substituting eq.B.2 into eq.B.1 yields

$$
\begin{aligned}
e_\alpha &= \tfrac{1}{1+z/R_\alpha}(\epsilon_\alpha + z\kappa_\alpha) \\
e_\beta &= \tfrac{1}{1+z/R_\beta}(\epsilon_\beta + z\kappa_\beta) \\
\gamma_{\alpha\beta} &= \tfrac{1}{(1+z/R_\alpha)(1+z/R_\beta)} \left[\epsilon_{\alpha\beta}\left(1 - \tfrac{z^2}{R_\alpha R_\beta}\right) + z\zeta\left(1 + \tfrac{z}{2R_\alpha} + \tfrac{z}{2R_\beta}\right) \right]
\end{aligned}
\tag{B.4}
$$

where $\epsilon_\alpha, \epsilon_\beta$ and $\epsilon_{\alpha\beta}$ are normal & shear strains in the *middle surface* due to stretching

$$
\begin{aligned}
\epsilon_\alpha &= \tfrac{1}{A}\tfrac{\partial u}{\partial \alpha} + \tfrac{v}{AB}\tfrac{\partial A}{\partial \beta} + \tfrac{w}{R_\alpha} \\
\epsilon_\beta &= \tfrac{u}{AB}\tfrac{\partial B}{\partial \alpha} + \tfrac{1}{B}\tfrac{\partial v}{\partial \beta} + \tfrac{w}{R_\beta} \\
\epsilon_{\alpha\beta} &= \tfrac{A}{B}\tfrac{\partial}{\partial \beta}\left(\tfrac{u}{A}\right) + \tfrac{B}{A}\tfrac{\partial}{\partial \alpha}\left(\tfrac{v}{B}\right)
\end{aligned}
\tag{B.5}
$$

and κ_α, κ_β are *midsurface* changes in curvature and ζ is the *midsurface* twist due to bending

$$
\begin{aligned}
\kappa_\alpha &= \tfrac{1}{A}\tfrac{\partial \theta_\alpha}{\partial \alpha} + \tfrac{\theta_\beta}{AB}\tfrac{\partial A}{\partial \beta} \\
\kappa_\beta &= \tfrac{\theta_\alpha}{AB}\tfrac{\partial B}{\partial \alpha} + \tfrac{1}{B}\tfrac{\partial \theta_\beta}{\partial \beta} \\
\zeta &= \tfrac{A}{B}\tfrac{\partial}{\partial \beta}\left(\tfrac{\theta_\alpha}{A}\right) + \tfrac{B}{A}\tfrac{\partial}{\partial \alpha}\left(\tfrac{\theta_\beta}{B}\right) + \tfrac{1}{R_\alpha}\left(\tfrac{1}{B}\tfrac{\partial u}{\partial \beta} - \tfrac{v}{AB}\tfrac{\partial B}{\partial \alpha}\right) + \tfrac{1}{R_\beta}\left(\tfrac{1}{A}\tfrac{\partial v}{\partial \alpha} - \tfrac{u}{AB}\tfrac{\partial A}{\partial \beta}\right)
\end{aligned}
\tag{B.6}
$$

For a circular cylindrical shell, the 2 generalized curvilinear axes α, β become s, θ and

$$
A = R, \qquad R_\alpha = \infty, \qquad B = R, \quad \text{and} \quad R_\beta = R.
$$

Using the above identities, expressions in eq.B.4, B.5 and B.6 can be simplified as

$$
\begin{aligned}
e_s &= \epsilon_s + z\kappa_s \\
e_\theta &= \tfrac{1}{1+z/R}\left(\epsilon_\theta + z\kappa_\theta\right) \\
\gamma_{s\theta} &= \tfrac{1}{1+z/R}\left[\epsilon_{s\theta} + z\zeta\left(1+\tfrac{z}{2R}\right)\right] \\
\epsilon_s &= \tfrac{1}{R}\tfrac{\partial u}{\partial s} \\
\epsilon_\theta &= \tfrac{1}{R}\tfrac{\partial v}{\partial \theta} + \tfrac{w}{R} \\
\epsilon_{s\theta} &= \tfrac{1}{R}\tfrac{\partial u}{\partial \theta} + \tfrac{1}{R}\tfrac{\partial v}{\partial s} \\
\kappa_s &= -\tfrac{1}{R^2}\tfrac{\partial^2 w}{\partial s^2} \\
\kappa_\theta &= \tfrac{1}{R^2}\left(\tfrac{\partial v}{\partial \theta} - \tfrac{\partial^2 w}{\partial \theta^2}\right) \\
\zeta &= \tfrac{2}{R^2}\left(\tfrac{\partial v}{\partial s} - \tfrac{\partial^2 w}{\partial \theta \partial s}\right)
\end{aligned}
\tag{B.7}
$$

B.3 Stress-Strain Relations

Assumes that the shell is made from materials which are linearly elastic and isotropic, Hooke's Law can then be applied to establish the stress-strain equations. Based on the assumptions $\sigma_z \approx 0$ and $\gamma_{sz} = \gamma_{\theta z} = e_z = 0$, the derivation of stress-strain equations is
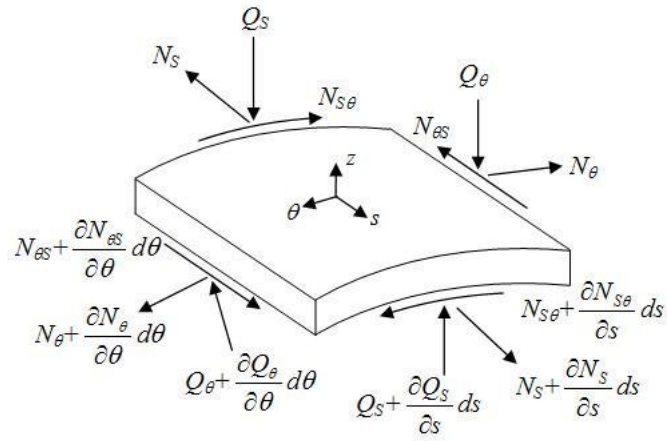
$$
\begin{aligned}
\sigma_s &= \tfrac{E}{1-\nu^2}\left(e_s + \nu e_\theta\right) \\
\sigma_\theta &= \tfrac{E}{1-\nu^2}\left(e_\theta + \nu e_s\right) \\
\tau_{s\theta} &= \tfrac{E}{2(1+\nu)}\gamma_{s\theta}
\end{aligned}
\tag{B.8}
$$
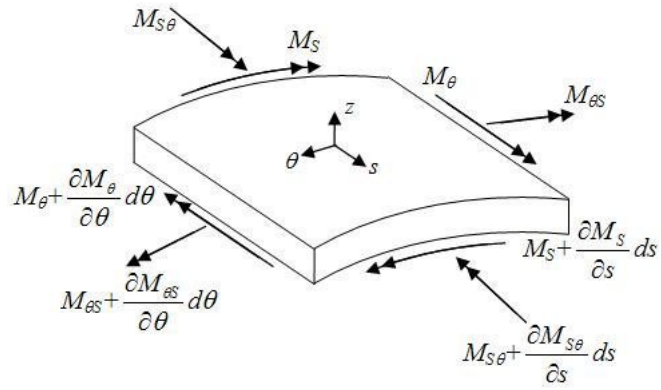
B.4 Force and Moment Resultants

Force resultants and *moment resultants* (Figure B.3) are obtained by integrating stresses over the shell thickness dz. They have dimensions of force per unit length and moment per unit length. Total thickness of shell is defined as h.

The distributed forces and moments are related to the stresses via

$$
\left\{
\begin{array}{c}
N_s \\
N_{s\theta} \\
Q_s
\end{array}
\right\}
=
\int_{-\frac{h}{2}}^{\frac{h}{2}}
\left\{
\begin{array}{c}
\sigma_s \\
\tau_{s\theta} \\
\tau_{sz}
\end{array}
\right\}
\left(1 + \frac{z}{R}\right) dz
\tag{B.9}
$$

(a) Force Resultants

(b) Moment Resultants

Figure B.3: Stress Resultants on a Shell Element

$$\left\{ \begin{array}{c} N_\theta \\ N_{\theta s} \\ Q_\theta \end{array} \right\} = \int_{-\frac{h}{2}}^{\frac{h}{2}} \left\{ \begin{array}{c} \sigma_\theta \\ \tau_{\theta s} \\ \tau_{\theta z} \end{array} \right\} dz \tag{B.10}$$

$$\left\{ \begin{array}{c} M_s \\ M_{s\theta} \end{array} \right\} = \int_{-\frac{h}{2}}^{\frac{h}{2}} \left\{ \begin{array}{c} \sigma_s \\ \tau_{s\theta} \end{array} \right\} \left(1 + \frac{z}{R}\right) z dz \tag{B.11}$$

$$\left\{ \begin{array}{c} M_\theta \\ M_{\theta s} \end{array} \right\} = \int_{-\frac{h}{2}}^{\frac{h}{2}} \left\{ \begin{array}{c} \sigma_\theta \\ \tau_{\theta s} \end{array} \right\} z dz \tag{B.12}$$

Substituting eq.B.7, B.8 into B.9~B.12, and expands the integrations, we can get the expressions of force and moment resultants in terms of strains. Utilizing the fact that $\frac{z}{R}$ is less than unity, one can expand the quotient $\frac{1}{1+z/R}$ into geometric series,

$$\frac{1}{1 + z/R} = \sum_{n=0}^{\infty} \left(-\frac{z}{R}\right)^n.$$

For sufficiently small $\frac{z}{R}$, 3rd and higher terms in the geometric series can be truncated. The final expressions are

$$\begin{aligned}
N_s &= \frac{Eh}{1-\nu^2} \left[\epsilon_s + \nu\epsilon_\theta + \frac{h^2}{12R}\kappa_s\right] \\
N_\theta &= \frac{Eh}{1-\nu^2} \left[\epsilon_\theta + \nu\epsilon_s - \frac{h^2}{12R}\left(\kappa_\theta - \frac{\epsilon_\theta}{R}\right)\right] \\
N_{s\theta} &= \frac{Eh}{2(1+\nu)} \left[\epsilon_{s\theta} + \frac{h^2}{24R}\zeta\right] \\
N_{\theta s} &= \frac{Eh}{2(1+\nu)} \left[\epsilon_{s\theta} - \frac{h^2}{12R}\left(\frac{\zeta}{2} - \frac{\epsilon_{s\theta}}{R}\right)\right] \\
M_s &= \frac{Eh^3}{12(1-\nu^2)} \left[\kappa_s + \nu\kappa_\theta + \frac{\epsilon_s}{R}\right] \\
M_\theta &= \frac{Eh^3}{12(1-\nu^2)} \left[\kappa_\theta + \nu\kappa_s - \frac{\epsilon_\theta}{R}\right] \\
M_{s\theta} &= \frac{Eh^3}{24(1+\nu)}\zeta \\
M_{\theta s} &= \frac{Eh^3}{24(1+\nu)} \left(\zeta - \frac{\epsilon_{s\theta}}{R}\right)
\end{aligned} \tag{B.13}$$

B.5   Equations of Motion

Equations of motion were derived by applying Newton's Law, summing forces and moments which act upon a shell element of thickness h, as shown in Figure B.3

$$
\begin{aligned}
\frac{1}{R}\frac{\partial N_s}{\partial s} + \frac{1}{R}\frac{\partial N_{\theta s}}{\partial \theta} &= \rho h \ddot{u} \\
\frac{1}{R}\frac{\partial N_{s\theta}}{\partial s} + \frac{1}{R}\frac{\partial N_{\theta}}{\partial \theta} + \frac{Q_\theta}{R} &= \rho h \ddot{v} \\
\frac{1}{R}\frac{\partial Q_s}{\partial s} + \frac{1}{R}\frac{\partial Q_\theta}{\partial \theta} - \frac{N_\theta}{R} &= \rho h \ddot{w} \\
\frac{1}{R}\frac{\partial M_s}{\partial s} + \frac{1}{R}\frac{\partial M_{\theta s}}{\partial \theta} - Q_s &= 0 \\
\frac{1}{R}\frac{\partial M_{s\theta}}{\partial s} + \frac{1}{R}\frac{\partial M_\theta}{\partial \theta} - Q_\theta &= 0 \\
N_{s\theta} - N_{\theta s} - \frac{M_{\theta s}}{R} &= 0
\end{aligned}
\tag{B.14}
$$

the last equation is not independent and so redundant.

B.6   Derivation of Flügge's Equation

The equations of motion for thin circular cylindrical shells by Flügge were derived combining eq.B.7, B.13 and B.14. The **Flügge's Equation** can be written in matrix form:

$$
\Im\{u_i\} = 0 \tag{B.15}
$$

where $\{u_i\}$ is the displacement vector and $\Im$ is a matrix differential operator,

$$
\Im = \Im_{D-M} + k\Im_{Flügge} \tag{B.16}
$$

and k is the thickness parameter $k = \frac{h^2}{12R^2}$. $\Im_{D-M}$ is derived as

$$
\begin{bmatrix}
\frac{\partial^2}{\partial s^2} + \left(\frac{1-\nu}{2}\right)\frac{\partial^2}{\partial \theta^2} - \Omega^2\frac{\partial^2}{\partial t^2} & \left(\frac{1+\nu}{2}\right)\frac{\partial^2}{\partial s\partial \theta} & \nu\frac{\partial}{\partial s} \\[2ex]
\left(\frac{1+\nu}{2}\right)\frac{\partial^2}{\partial s\partial \theta} & \left(\frac{1-\nu}{2}\right)\frac{\partial^2}{\partial s^2} + \frac{\partial^2}{\partial \theta^2} - \Omega^2\frac{\partial^2}{\partial t^2} & \frac{\partial}{\partial \theta} \\[2ex]
\nu\frac{\partial}{\partial s} & \frac{\partial}{\partial \theta} & 1 + k\nabla^2\nabla^2 + \Omega^2\frac{\partial^2}{\partial t^2}
\end{bmatrix}
\tag{B.17}
$$

and $\Im_{Fl\ddot{u}gge}$ is a modifier for Flügge's Theory,

$$\Im_{Fl\ddot{u}gge} = \begin{bmatrix} \left(\frac{1-\nu}{2}\right)\frac{\partial^2}{\partial\theta^2} & 0 & -\frac{\partial^3}{\partial s^3} + \left(\frac{1-\nu}{2}\right)\frac{\partial^3}{\partial s\partial\theta^2} \\ 0 & 3\left(\frac{1-\nu}{2}\right)\frac{\partial^2}{\partial s^2} & -\left(\frac{3-\nu}{2}\right)\frac{\partial^3}{\partial s^2\partial\theta} \\ -\frac{\partial^3}{\partial s^3} + \left(\frac{1-\nu}{2}\right)\frac{\partial^3}{\partial s\partial\theta^2} & -\left(\frac{3-\nu}{2}\right)\frac{\partial^3}{\partial s^2\partial\theta} & 1 + 2\frac{\partial^2}{\partial\theta^2} \end{bmatrix} \quad \text{(B.18)}$$

where $\Omega^2 = \frac{\rho(1-\nu^2)R^2}{E}$ and $\nabla^2 = \frac{\partial}{\partial s^2} + \frac{\partial}{\partial\theta^2}$.

B.7 Boundary Conditions

Assume the shell vibrates with both ends completely free, its boundary conditions are

$$
\begin{aligned}
N_s &= 0 \\
N_{s\theta} + \frac{M_{s\theta}}{R} &= 0 \\
Q_s + \frac{1}{R}\frac{\partial M_{s\theta}}{\partial\theta} &= 0 \\
M_s &= 0
\end{aligned}
\qquad \text{at} \qquad s = 0, Rl \qquad \text{(B.19)}
$$

At the boundaries, there are no reaction forces or moments. Summation of shear force and moment is zero.

B.8 Displacement Functions

The displacement functions exhibit periodic behavior with respect to time and the circumferential angle θ is preserved in the solution functions of u, v and w. Besides, the periodic variation with respect to s is also generalized to an exponential function $e^{\lambda s}$. Displacement functions at natural modes are in the form of

$$
\begin{aligned}
u &= Ae^{\lambda s}\cos n\theta \cos\omega t \\
v &= Be^{\lambda s}\sin n\theta \cos\omega t \\
w &= Ce^{\lambda s}\cos n\theta \cos\omega t
\end{aligned}
\qquad \text{(B.20)}
$$

where n is the number of circumferential waves, A, B, C and λ are undetermined constants and ω is the resonance frequency. Substituting equation B.20 into B.15, this leads to a set of homogeneous equations. For a non-trivial solution, the determinant of coefficient matrix is set equal to zero. An 8th order characteristic equation in terms of ω and λ is obtained that can be solved for resonance frequencies and mode shapes at different natural modes. The determinant can be written as

$$
\begin{vmatrix}
\lambda^2 - \frac{n^2(1+k)(1-\nu)}{2} + \Pi & \frac{1+\nu}{2}\lambda n & v\lambda - k\left(\lambda^3 + \frac{(1-\nu)\lambda n^2}{2}\right) \\
-\frac{(1+\nu)\lambda n}{2} & \frac{(1+3k)(1-\nu)\lambda^2}{2} - n^2 + \Pi & -n + k\lambda^2 n\frac{3-\nu}{2} \\
v\lambda - k\left(\lambda^3 + \frac{(1-\nu)\lambda n^2}{2}\right) & n - k\lambda^2 n\frac{3-\nu}{2} & 1 + k\left[1 - 2n^2 + \left(n^2 - \lambda^2\right)^2\right] - \Pi
\end{vmatrix}
$$

(B.21)

where $\Pi = \frac{\rho(1-\nu^2)R^2\omega^2}{E}$.

Appendix C

Design Specifications

C.1 Specifications of Humanoid Hand Design

All dimensions are in mm.
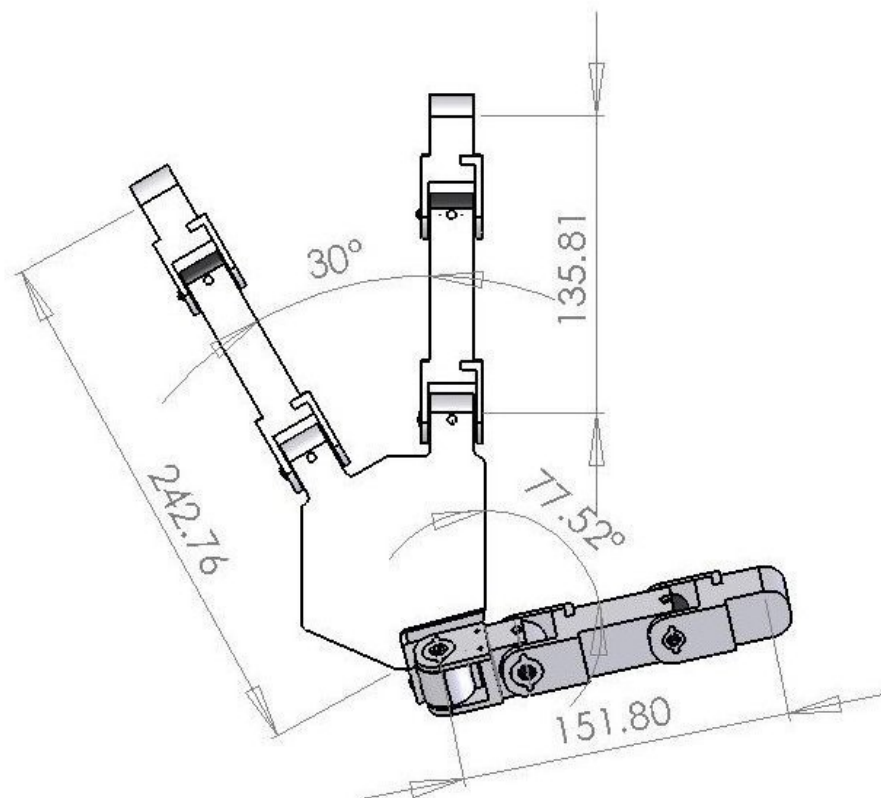
Figure C.1: Humanoid Hand Assembly
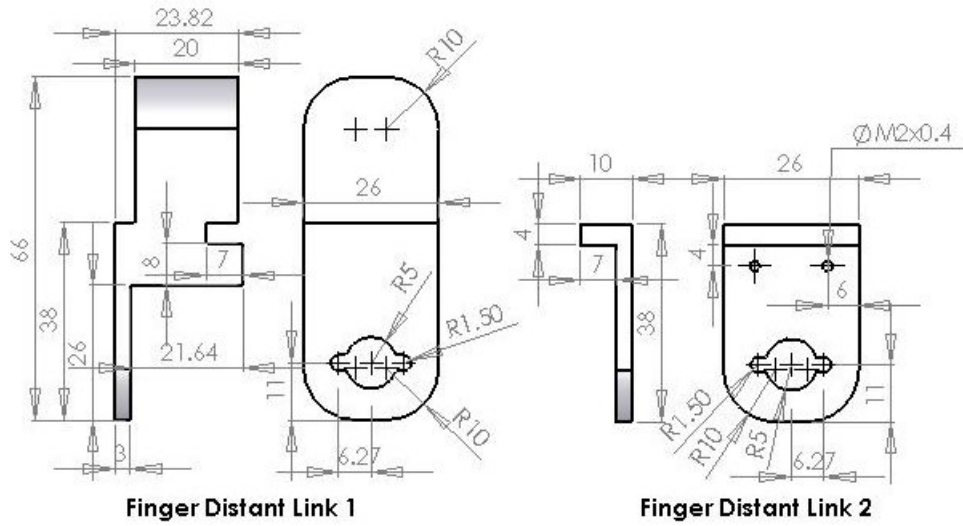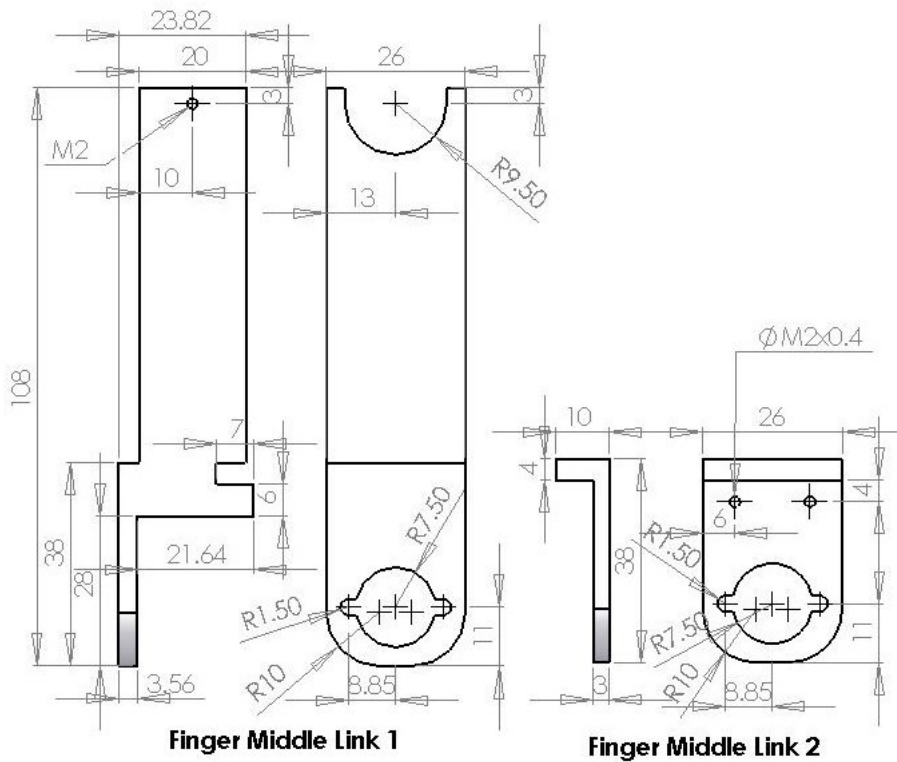
Figure C.2: Humanoid Hand Parts (1)
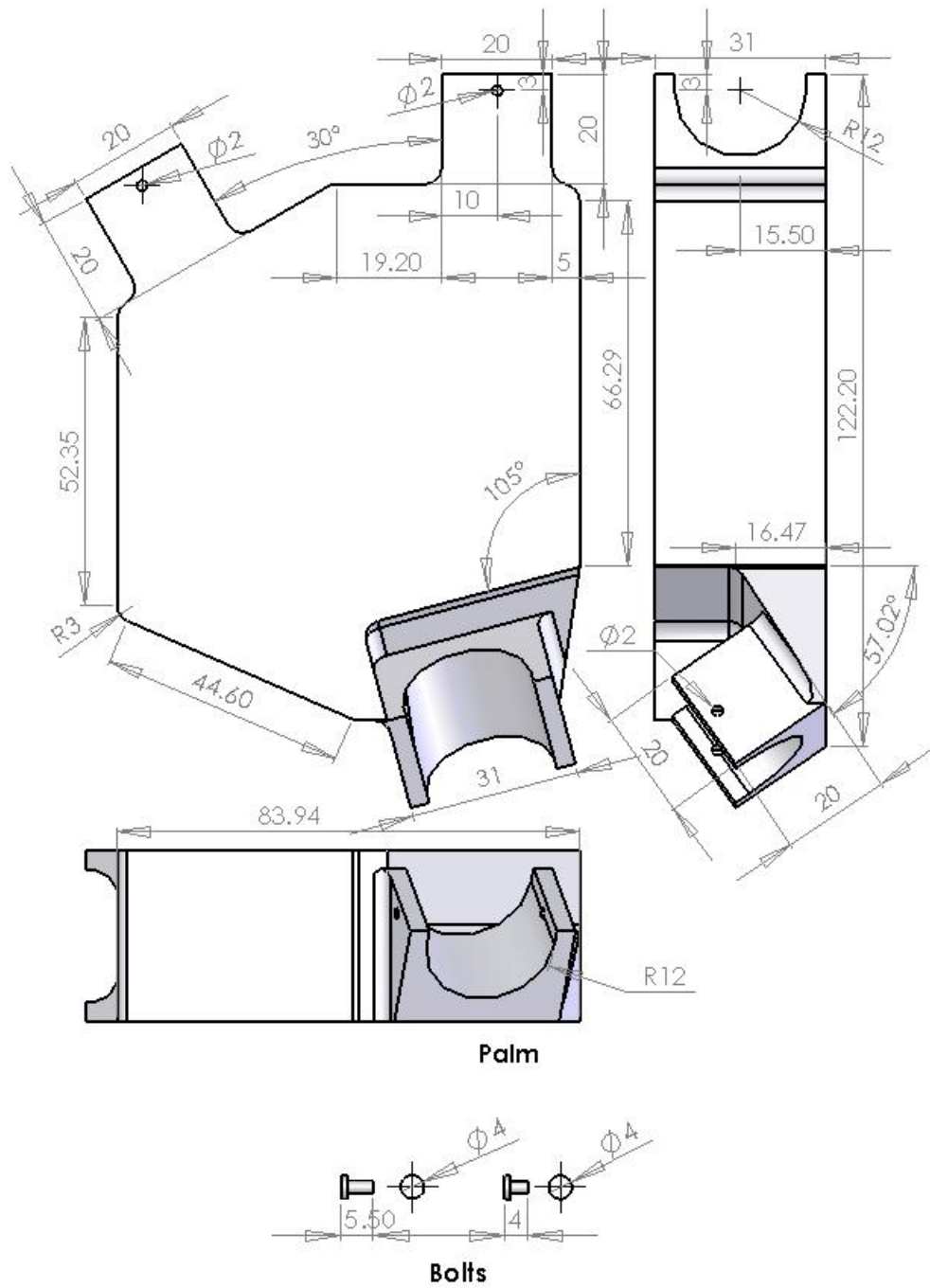

Figure C.3: Humanoid Hand Parts (2)

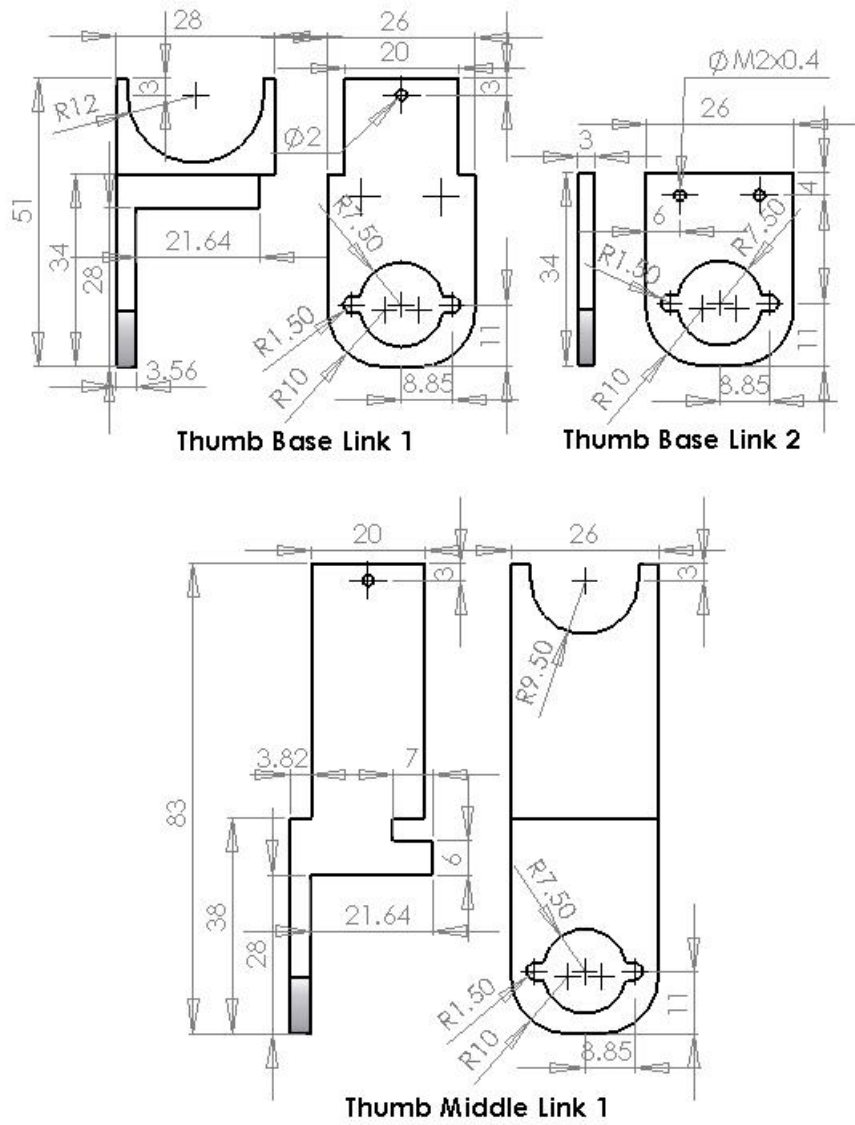Figure C.4: Humanoid Hand Parts (3)

Figure C.5: Humanoid Hand Parts (4)
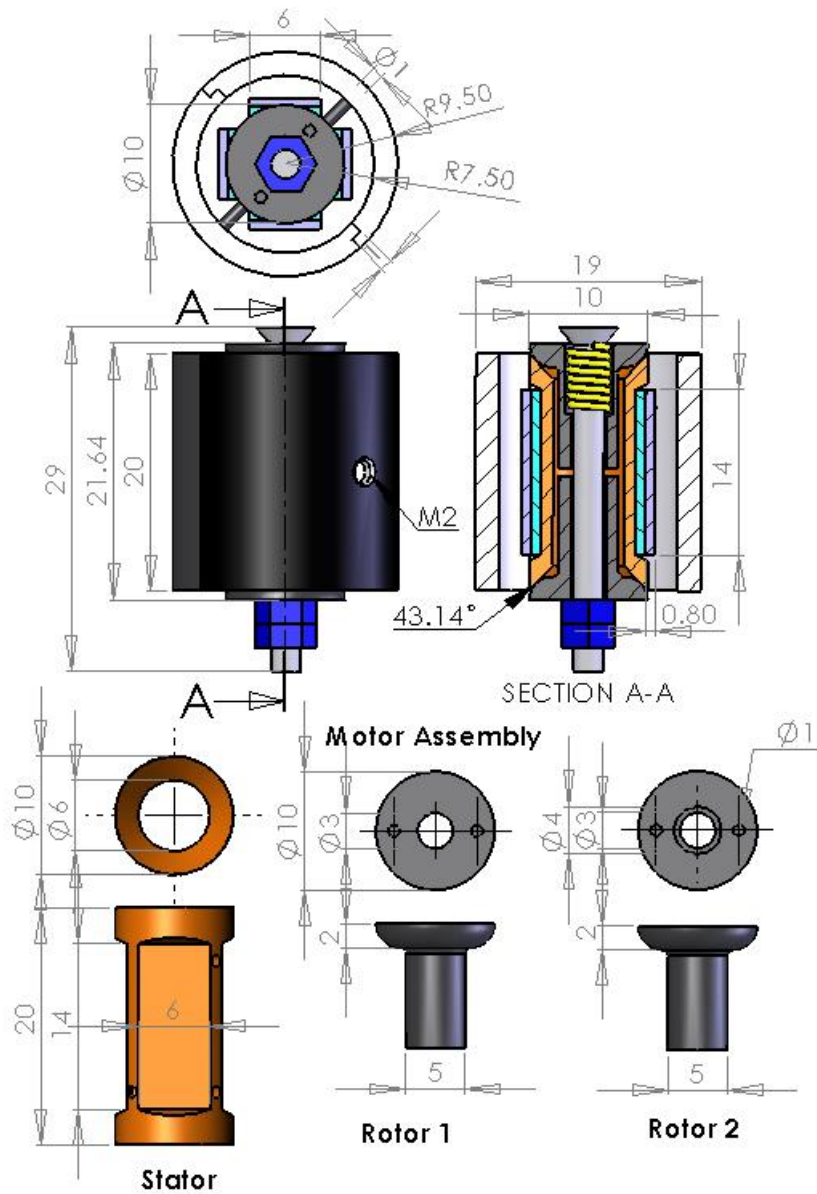
C.2 Specifications of Cylindrical USM Motors

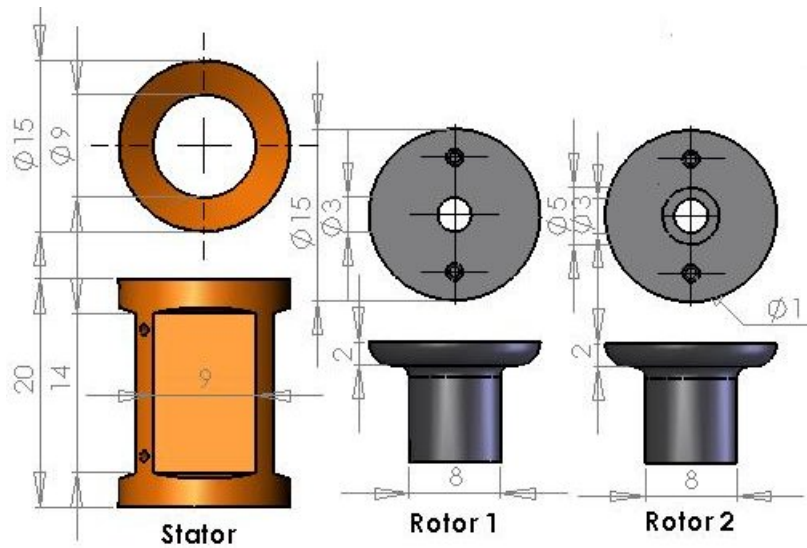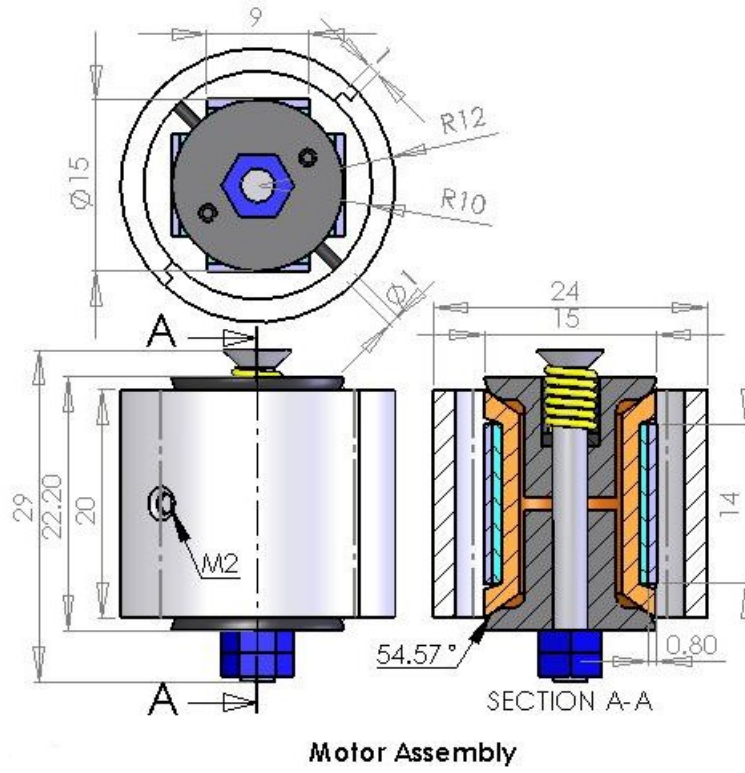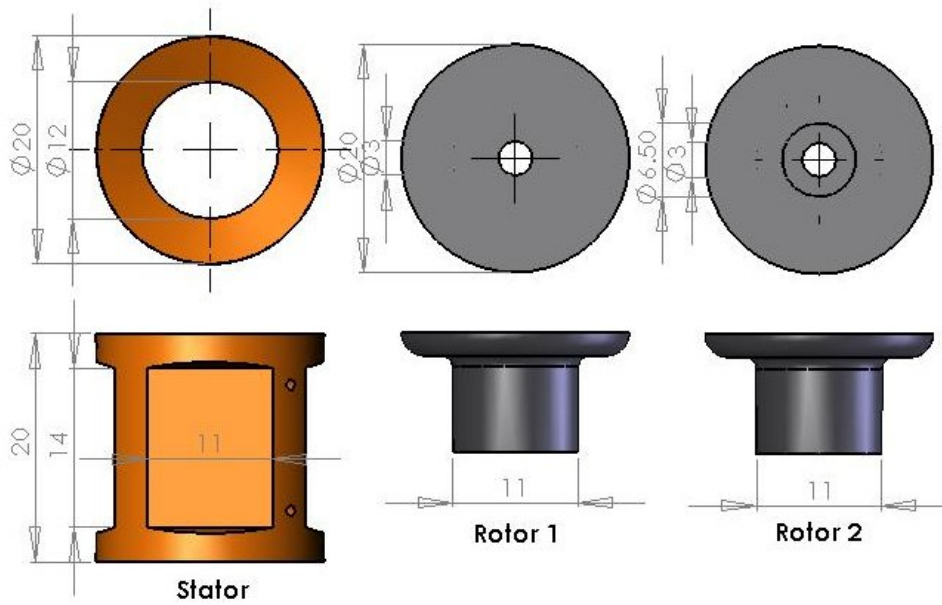Detail dimensions of the 3 motors.
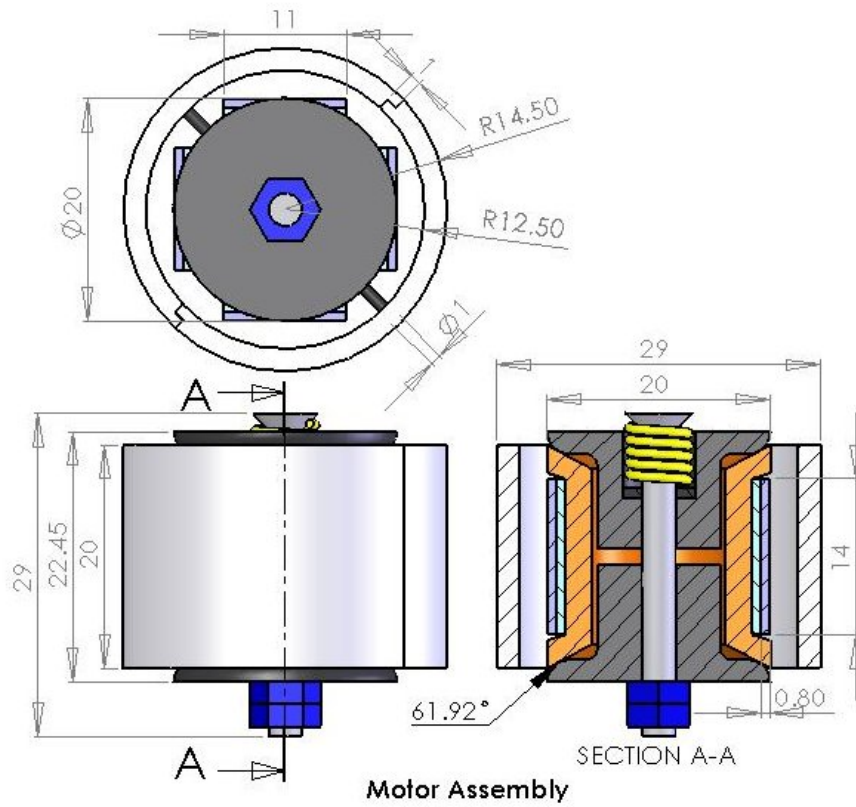

Figure C.6: Motor S

Figure C.7: Motor M

Figure C.8: Motor L
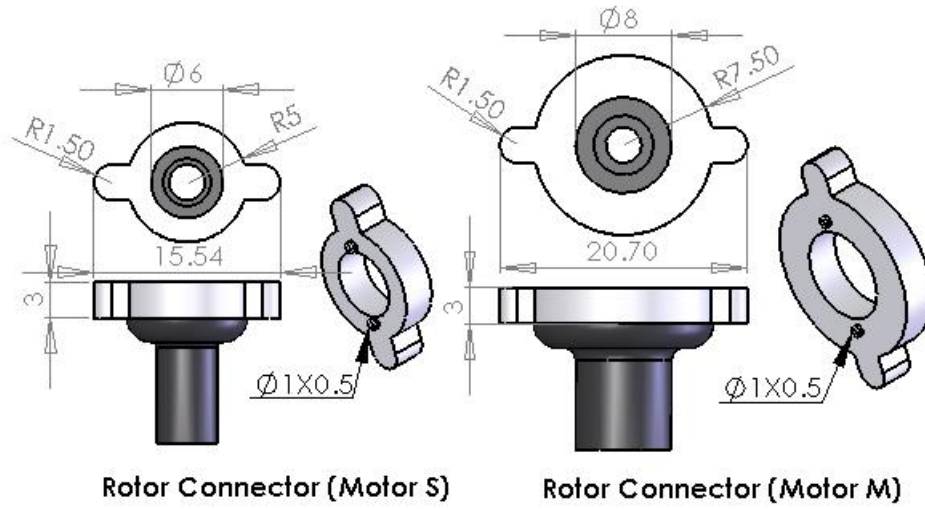
C.3   Miscellaneous Dimensions

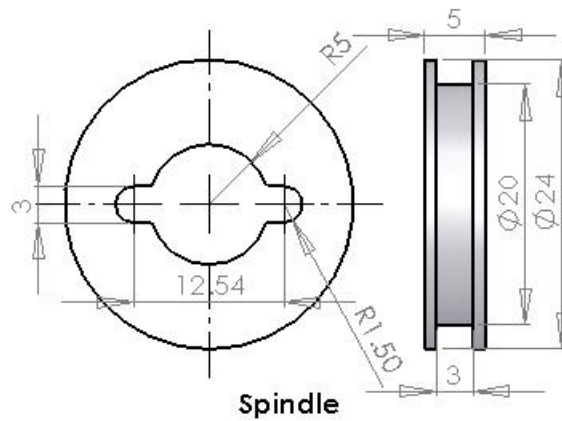Figure C.9: External Connectors for Force transmission

Figure C.10: Spindle for Torque-Speed Measurement (Motor S)

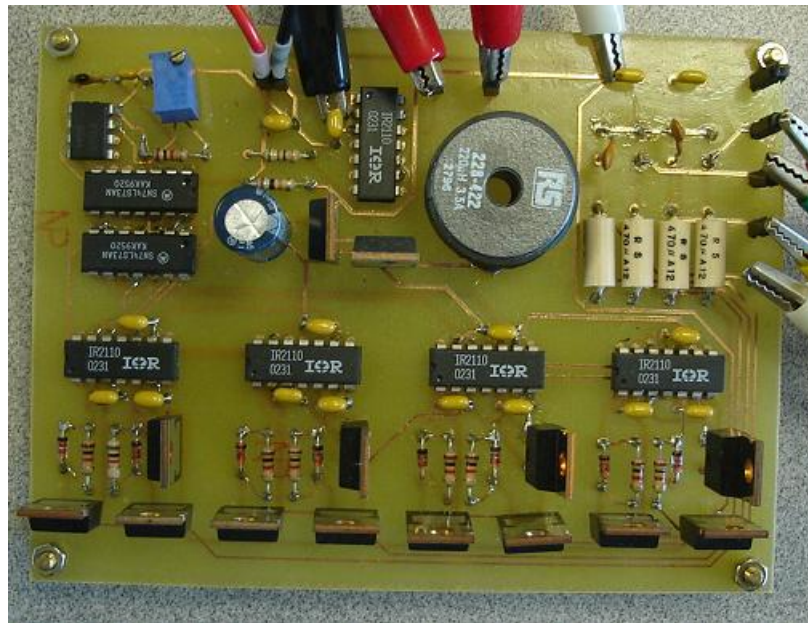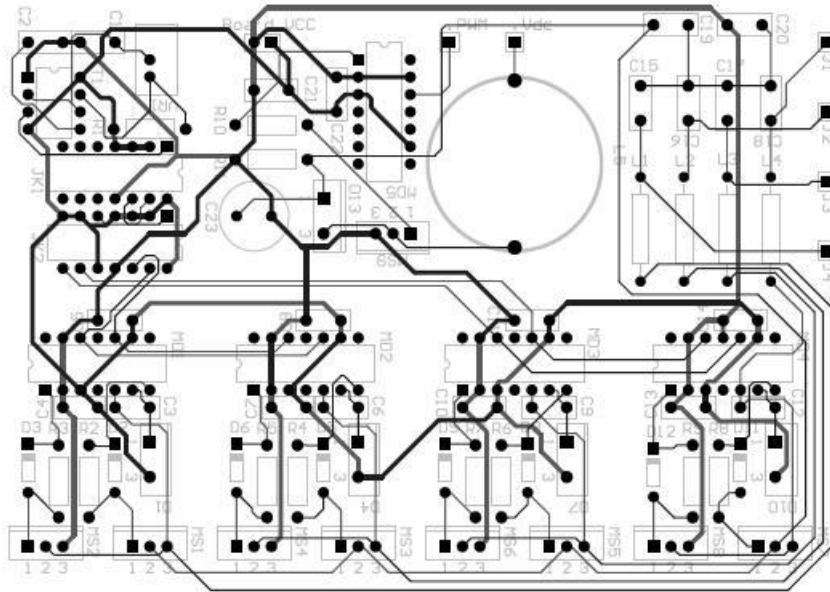## C.4 PCB Board Design and Implementation

Figure C.11: PCB Board Design and Actual Implementation

Bibliography

[1] S.Ueha, Y.Tomikawa, M.Kurosawa, N.Nakamura: *Ultrasonic Motors: Theory and Applications*, Oxford: Clarendon Press, (1993).

[2] J.K.Salisbury, J.J.Craig: *Articulated Hands: Force Control and Kinematics Issues*, International Journal of Robotics Research, **1**(1), (1982), 4-17.

[3] S.C.Jacobsen, J.E.Wood, D.F.Knutti, K.B.Biggers: *The UTAH/MIT Dextrous Hand: Work in Progress*, International Journal of Robotics Research, **3**(4), (1984), 21-50.

[4] J.Butterfass, M.Grebenstein, H.Lieu, G.Hirzinger: *DLR-Hand II: Next Generation of a Dextrous Robot Hand*, Proceedings of the 2001 IEEE International Conference on Robotics and Automation, (2001), 109-114.

[5] J.K.Salisbury, M.T.Mason: *Robot Hands and the Mechanics of Manipulation*, MIT Press, (1985).

[6] C.S.Lovchic, M.A.Diftler: *The Robonaut Hand: Dextrous Robot Hand for Space*, Proceedings of the 1999 IEEE International Conference on Robotics and Automation, (1999), 907-912.

[7] R.Tubiana: *Architecture and Functions of the Hand*, The Hand Vol. **1**, W.B.Saunders, Philadelphia, PA, (1981), 19-93.

[8] M.Dorey: *Advances in Actuators*, Institute of Physics Publishing, Bristol and Philadelphia, (1995).

[9] T.Sashida, T.Kenjo: *An Introduction to Ultrasonic Motors*, Oxford Science Publications, (1993).

[10] K.Nishibori, S.Okuma, H.Obata, S.Kondo: *Robot Hand with Fingers using Vibration-Type Ultrasonic Motors (Driving Characteristics)*, Proceedings of 4th IEEE International Workshop on Advanced Motion Control, Tsu, Mie, Japan, (1996), 97-102.

[11] B.H.Choi, H.R.Choi: *SKK Hand Master-Hand Exoskeleton Driven by Ultrasonic Motors*, Proceedings of the 2000 IEEE/RSJ International Conference on Intelligent Robots and Systems, (2000), 1131-1136.

[12] I.Yamano, T.Maeno: *Five-fingered Robot Hand using Ultrasonic Motors and Elastic Elements*, Proceedings of the 2005 IEEE International Conference on Robotics and Automation, (2005), 2684-2689.

[13] S.Dilibal, R.M.Tabanli, A.Dikicioglu: *Development of Shape Memory Actuated ITU Robot Hand and Its Mine Clearance Compatibility*, Journal of Materials Processing Technology, (2004).

[14] Y.Bar-Cohen: *Biologically Inspired Intelligent Robotics Using Artificial Muscles*, 2003 International Conference on MEMS, NANO, and Smart Systems, (2003).

[15] G.A.Bekey, R.Tomovic, I.Zeljkovic: *Control Architecture for the Belgrade/USC Hand*, S.T.Venkataraman and T.Iberall (eds.) Dextrous Robot Hands, NY: Springer-Verlag, (1990), 136-149.

[16] J.Vanriper, M.S.Ali, K.J.Kyriakopoulos, H.E.Stephanou: *Description and Kinematic Analysis of the Anthrobot-2 Dextrous Hand*, Proceedings of the 1992 IEEE International Symposium on Intelligent Control, (1992), 299-305.

[17] L.R.Lin, H.P.Huang: *Mechanism Design of A New Multifingered Robot Hand*, Proceedings of the 1996 IEEE International Conference on Robotics and Automation, (1996).

[18] T.Morita, H.Iwata, S.Sugano: *Development of Human Symbiotic Robot: WENDY*, Proceedings of the 1999 IEEE International Conference on Robotics and Automation, (1999).

[19] T.Raparelli, G.Mattiazzo, S.Mauro, M.Velardocchia: *Design and Development of a Pneumatic Anthropomorphic Hand*, Journal of Robotic Systems **17**(1), (2000), 1-15.

[20] S.Schulz, C.Pylatiuk, G.Bretthauer: *A New Ultralight Anthropomorphic Hand*, Proceedings of the 2001 IEEE International Conference on Robotics and Automation, (2001).

[21] H.Kawasaki, T.Komatsu, K.Uchiyama: *Anthropomorphic Robot Hand: Gifu Hand III*, International Conference on Control, Automation, and Systems, (2002), 1288-1293.

[22] *http://www.shadowrobot.com/hand/*, (2004).

[23] F.Lotti, P.Tiezzi, G.Vassura, L.Biagiotti, G.Palli, C.Melchiorri: *Development of UB Hand 3: Early Results*, Proceedings of the 2005 IEEE International Conference on Robotics and Automation, (2005), 4488-4493.

[24] T.Mouri, H.Kawasaki, K.Umebayashi: *Developments of New Anthropomorphic Robot Hand and its Master Slave System*, 2005 IEEE/RSJ International Conference on Intelligent Robots and Systems, (2005).

[25] B.J.Choi, S.H.Lee, H.R.Choi, S.C.Kang: *Development of Anthropomorphic Robot Hand with Tactile Sensor : SKKU Hand II*, Proceedings of the 2006 IEEE/RSJ International Conference on Intelligent Robots and Systems, (2006).

[26] M.R.Cutkosky: *On Grasp Choice, Grasp Model, and the Design of Hands for Manufacturing Task*, IEEE Transactions on Robotics and Automation **5**, (1989), 269-279.

[27] A.Bicchi: *On the Closure Properties of Robotic Grasping*, International Journal of Robotics Research **14**(4), (1995), 319-334.

[28] E.Rimon, J.Burdick: *On Force and Form Closure For Multiple Finger Grasps*, Proceedings of the 1996 IEEE International Conference on Robotics and Automation, (1996), 1795-1800.

[29] Z.Li, P.Hsu, S.Sastry: *Grasping and Coordinated Manipulation by a Multifingered Robot Hand*, International Journal of Robotics Research **8**(4), (1989), 33-50.

[30] H.Zhang, K.Tanie, H.Maekawa: *Dextrous Manipulation Planning by Graph Transformation*, Proceedings of the 1996 IEEE International Conference on Robotics and Automation, (1996), 3055-3060.

[31] M.R.Cutkosky, P.K.Wright: *Modeling Manufacturing Grips and Correlations with the Design of Robotic Hands*, Proceedings of the 1986 IEEE International Conference on Robotics and Automation, (1986).

[32] V.D.Nguyen: *Constructing Force-Closure Grasp*, International Journal of Robotics Research **7**(3), (1988), 3-16.

[33] C.P.Tung, A.C.Kak: *Fast Construction of Force-Closure Grasps*, IEEE Transactions on Robotics and Automation **12**(4), (1996), 615-626.

[34] D.Ding, Y.H.Liu, S.G.Wang: *Computation of 3-D Form-Closure Grasps*, IEEE Transactions on Robotics and Automation **17**(4), (2001), 515-522.

[35] C.Ferrari, J.Canny: *Planning Optimal Grasps*, Proceedings of the 1992 IEEE International Conference on Robotics and Automation, (1992), 2290-2295.

[36] P.Hagedorn, J.Wallaschek: *Travelling Wave Ultrasonic Motors, Part 1: Working Principle and Mathematical Modeling of the Stator*, Journal of Sound and Vibration, (1992) **155**(1), 31-46.

[37] N.W.Hagood IV, A.J.McFarland: *Modeling of a Piezoelectric Rotary Ultrasonic Motor*, IEEE Transactions on Ultrasonics, Ferroelectrics and Frequency Control **42**(2), (1995), 210-224.

[38] D.Sun, J.B.Liu, X.Ai: *Modeling and Performance Evaluation of Traveling-Wave Piezoelectric Ultrasonic Motors with Analytical Method*, Sensors and Actuators, A 100, (2002), 84-93.

[39] J.L.Pons, H.Rodríguez, F.Seco, R.Ceres, L.Calderón: *Modeling of Piezoelectric Transducers Applied to Piezoelectric Motors: A Comparative Study and New Perspective*, Sensors and Actuators A 110, (2004), 336-343.

[40] A.Frangi, A.Corigliano, M.Binci, P.Faure: *Finite Element Modeling of a Rotating Piezoelectric Ultrasonic Motor*, Ultrasonics 43, (2005), 747-755.

[41] G.Bal, E.Bekiroğlu: *Characteristics Estimation of Travelling-Wave Ultrasonic Motor Using Equivalent Circuit Model*, Eleco'2001 International Conference on Electrical and Electronics Engineering, (2001).

[42] T.Senjyu, T.Kashiwagi, K.Uezato: *Position Control of Ultrasonic Motors Using MRAC and Dead-Zone Compensation With Fuzzy Inference*, IEEE Transactions on Power Electronics **17**(2), (2002), 265-272.

[43] K.T.Chau, S.W.Chung, C.C.Chan: *Neuro-Fuzzy Speed Tracking Control of Travelling-Wave Ultrasonic Motor Drives Using Direct Pulsewidth Modulation*, IEEE Transactions on Industry Applications **39**(4), (2003), 1061-1069.

[44] T.Senjyu, K.Uezato, H.Miyazato: *Adjustable Speed Control of Ultrasonic Motors by Adaptive Control*, IEEE Transactions on Power Electronics **10**(5), (1995), 532-538.

[45] V.I.Utkin: *Sliding Mode Control Design Principles and Applications to Electric Drives*, IEEE Transactions on Industrial Electronics **40**(1), (1993), 23-36.

[46] C.Y.Yen, F.L.Wen, M.S.Ouyang: *Thin-disc Piezoelectric Ultrasonic Motor. Part II: System Construction and Control*, Ultrasonics 41, (2003), 451-463.

[47] M.Berg, P.Hagedorn, S.Gutschmidt: *On the Dynamics of Piezoelectric Cylindrical Shells*, Journal of Sound and Vibration 274, (2004), 91-109.

[48] T.Morita, M.Kurosawa, T.Higuchi: *An Ultrasonic Micromotor Using A Bending Cylindrical Transducer Based on PZT Thin Film*, Sensors and Actuators A 50, (1995), 75-80.

[49] P.Lu, K.H.Lee, S.P.Lim, W.Z.Lim: *A Kinematic Analysis of Cylindrical Ultrasonic Micromotors*, Sensors and Actuators, A 87, (2001), 194-197.

[50] G.Schlesinger: *Der Mechanische Aufbau der kunstlischen Glieder [The Mechanical Structure of Artificial Limbs]*, In M.Borchardt *et al.* (Eds.), Ersatzklieder und Arbeitshilfen fur Kriegsbeschadigte und Unfallverletzte, Berlin: Springer, (1919), 21-600.

[51] J.R.Napier: *The Prehensile Movements of the Human Hand*, The Journal of Bone & Joint Surgery **38**B(4), (1956), 902-913.

[52] P.Somov: *Uber Gebiete von Schraubengeschwindigkeiten eines starren K orpers bei verschiedener Zahl von St utz achen*, Zeitschrift f ur Mathematik und Physik, vol.45, (1900).

[53] K.Lakshminarayana: *Mechanics of Form Closure*, ASME paper 78-DET-32, (1978),2-8.

[54] M.E.Johanson, W.M.Murray, N.Smaby, G.J van de Pol, J.D.Towles, F.E.Zajac, V.R.Hentz: *Key Pinch Force is More Misdirected in Individuals with Tetraplegia Compared to Non-impaired Subjects*, Proceedings of the Third National Meeting Rehabilitation Research and Development Conference, Arlington, VA, (2002), 115.

[55] G.Burdea: *Force and Touch Feedback for Virtual Reality*, New York: John Wiley and Sons, (1996).

[56] L.D.KETCHUM, D.E.THOMPSON: *An Experimental Investigation Into the Forces Internal to the Human Hand*, Paul W.Brand & Hollister, Clinical Mechanics of the Hand, St.Louis: Mosby, (1985).

[57] T.J.HO: *Humanoid Hand Design*, FYP Report, Department of Mechanical Engineering, NUS, (2005).

[58] L.C.LIM, J.JIN, K.K.RAJAN, S.P.LIM, P.LU, K.H.LEE: *New-generation High-performance Piezo Single Crystal Driven Micro-actuators/motors*, Internal Research Report, NUS, (2005).

[59] N.MOHAN, T.M.UNDELAND, W.P.ROBBINS: *Power Electronics: Converters, Applications and Design*, 2nd Edition, John Wiley & Sons Inc., (1995).

[60] X.P.WANG: *Modelling And Control Of Cylindrical Ultrasonic Motor*, Master Thesis, Department of Mechanical Engineering, NUS, (2002).